UNIVERSITÀ
POLITECNICA
DELLE MARCHE

Scuola di Dottorato di Ricerca in Scienze dell'Ingegneria
Corso di Dottorato in Ingegneria Meccanica

Mechanical characterization of shape memory thermoplastic polyurethane

Ph.D. Dissertation of:
Mattia Coccia

Advisor:
Prof. Marco Sasso

Coadvisor:
Prof. Gianluca Chiappini

Curriculum Supervisor:
Prof. Giovanni Di Nicola

XX edition - new series

UNIVERSITÀ
POLITECNICA
DELLE MARCHE

Scuola di Dottorato di Ricerca in Scienze dell'Ingegneria
Corso di Dottorato in Ingegneria Meccanica

Mechanical characterization of shape memory thermoplastic polyurethane

Ph.D. Dissertation of:
Mattia Coccia

Advisor:
Prof. Marco Sasso

Coadvisor:
Prof. Gianluca Chiappini

Curriculum Supervisor:
Prof. Giovanni Di Nicola

XX edition - new series

UNIVERSITÀ POLITECNICA DELLE MARCHE
SCUOLA DI DOTTORATO DI RICERCA IN SCIENZE DELL'INGEGNERIA
CORSO DI DOTTORATO IN INGEGNERIA MECCANICA
Via Brecce Bianche – 60131 Ancona (AN), Italy

Dedicato alla mia famiglia

Abstract

In recent years, Shape Memory Polymers (SMPs) received considerable attention in the research community, due to the possibility of controlling one or more of their mechanical properties through the application of different external stimuli. The shape memory effect (SME) is the peculiarity of this family of polymers as it allows the transition from a permanent to a temporary shape and vice versa. Compared to other shape memory materials, polymers can be processed by injection molding (as can all plastics). This feature facilitates their production, allowing the molding of a large number of shape memory plastic parts in a very short time and with reduced cost. However, the complexity of the transformation process, from the raw material to the finished product, can lead to failure to achieve the required production volumes and quality standards. For this reason, in order to ensure an optimized and repeatable production process, it is necessary to monitor the condition of the material during the transformation process using sensors.

Within this context, the aim of this thesis is to identify the best way of processing a shape memory polymer by injection molding. The research aim was determine which parameters have the greatest influence on the quality of a product (particularly with regard to aesthetics), dimensional quality and mechanical properties. For this purpose, a mold was designed for the production of tensile test specimens. The mold was also equipped with pressure and temperature sensors in the cavity, which allowed direct monitoring during all phases of the process. Thanks to the use of numerical process simulations using the Moldex3D software, the design of the mold was evaluated, and the process was analyzed for each stage.

The research activity focuses on the study of mechanical and shape memory properties, which are determined by performing a well-defined thermomechanical cycle. For this reason, an experimental campaign was carried out in order to understand the effect of different parameters, to which the material may be subjected (i.e. temperature, deformation and deformation speed), on the shape memory effect. In particular, the influence of the mentioned parameters on the capability of the material to maintain and recover a temporary shape was evaluated on a polyurethane-based shape memory polymer (SMPU).

Subsequently, a constitutive model present in the literature was implemented with a commercial FEM code in order to simulate the shape memory effect of the material; the coefficients required by the model were calibrated by means of a series of experimental tests. Finally, the validation of the model was carried out by comparing a number of experimental tests with those reproduced numerically.

Sommario

Negli ultimi anni, i polimeri a memoria di forma (SMPs) sono oggetto di numerose ricerche, grazie alla possibilità di controllare una o più delle loro proprietà meccaniche, tramite l'applicazione di svariati stimoli esterni. L'effetto a memoria di forma (SME) rappresenta la peculiarità di questa famiglia di polimeri in quanto consente il passaggio da una forma permanente ad una temporanea, e viceversa. Rispetto agli altri materiali a memoria di forma, i polimeri possono essere processati tramite stampaggio ad iniezione. Questa caratteristica facilita la loro produzione, permettendo lo stampaggio di un elevato numero di pezzi plastici a memoria di forma, in tempi e costi molto ridotti. Tuttavia, la complessità del processo di trasformazione, dalla materia prima fino alla realizzazione del prodotto finito, può portare al mancato raggiungimento dei volumi di produzione e degli standard di qualità richiesti. Per questo motivo, al fine di ottenere un processo produttivo ottimizzato e ripetibile, risulta necessario controllare le condizioni del materiale durante il processo di trasformazione con l'utilizzo di sensori.

All'interno di questo contesto, lo scopo della tesi è individuare il miglior modo di processare un polimero a memoria di forma, tramite stampaggio a iniezione. La domanda di ricerca vuole determinare quali parametri influiscono maggiormente sulla qualità di un prodotto (in particolare riguardo l'estetica), sulla qualità dimensionale e sulle proprietà meccaniche. A tal fine, è stato progettato uno stampo per la realizzazione di provini per test di trazione. Lo stampo è stato, inoltre, attrezzato con sensori di pressione e di temperatura in cavità, i quali hanno permesso un monitoraggio diretto durante tutte le fasi del processo. Grazie all'utilizzo di simulazioni numeriche di processo tramite il software Moldex3D, la progettazione dello stampo è stata valutata, e il processo è stato analizzato in ogni singola fase.

L'attività di ricerca si focalizza sullo studio delle proprietà meccanica e quelle a memoria di forma, le quali vengono determinate effettuando un ciclo termomeccanico ben definito. Per questo motivo è stata effettuata una campagna sperimentale finalizzata a comprendere meglio l'effetto di differenti parametri a cui può essere soggetto il materiale (cioè temperatura, deformazione e velocità di deformazione), sull'effetto a memoria di forma. In particolare, l'influenza dei parametri citati sulla capacità del materiale di mantenere e recuperare una forma temporanea è stata valutata su un polimero a memoria di forma a base poliuretanica (SMPU).

Successivamente, un modello costitutivo, presente in letteratura, è stato implementato con un codice FEM commerciale per riuscire a simulare l'effetto a memoria di forma del materiale; i coefficiente richiesti dal modello sono stati calibrati mediante una serie di prove sperimentali. Infine, la convalida del modello è stata effettuata tramite il confronto di alcune prove sperimentali e quelli riprodotti numericamente.

Contents

List of Figures

List of Tables

Chapter 1

Introduction

1.1 Motivation of the research

In recent years, the progression of a wide range of smart materials has enabled the development of numerous applications in medicine, mechanics, robotics, aerospace technologies and so on. In particular, the use of SMPs has not yet reached its full potential in engineering applications, but they are used for the property of free recovery capability or in applications where a low recovery force is required. The failure to achieve the use of this family of materials is mainly due to two reasons.

The first reason is related to the absence of studies on the processing of shape memory polymers. Thermoplastic shape memory polymers, differently from the other shape memory materials, have the advantage that they can be obtained with traditional processing techniques. This is due to the presence of weak bonds and the ability to easily reach melting temperature, which means that the class of thermoplastic polymers is suitable for various processes, e.g., extrusion and injection molding. The success of a product manufactured using injection molding technology, in terms of dimensional, aesthetic and structural quality, depends on many factors. The design of the mold is certainly very important, as it must be properly optimized for the manufacture of a product with a specific polymer. Another considerable factor is the control and optimization of the molding process parameters.

Otherwise, the second reason is due to the lack of available data on the exact behaviour of the shape memory effect. For the purpose of quantitatively assess the capability of SMPs to change and recovery the original shape from the temporary one, specific thermomechanical cyclic tests are required. This kind of test provides two significant parameters that characterize the SME strictly related to the deformation applied in the programming sequence: the shape Fixity ratio and the Recovery ratio; the former estimates the ability to maintain a temporary shape, the latter evaluates the capability to restore the original shape [14] [15]. Together, Fixity ratio and Recovery ratio characterize the SME of the examined polymer. For different SMPs, it was found that the Recovery and Fixity ratios are strongly influenced by several factors; among them, humidity, prescribed deformation, and temperature effects were extensively studied.

For these reasons, in this thesis work, a mold was developed to provide dog-bone standard specimens for mechanical tests have been manufactured by injection molding.

The mold used is equipped with cavity pressure and temperature sensors for process monitoring, with a view to ensure repeatability of the molding parameters within the cavity to obtain identical test specimens and compare simultaneously the properties of the materials obtained with simulation of the process. The use of sensors has also made it possible to better evaluate the molding cycle to understand which parameters most influence the process to ensure the correct process of the material. The reference polymer used is a shape memory polymer polyurethane-based and the mechanical characterization, necessary to investigate the SME, was performed by means of a campaign of thermomechanical tests. Specifically, in order to better understand how environmental conditions affect shape memory behaviour in terms of Fixity and Recovery ratio, a systematic study of the combined effect of strain, temperature and strain rate has been conducted.

1.2 Polymer materials

1.2.1 Brief history of plastics

The history of plastics is quite recent compared to other traditional materials such as metals, wood, glass etc. Indeed, the history of this material has been significantly investigated just over the last 100 years. In 1900, it was necessary to find a material to replace the ivory. Such material should be rigid, opaque, water-resistant, colourable, usable in a solid state and workable with a tool like metals. These requirements led to the discovery of a new material: the Bakelite, that is a thermosetting resin obtained by reacting phenol and formaldehyde. The Bakelite was defined “the first plastic material”. In the 1930s, the production of plastics from petroleum (such as Polyethylene and Polystyrene), along with the improvement of injection molding techniques (fully automated in 1937) brought the plastics to mass production. In the 1960s, a better understanding of polymerization mechanisms contributed to the emergence of plastics with high mechanical properties and heat resistance, also allowing the replacement of metals in many applications.

1.2.2 Structure of plastics

Polymers are substances consisting of large molecules. The polymers structure derives from the union of a large number of small units, generally called repetitive units. The basic units are single molecules, called monomers, and their union is possible thanks to the chemical bonds, of the same type along the same molecular chain, that are not easily dissociable. As shown in Figure 1.1, the monomers are the reactants from which the polymer is formed through the polymerization reaction; instead, the repetitive units are the repeating molecular groups, composing the polymer. There are two different polymerization processes:

$$\underset{\text{Monomers}}{A} \quad \overset{\textbf{Polimerization}}{\overline{\hspace{5cm}}} \quad \underset{\text{Repetitive Units}}{-(A)_n-}$$

Figure 1.1: Monomer and Repetitive Units.

- Poly-condensation, in which the union between the monomer molecules, as well as the polymer, the reaction is accompanied by the elimination of small molecules (water, ammonia, alcohol, etc.);

- Polyaddition, in which the macromolecule is formed without the elimination of other substances.

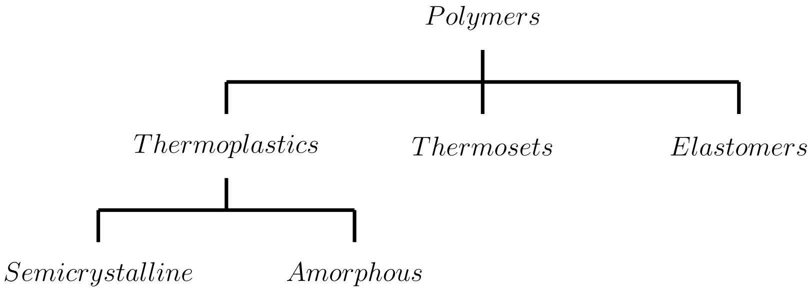

Figure 1.2: Classification of polymers.

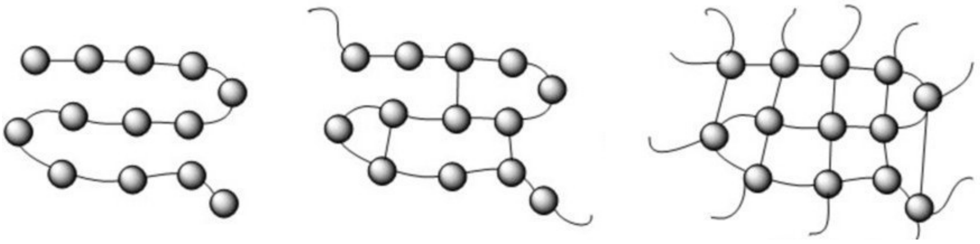

(a) (b) (c)

Figure 1.3: Structure for a thermoplastic (a), elastomer (b) and thermoset (c) polymers.

1.2.3 Classification of polymers

The best way to classify polymers, is dividing them in three groups based on molecular structure (as shown in Figure 1.2): thermoplastics [16], thermosetting [17], and elastomer [18] polymers. The structure of the different kind of polymers are depicted in Figure 1.3. Elastomers are, basically, rubbery polymers that can be stretched easily for several times from their unstretched length and which rapidly return to their original dimensions when the applied stress is released. Elastomers can be both thermoplastic and thermoset, they are cross-linked, but have a low cross-link density. The polymer chains still have some freedom to move, but are prevented from permanently moving relative to each other by the cross-links.

The thermoset class consists of irreversible polymers, which are able to create the chemical networks in three-dimensional directions through the polymerization (named also cross-linking or curing process) [19]. The curing process can be accomplished by specific radiations (e.g., heating [20], ultraviolet [21]) and catalysts or curing agents [22]. Generally, the development of such a process leads from the viscous liquid state to the solid one. As detailed in literature, in the curing process, the covalent bonds allow the individual chains of the polymers to link together for creating crosslinks. Crosslinked polymer network, defining the molecular architecture, gives a strong and rigid structure to the material, thus increasing the strength and providing high mechanical performances [23]. The nature of the thermosetting polymers enables several applications, such as the coating, adhesives and electrical equipment. However, most of the applications are in composite materials, reinforced with both carbon and glass fibers (used as matrix); for instance in sport equipment [24], automotive [25] and aerospace industries [26].

On the other hand, the thermoplastic class includes the reversible polymers, defined as materials that can be melted by heating and then back to the solid state after cooling. The reversible physical changes occur, because, in terms of molecular architecture, the thermoplastic is not cross-linked. Consequently, it is possible to identify and separate each single chain from the others. Thermoplastic polymers, depending on the arrangement of the molecular chain, can be further divided into two subclasses, namely amorphous or semi-crystalline polymers as depicted in Figure 1.4. In particular, a thermoplastic polymer is defined semi-crystalline (Figure 1.4(b)), when the molecular chains exhibit an organized and tightly packed structure, that ensure both elevated strength and chemical resistance as properties. Instead, an amorphous thermoplastic polymer (Figure 1.4(a)) presents more complex molecular chains, which are intertwined and randomly oriented. This specific structure influences the mechanical properties, resulting in a high impact resistance, a brittle behaviour and poor fatigue durability. Both aforementioned subclasses are representative of reusable and recyclable polymeric materials. Together with the presence of weak bonds and the capability to easily achieve the melting temperature, these properties make the class of thermoplastic polymers suitable for several processes either in the heat-softened state (e.g., by thermoforming [27]) or in the liquid state allowing to mold into a wide range of shapes (e.g., by extrusion and injection molding [28]).

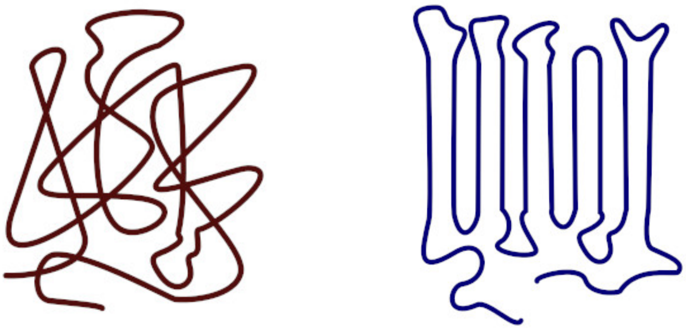

(a) (b)

Figure 1.4: Molecular chain organization for an amorphous (a) and semi-crystalline (b) thermoplastic polymer.

1.2.4 Temperature effect on specific volume and mechanical properties

In order to better understand the injection molding process, one of the most important characteristics of polymeric materials are the curves that connect Pressure, Temperature and Specific Volume or also named PVT curves. There are different behaviour of the PVT curves between amorphous and semi-crystalline polymers. For both of them, the main effect of increasing temperature is the material expands, with a consequent rise of the specific volume, contrarily an increment of the pressure decreases the specific volume.

Figure 1.5(a) shown the typical trend of PVT curves for an amorphous polymer. Focusing on the three curves it is possible to notice, for each of them, a point of change of slope, that identify the transition from fluid to solid state. Respect to the crystalline polymers, reported in Figure 1.5(b), the material behaviour is completely different. For this reason, the state change is not a true and proper solidification, but is called glass transition. This transition, consists of a disordered arrangement of macromolecules, that does not allow the molecular chain movement.

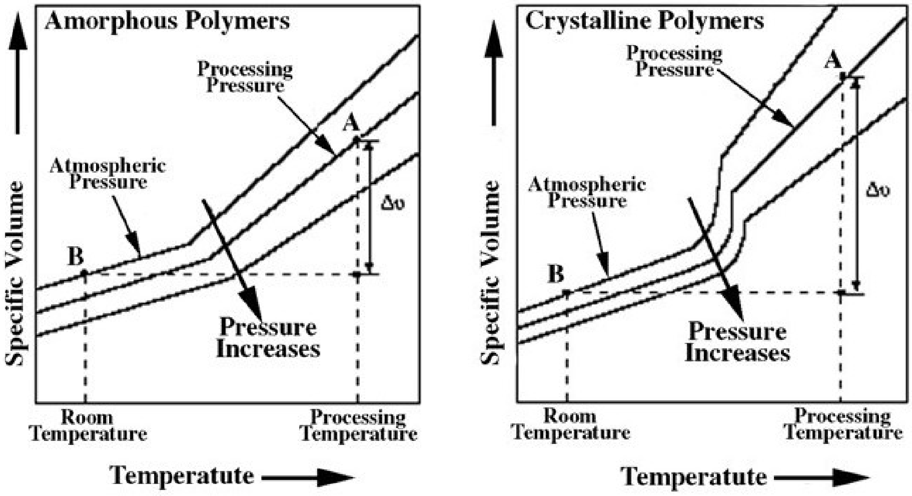

(a) (b)

Figure 1.5: Specific volume vs. Temperature for an amorphous (a) polymer and semi-crystalline (b) polymer. Reproduced from [1].

On the other hand, in crystalline polymers (Figure 1.5(b)) the transition from the fluid to the solid state, is characterized by a point with a drastic drop of the specific volume at a certain temperature. Differently from amorphous polymers, the phase transition of crystalline polymers occurs in a rather wide temperature interval, which depends on the pressure. This pressure-dependent transition, enables the formation of an ordered structure.

1.2.5 Effect on mechanical properties

The mechanical properties of the materials can be determined by different experimental tests, from uniaxial to multiaxial loads. As depicted in Figure 1.6, polymers can exhibit different behaviours depending on their internal molecular structure.

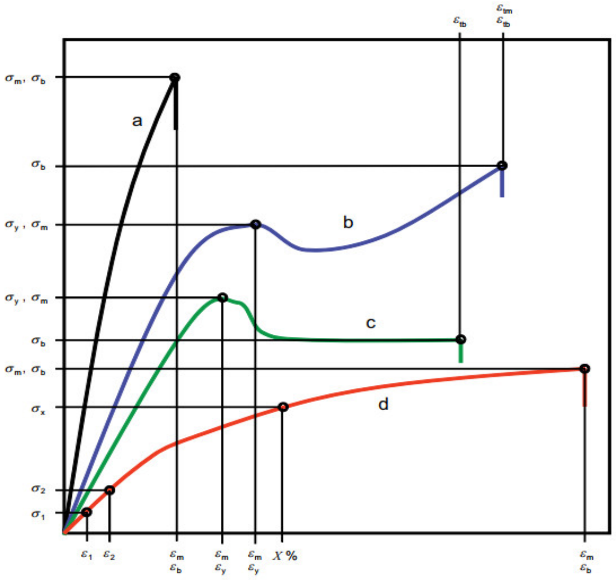

Figure 1.6: Example of stress-strain curves of polymers. Reproduced from [2].

Therefore, it is possible to classify several material behaviours:

a. Brittle (e.g., PC, PMMA, SAN)

b. Semi-ductile (e.g., ABS, PA, PEEK)

c. Ductile (e.g., PET, PP, PBT)

d. Elastomeric (e.g., TPU, urethane, natural rubber)

The mechanical properties are not only dependent on the molecular mobility of the polymer chains, but are determined also from other variables, as temperature and strain rate variation [29]. In particular, the effect of temperature brings the material to be more ductile and therefore softer (Figure 1.7(a)). This happens because, increasing the temperature, the movement of molecular chains is triggered, resulting in a significant higher failure strain [30]. Conversely, the effect of strain rate (Figure 1.7(b)) increases the stiffness, making the material more brittle. The occurring of this behaviour is due to the not easy sliding of the molecular chains, resulting in a higher yield stress and low failure strain as the strain rate increase [31].

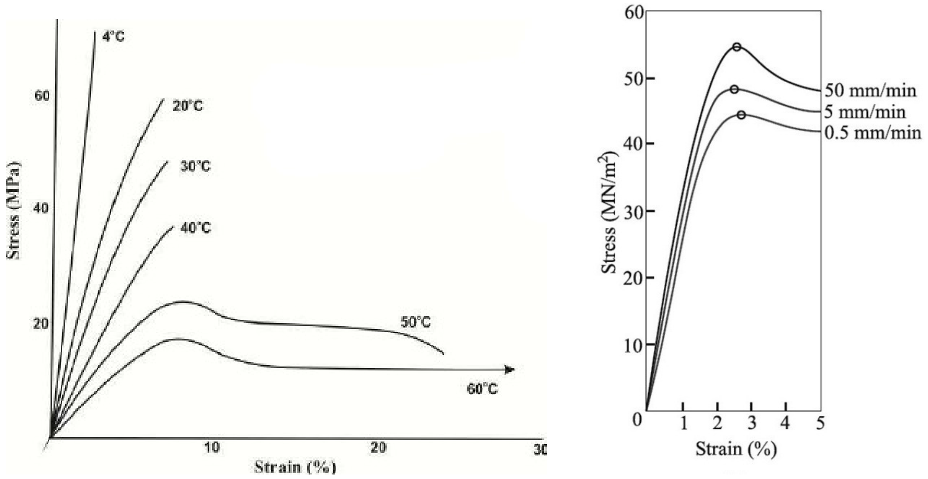

(a) (b)

Figure 1.7: Dependence of temperature (a) and strain rate (b) on stress-strain curve. Reproduced from [3, 4].

1.2.6 Glass transition temperature and melting point

One of the main thermal analysis, used to characterize many types of material, including polymers, is the Differential Scanning Calorimetry (DSC). This technique consist in heating and cooling, a small quantity of material, in a controlled manner. In this way, when a polymeric material is subjected to a state change, an alteration of the heat-flow can be visible. The variation of the heat-flow, can be exothermic or endothermic, depending on whether the transformation involves a transfer of heat from the system to the environment or vice versa.

The Figure 1.8 depicts the thermal history of a crystalline material, obtained by a DSC analysis. Noticeable are two important peaks of the heat flow, that are used to identify two specific temperatures: the melting temperature (T_m) and crystallization temperature (T_c). The melting temperature is the temperature corresponding to the maximum point of the endothermic alteration (upward peak), observed during the heating phase of the analysis. On the other hand, in the course of the cooling phase, the crystallization temperature occurs, corresponding to the temperature at the minimum point of the exothermic alteration (downward peak). In addition, from the graph it is possible to determine another temperature, namely glass transition temperature (T_g), which is noted with a change in the baseline during the heating phase. At the glass transition temperature, the material exhibits two different behaviours: hard and brittle when the temperature is below T_g, called glassy state; soft when the temperature rises above T_g, called rubbery state.

This example refers to the case of crystalline polymers, where considerable three-dimensional ordered molecular structures and long-range order can be found [32]. In contrast, for an amorphous material, neither crystallization peak nor significant

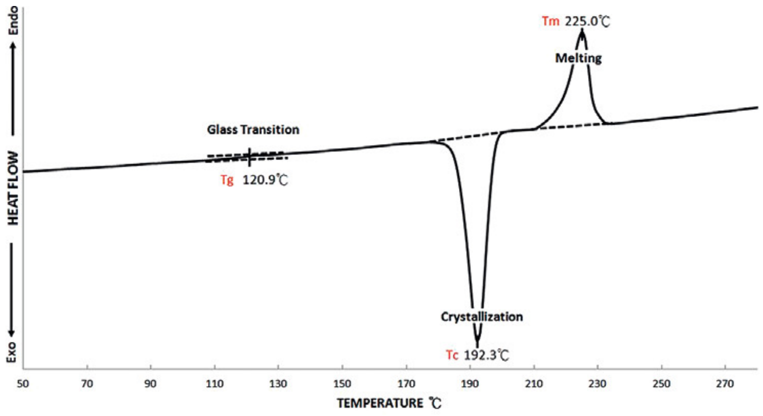

Figure 1.8: Thermal history of a crystalline material, obtained by a DSC analysis. Reproduced from [5].

melting peak would be observed. For this kind of polymers, the distribution of the chains is completely random (as shown in Figure 1.4(a)) and the chains exhibit a limited amount of short-range order [33].

1.2.7 Stiffness evolution of a plastic material

Polymers are called viscoelastic materials for their time-dependent [34] mechanical behaviour. Viscoelastic properties can be measured by Dynamic Mechanical Analysis (DMA), in order to determine the Storage Modulus (E'), which measures stored energy and is related to elastic behaviour. Using DMA, it is possible to determine the variation of Storage modulus as a function of temperature. As described above, thermoplastic polymers can be divided into two families: amorphous and semi-crystalline.

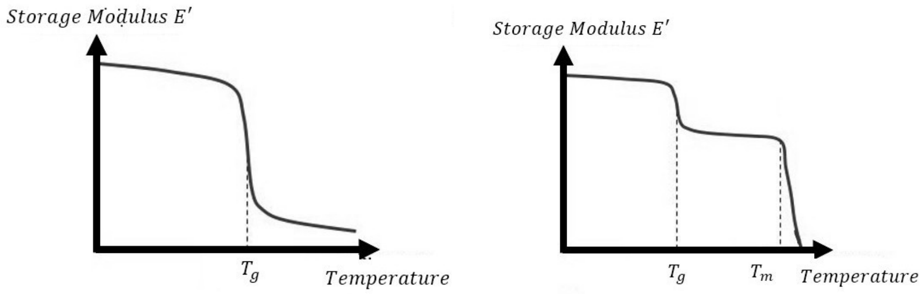

(a)

(b)

Figure 1.9: DMA Storage modulus E' vs. Temperature for an amorphous (a) polymer and semi-crystalline (b) polymer.

Amorphous materials are characterized by a temperature, known as the glass transition temperature (T_g) as shown in Figure 1.9(a). This temperature represents a point where mechanical behaviour of the material changes from a rigid to a rubbery state [35]. In particular, as the temperature rises above T_g, the material is in the rubbery state. In this state, the material becomes soft, and the molecular chains remain bound together in a tangle that is difficult to untangle. Despite the molecules have a high mobility and behave like a rubber material, at this temperature it is not possible to transform the polymer, because the molecules would turn back once the forces applied to make them slide cease. This means that for a good transformation process, it is necessary to operate at temperatures much higher than T_g.

On the other hand, as depicted in Figure 1.9(b), semi-crystalline polymers shows two characteristic temperatures: T_g, for the amorphous part, and T_m for the crystalline part [36].

1.3 Smart materials

1.3.1 Introduction to Smart Materials

The words smart materials refer to a class of carefully designed materials that can physically or chemically change their properties, by responding to specific environmental stimuli, such as heat, magnetism, electricity, moisture, and so on. For this kind of materials, nature has been a source of inspiration to develop the reactive stimuli systems (e.g., the camouflaging ability of a chameleon to change the colour of its body to adapt to the surroundings or the defence mechanism of certain types of plants, which when annoyed, release various chemicals, resulting in the closure of their leaves).

Differently from conventional materials, smart materials react to the environment and conditions in which they are placed, in order to provide solutions that overcome the problem. Basically, when conventional materials are subjected to temperature will become soft, enabling the possibility to be molded into the desired shape. Applying the same temperature again, the resulting deformed shape will not return to its initial shape unless an external force is exerted. On the contrary, many intelligent materials such as Shape Memory Materials (SMMs) behave differently in these situations, thus defying the so far known rules of general material behaviour.

Indeed, the peculiarity of SMMs is the shape-shifting property, that is the capability of changing its shape from the original (also named permanent) shape to a temporary one and vice versa [37] as depicted in Figure 1.10. This transformation phenomenon is named the shape memory effect (SME).

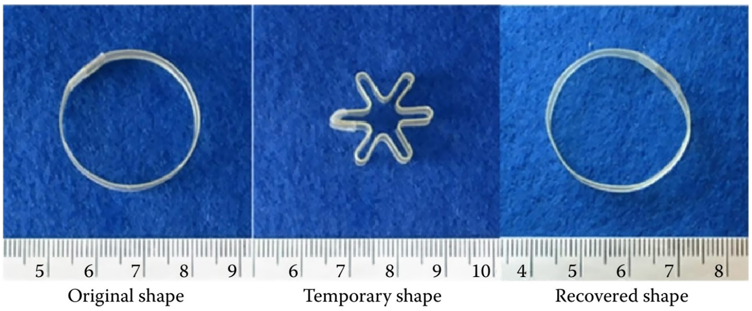

Original shape Temporary shape Recovered shape

Figure 1.10: SME. Reproduced from [6].

SMMs are functional materials for numerous applications, due to the possibility to change their shape. In particular, the capabilities of this sub-category of smart materials, such as actuation and control, are inherently built into the microstructure of such materials to react to changing environmental conditions.

Materials showing SME can be classified as shape memory alloy (SMAs), shape memory polymers (SMPs), shape memory hybrids (SMHs), shape memory ceramics (SMCs), and shape memory gels (SMGs), which can form composite materials generally termed shape memory composites (SMCs) as depicted in Figure 1.11.

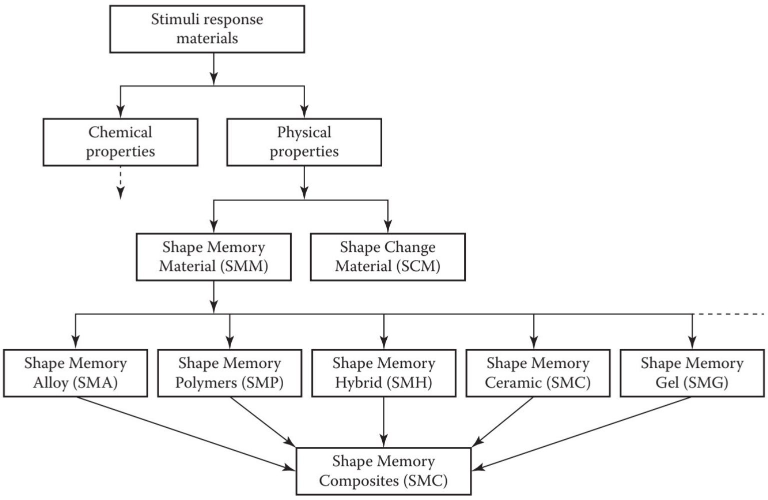

Figure 1.11: SMM domain. Reproduced from [6].

1.3.2 Shape Memory Polymers

Polymers having the ability to memorize a temporary shape, that is fixed under appropriate conditions, by an original shape are called SMPs.

In general, SMPs are different compared to other SMMs, due to their excellent properties such as a remarkable recovery strain (up to 400% compared to a low 8% for metal alloys), are resistant to very aggressive biological fluids (which could corrode metals), low-cost fabrication, biocompatible and biodegradable. In particular, an excellent property is the possibility of trigger the shape changes under different various nature of external stimuli, such as thermal load, humidity [38], electromagnetic [39], electricity [40], light [41], and some specific chemicals [42].

The external stimuli act to an alteration of the polymer's active cross-linked molecular architecture, thus altering the stability at the macroscopic level and allowing the change of the shape from temporary/original.

In fact, in recent years, SMPs received considerable attention in the research community in different application fields, such as propulsion [43], self-folding [44], 4D printing [45], robotics [46], aerospace [47] and biomedical devices [48].

1.3.3 Shape Memory Effect

Among all the external stimulus to activate the SME, the most commonly used in the SMPs is the thermal load. According to Giuliano et al. [49], the SME is strictly related to the different properties of the "hard segments", storing the original shape, and the "soft segments", which allow for temporary shape changes above a certain shape transition temperature. Concerning the polymers, the critical transition temperature at which their physical properties change is the transition temperature (T_{trans}) [50]. However, the activation of SME depends on both the molecular architecture of

SMPs and an appropriate programming sequence of external stimuli [51]. A complete programming sequence includes a shape modification phase and a shape recovery phase as shown in Figure 1.12. In the first one, after heating the SMP above the transition temperature ($T > T_{trans}$, where T is the current temperature of the polymer), the mechanical properties of the polymer are modified and a deformed shape is achieved, by means of an external load. This condition is held by a subsequent cooling below the transition temperature ($T < T_{trans}$), which brings the material into a metastable temporary shape. In the second phase, the original shape can be recovered by removing the mechanical load and heating again above the transition temperature, without applying constraint or loads.

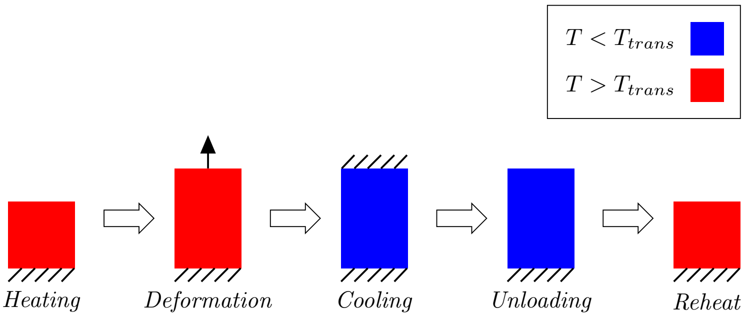

Figure 1.12: Shape memory effect cycle.

The SME is also predominantly an entropic phenomenon, where both the original macroscopic shape and the molecular chains are in a thermodynamically stable state [52]. More specifically, when heating is imposed to perform the programming sequence, the polymer assumes the conformation at the state of maximum entropy. Then, since the material is above the glass transition region, the deformation results easier to be applied, thanks to a significant mobility of the polymer chains. According to Guan et al. [53], the polymer's deformation determines also an alteration in the entropy state. Hence, when an external load is applied, the conformation of the molecular chains changes, achieving a more organized temporary shape with a lower entropy state. In addition, the strain rate influences the relative mobility of macromolecules [54], which can slip more easily among each other at low rates. Going on through the programming sequence, during the cooling phase, the reached entropic state is confined in the polymer chains, especially when the temperature reaches the glassy region, corresponding to a macroscopic shape fixation. Finally, when reheating the material again above T_{trans}, the molecular mobility is reactivated, facilitating the molecular chains to return to their maximum entropy state and recover their original shape [52].

1.3.4 Thermomechanical tests

In order to characterize the behaviour of SMPs, a thermomechanical experimental test was conducted. A three-dimensional schematic representation of the cycle for characterizing the behaviour of a SMP is shown in Figure 1.13. Previously, in literature, this cycle has been described by Tobushi et al. (1996) [55]. After an initial heating,

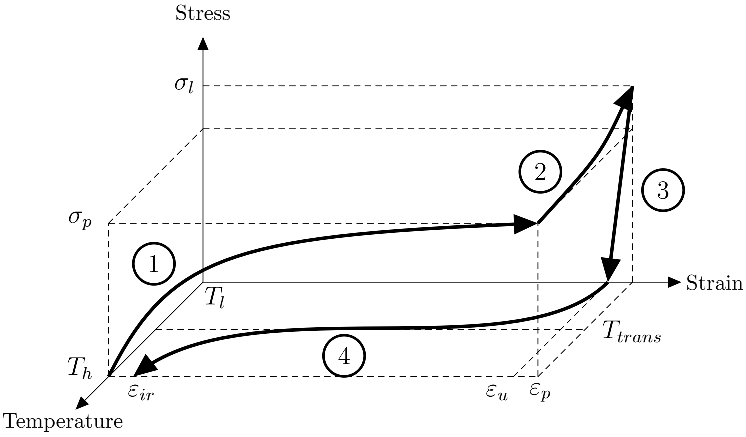

Figure 1.13: Schematic of typical SMP material thermomechanical cycles.

the cycle consists of four steps (i.e., loading, cooling, unloading and reheating) during which temperature and stress or strain are controlled:

- *Step* 1, *Loading*: the specimen is deformed up to a prescribed value of strain ε_p at temperature T_h (above T_{trans}).

- *Step* 2, *Cooling*: the specimen is rapidly cooled to temperature T_l (below T_{trans}), while maintaining the prescribed strain. In these two steps, a new temporary shape is imprinted to the specimen.

- *Step* 3, *Unloading*: the specimen retains this new shape, except for a small amount of strain. At this stage, the specimen maintains a strain ε_u slightly lower than the imprinted one ε_p. Hence, the shape Fixity ratio is defined as

$$R_f = \frac{\varepsilon_u}{\varepsilon_p} \times 100 \tag{1.1}$$

  and represents the quantity of imposed strain ε_p that the material is able to effectively store. R_f is a number ranging between 0 and 100: a ratio equal to 100 represents the ideal material behaviour, meaning that the specimen maintain all the initially imposed deformation after the loading step.

- *Step* 4, *Reheating*: it consists in heating from T_l to T_h where no loads are applied to the material. The original shape is therefore recovered, except for a small, irrecoverable, amount of strain, ε_{ir}. Hence, it is possible to define a shape Recovery ratio:

$$R_r = \frac{\varepsilon_p - \varepsilon_{ir}}{\varepsilon_p} \times 100 \tag{1.2}$$

which represents the quantity of the imposed strain ε_p that the material is able to recover. R_r is a number included between 0 and 100: a ratio equal to 100 represents the ideal material behaviour, meaning that the deformed specimen recovers all the initially imposed deformation after being heated in the last step.

These two parameters reported in Equation 1.1 and 1.2 are important to evaluate how the material is reliable in maintaining and recovering the imprinted shape.

1.3.5 Shape Memory Polyurethanes

Thermoplastic SMPs could be obtained by traditional processing techniques. Together with the presence of weak bonds and the capability to easily achieve the melting temperature, these properties makes the class of thermoplastic polymers suitable for several processes either in the heat-softened state (e.g., by thermoforming [27]) or in the liquid state allowing to mold into a wide range of manufactures shapes (e.g., by extrusion and injection molding [28]).

As compared with other SMMs, mostly used in several application fields, the thermoplastic Shape Memory Polyurethanes (SMPUs), has some important characteristics and advantages, such as: low density, excellent chemical properties and biocompatibility [56], high memory performance, can be used in injection molding process and the possibility to easily modify the transition temperature (T_{trans}), by means of a proper modulation of the chain blocks [57].

Moreover, SMPUs are characterized by a wide range of glass transition region, whereby the polymer stiffness change gradually and elasticity like rubber attitude is observed [58]. Shape memory polyurethanes polymers are different from conventional polyurethanes (PUs) [59], in presenting heterogeneous structure and morphology with two-phases: hard-segment and soft-segment phase. In particular, the hard segments link together the soft segments, while the soft segments works as reversible molecular switches, showing a thermal transition temperature T_{trans}. Additionally, to exhibit good shape memory properties, the hard segment percentage content in the polymer, should be high enough in order to prevent the plastic flow of the chains that are responsible for memorizing the temporary shape.

Segmented PUs are typically produced from three basic starting materials:

- Diisocyanate
- Long-chain polyether or polyester macrodiols with a high thermal transition temperature such as T_g or T_m as the hard segment
- Short-chain chain extender, a diol, and/or a diamine with lower T_g or T_m as the switching segment

More specifically, hard segment are obtained by the reaction between the diisocyanate and the chain extender, while the soft segments between them are formed from the long-chain polyether or polyester macrodiol. Scheme shows below represent the typical two-step prepolymer method that is usually employed for the production of thermoplastic PU elastomers.

$$\mathrm{HO}\text{——}\quad\text{——}\mathrm{OH} + \mathrm{nOCN}\text{——}\mathrm{NCO}$$

In this process, isocyanate-terminated prepolymers are obtained by the reaction of a long chain diol with an excess of a low molecular weight diisocyanate. A diol, at the left in the chemical reaction, is a chemical compound containing two hydroxyl groups -OH. Diisocyanate, at the right in the chemical reaction, it is used in the addition reaction with the polyols to form polyurethanes.

In the second reaction step, in order to couple these prepolymers, the low molecular chain-extender is added.

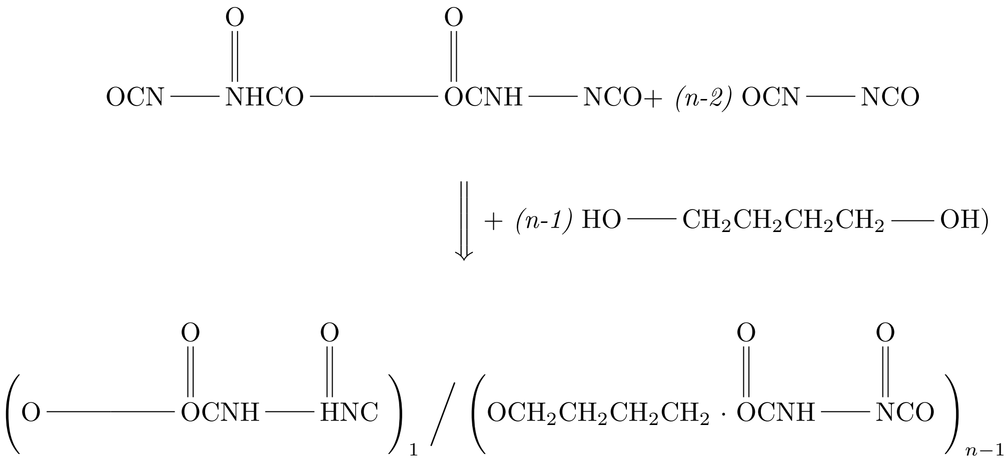

$$\mathrm{OCN}\text{——}\overset{\mathrm{O}}{\overset{\|}{\mathrm{N}}}\mathrm{HCO}\text{————}\overset{\mathrm{O}}{\overset{\|}{\mathrm{O}}}\mathrm{CNH}\text{——}\mathrm{NCO}+\ \textit{(n-2)}\ \mathrm{OCN}\text{——}\mathrm{NCO}$$

$$\Big\Downarrow +\ \textit{(n-1)}\ \mathrm{HO}\text{——}\mathrm{CH_2CH_2CH_2CH_2}\text{——}\mathrm{OH)}$$

$$\left(\mathrm{O}\text{————}\overset{\mathrm{O}}{\overset{\|}{\mathrm{O}}}\mathrm{CNH}\text{——}\overset{\mathrm{O}}{\overset{\|}{\mathrm{H}}}\mathrm{NC}\right)_1 \Big/ \left(\mathrm{OCH_2CH_2CH_2CH_2}\cdot\overset{\mathrm{O}}{\overset{\|}{\mathrm{O}}}\mathrm{CNH}\text{——}\overset{\mathrm{O}}{\overset{\|}{\mathrm{N}}}\mathrm{CO}\right)_{n-1}$$

In this way, linear and phase-segregated PU- or PU-urea block copolymers are obtained, which are characterized by a microphase morphology that depending on the chemical composition and the length of the segment.

1.4 The injection molding of thermoplastic polymers

Injection molding is the most useful process used for mass production of plastic parts. Generally, in this process, the plastic material is melted and injected at high pressure into a closed mold, which is opened after solidification of the part. This versatile process can be used to obtain consumable parts or high quality and durability components. The injection molding process is used in many applications fields, such as automotive, aerospace, packaging, electronics and medical.

The polymer used for this process, is generally provided as pellets. The material is firstly dried, to remove the moisture, then injected into a clamped mold (made in steel or aluminium). At this point, the melt inside the mold is cool down until the ejection temperature is reached. This process is suitable to manufacture products from simple to complex geometry, of different dimensions and with several kinds of polymers.

The high production rate of the injection molding process, makes the costs of the plastic parts extremely low. However, there are some drawbacks as initial capital cost of the injection machines and molds. The quality of the final components depend mainly on mold design and process control.

1.4.1 The Injection Molding Machine

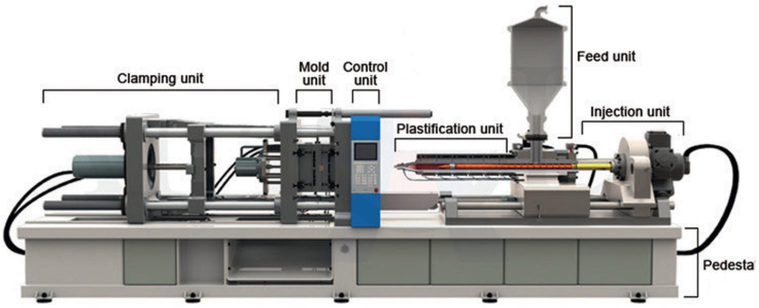

Figure 1.14: Injection Molding Machine. Reproduced from [5].

An injection molding machine as shown in Figure 1.15, is composed of six main unit: Injection, Feed, Plastification, Control, Mold and Clamping unit.

Initially, the material is loaded in a feed hopper (feed unit) and by an appropriate control systems, at each molding cycle, the correct quantity of materials to realize the part is introduced in the cavity. In order to fill the cavity, the material passes into a barrel (plastification unit), who through heating resistances and a screw with suitable geometry rotate inside a cylinder, enabling the preparation of the melt before injection. The screw inside the cylinder has a constant pitch worm screw with a variable core diameter and is composed of 3 zones, as shown in Figure 1.15. The first zone is the feeding one, where the temperature is low in respect to the melting point of the material and the heating is generated only by heaters bands. The other two zones are the compression and the metering zone, where the temperature is higher than the melting temperature and increasing as it moves towards the nozzle. In these zones, the material is subjected to both mechanical friction and the heaters. At the end of the screw in the cylinder, there is a back-flow valve which does not allow flow back to the molten material during the filling phase. In this way, with an advance of the screw by means of a hydraulic piston (injection unit), the material is forced into the mold cavity (mold unit). With the purpose of achieve the desired shape, the mold is kept closed during the filling and cooling phase, by means of toogle movements systems (clamping unit). Additionally, the mold must be suitably designed with cooling channels depending on the material used and the shape of the cavity. Finally, the last unit is the control one, for ensures good repeatability and manages the main process parameters such as: Mold Temperature, Melt Temperature, Injection Speed, Packing Pressure, Packing and Cooling Time.

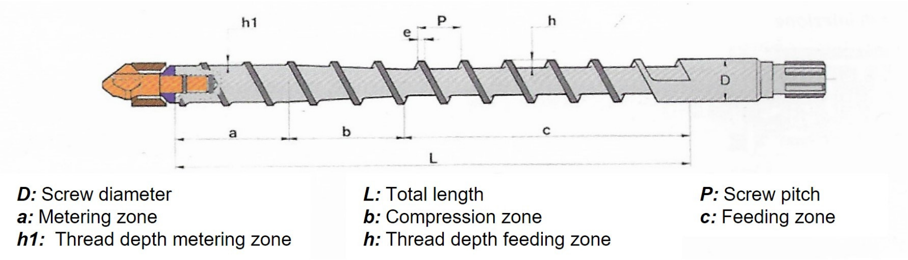

Figure 1.15: Injection Molding screw. Reproduced from [7].

1.4.2 The Cycle of Injection Molding

Injection molding is a process repeated cyclically for making a product and it is composed of 4 main operations, as shown in Figure 1.16.

The first phase is the filling phase, in which the mold is closed and initially empty. In this phase, the injection molding machine controls the speed of the screw (volumetric control), which moves forward until almost the entire amount of material into the cavity is injected (about 95-98% of the cavity volume). At this point, the machine changes from speed control of the screw to pressure control. This process step is called V/P switch-over and represents the beginning of the holding phase.

Generally, in the holding phase, the screw continues to move slowly until it reaches the pressure indicated by the operator. This causes, the continues flow of a small amount of material into the mold and is used to compensate the shrinkage and the deformation of the part. The packing phase ends when the gate for the mold cavity is frozen.

Once the holding phase is over, the cooling phase begins and the screw moves backwards rotating to prepare a new charge for the following cycle. When the material arrive at the ejection temperature the cooling phase ends, the mold opens and the part is ejected. After the ejection of the part, the mold closes and the machine reaches a set clamping force to contrast the pressure that will be reached in the next injection

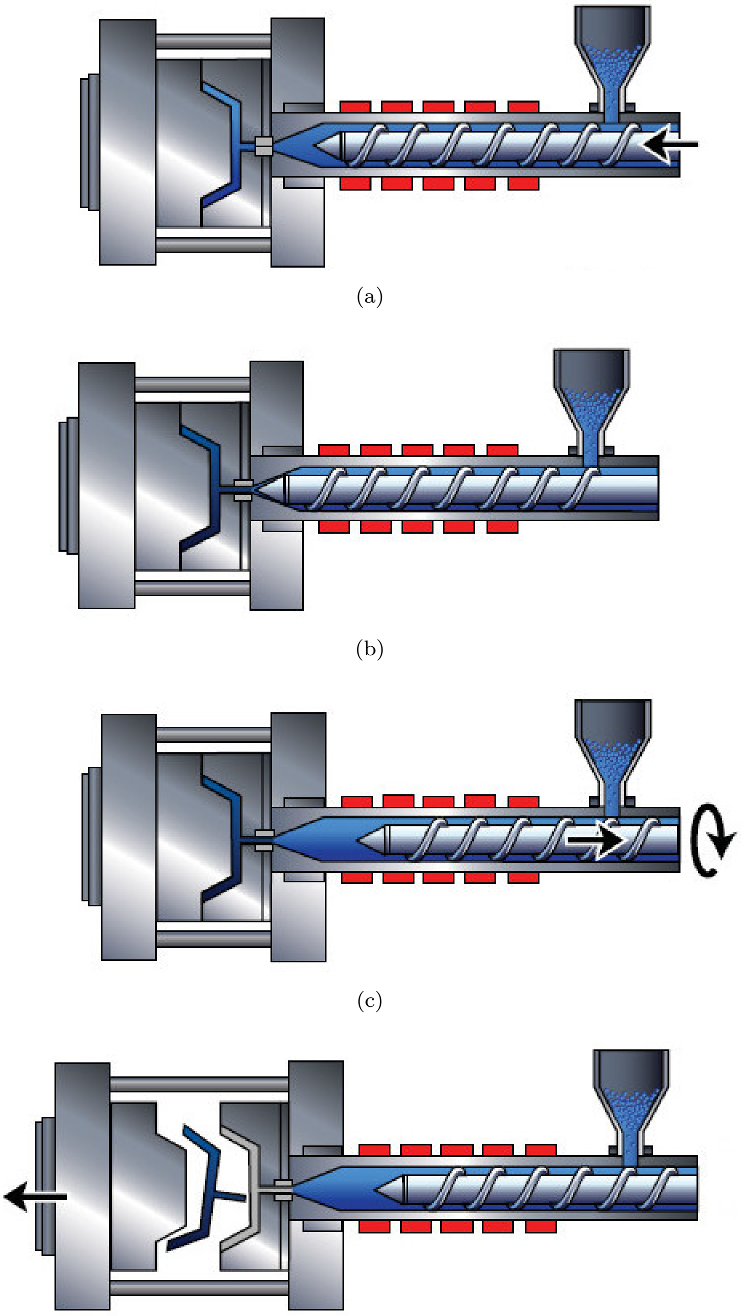

(a)

(b)

(c)

(d)

Figure 1.16: Phase of process: Filling phase (a), Packing phase (a), Cooling phase (a), Ejection phase (a). Reproduced from [8].

cycle.

The Figure 1.17 shows in the 3 rings a schematic overlapped cycle timelines. In particular, the outermost ring represents the process steps, while the middle and inner rings represent the movements of the screw and the mold respectively. Regarding the second ring, it is possible to notice that the screw has three movements within the process. The first one starts at zero time in which the screw, which acts as a piston, generates the flow of material in the injection phase and in the maintenance phase. The second phase is the plasticization, which occurs with the rotation of the screw and therefore the introduction of material from the feed hopper in the cylinder. Finally, there is a phase in which the screw remains stationary during the opening and closing time of the mold. Differently, the movement of the mold during the process are only two. At time zero the mold is closed and will open only in the last phase of the process, when the material inside the cavity reach the ejection temperature.

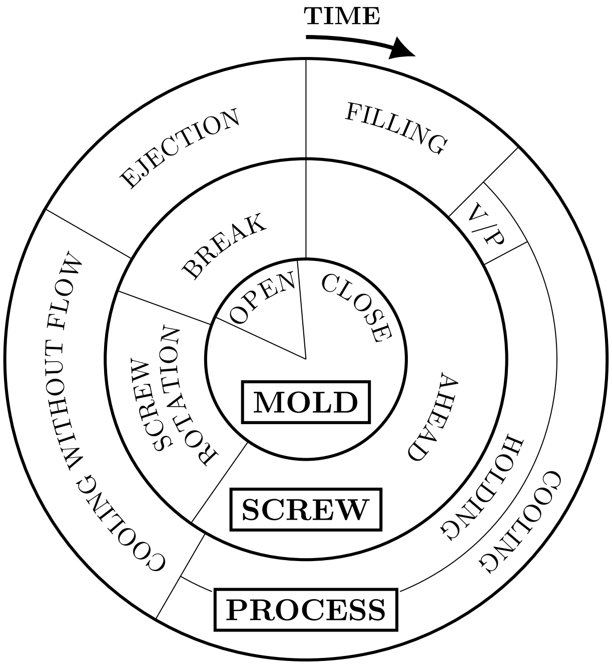

Figure 1.17: Phase of process. Reproduced from [9].

1.4.3 Plastic melt in the cavity

The phase of pushing the melt into the cavity, represents the first phase of the molding process and could determine all kinds of defects in the part. During the filling phase the flow front of the material, which comes in contact with the cavity walls (as shown in Figure1.18), generates two different effects. The first effect generated, called fountain effect, is due to the molten mass of a fluid at high viscosity that forms a laminar flow

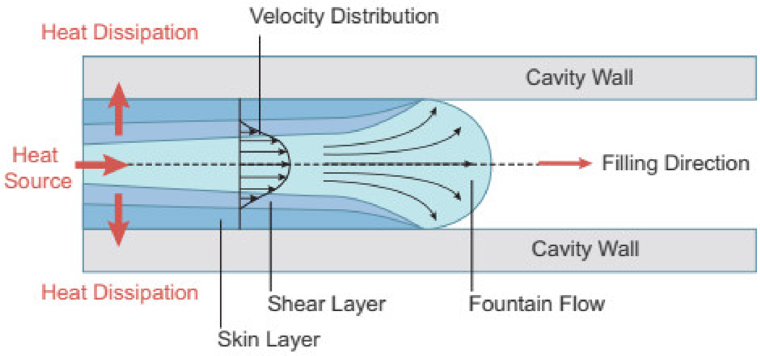

Figure 1.18: Polymer melt during filling process. Reproduced from [5].

when it is moving in the cavity. The name comes from the shape that the flow front takes, since the velocity is higher in the centre and lower at the sides, thus creating a fountain-shaped.

Otherwise, another effect that is generated in contact with the cavity walls is the skin effect, which is caused by the contact of the melt with the mold at low temperature. The high temperature variation causes a cooling of the surface layer in contact with the mold, reducing the flowing space of the melt. The flow of plastic can not be controlled when it is out of the nozzle, because the natural behaviour is flow in the direction with lower resistance. The only way to improve the movement of the melt inside the mold is by adjusting the flow rate according to the variation of the cavity's cross-sections. The cross-sectional velocity distribution inside the cavity, as depicted in Figure 1.19, generate also two different shear rate zones, namely shear layer and low shear rate area. The shear layer is characterized by a high speed difference to the skin layer and resulting in elongation and high orientation of the molecular chains. Differently, the low shear rate area is subject to a lower variation of speed with consequent low orientation of the molecular chains.

In addition, the flow rate is influenced by the thickness of the finished product, the mold and melt temperature. All these three aspects affect the shear and the skin layer thickness during the molding process. If the thickness of the part is thin, the shear rate and shear stress become higher, inducing a heating effect to the melt and reducing the skin layer. The same effect can be achieved by increasing the mold and melt temperature, thus decreasing the heat dissipation effect of the material. The flow of material within the cavity depends on the viscosity, which varies during the injection phase. This occurs because the temperature and shear rate to which the melt is subjected vary. It is essential, for this reason, to know the influence of viscosity on these factors.

Figure 1.20 shows the viscosity chart of a commercial Desmopan DP 3695AU. The viscosity is strongly dependent on the temperature and shear rate, in particular it decreases as shear rate increases. The curves in different colours represent the viscosity

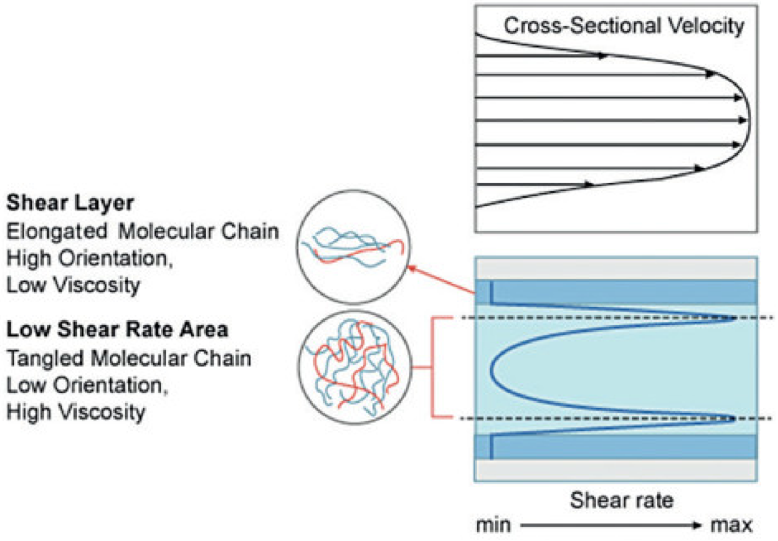

Figure 1.19: Steady laminar flow field of polymer melt. Reproduced from [5].

of the material at different temperatures. Observing the temperature curves (the curve of same colour), the viscosity decrease as the shear rate increases, while for a constant shear rate (same vertical line), the viscosity decrease as the temperature increases. Since the cross-section of the inlet gate is the smallest in the entire mold cavity, it also has the highest shear rate and therefore the temperature during the filling phase increases significantly, due to material friction. This condition, higher injection speeds, will help to fill the cavity; however, the polymer chains should not be subjected to excessively high shear stresses in order to avoid deterioration of the structure. When the melt reaches the filling end, the screw speed is reduced already and thus the shear rate is relatively lower as well as the temperature.

1.4.4 PVT variations during the Process

Once the mold is full, the holding phase begins, in which the screw continues to apply pressure to the front of the cylinder, which still contains a small amount of material, called cushion. This second step is important, as it is necessary to provide the material in the mold with shrinkage compensation during cooling, as well as to influence problems of part tolerances, sink marks, deformation, etc. Since the material in the mold cavity does not reach the various zones at the same time, and it is not even possible to achieve an ideal condition of temperature uniformity on the surface of the mold, the part solidifies inhomogeneously. Consequently, it is not possible to transfer the same pressure to each zone during the holding phase. This results in a different holding pressure from point to point, depending on the geometry of the part, resulting in shrinkage, warpage and different final properties. To understand more

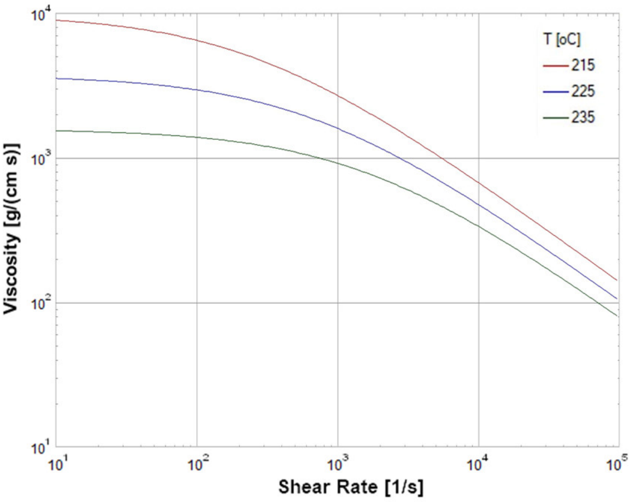

Figure 1.20: Viscosity of a commercial Desmopan DP 3695AU. Reproduced from Moldex3D Bank.

clearly the effect of holding pressure in the part, the evolution of the specific volume of a polymer should be considered, as shown in the PVT (pressure-volume-temperature) curves, shown in Figure 1.17. Once the material is placed in the hopper at room temperature and atmospheric pressure (point 1), it is heated by the electric heaters on the cylinder and by shear friction, thus becoming molten (point 2) and occupying the front of the screw, to be metered and ready for injection.

In the filling phase, the state of the melt in front of a screw and inside the mold cavity, is recorded. The melt is at low pressure (point 2) in the dosage section before being injected. When the melt is crushed by the injection speed, but still remains in front of the screw, it enters a state of high pressure (point 3). After being injected into the cavity, the melt temperature and the pressure drops due to the contact with the mold and the passage through the channels and gates, which results in a loss of pressure (point 4).

When the mold cavity is almost completely filled with melt (98-99%), the packing phase begins, in which continuous and constant pressure is applied to supply melt into the cavity and compensate the shrinkage of the material. During this phase, there is no more melt bringing heat into the cavity, so the heat entering the mold is less than that removed by the cooling channels, for this reason the temperature decreases rapidly (point 5).

Then, during the cooling phase, the screw moves back to prepare for the plastification of the next shot, while the melt inside the mold continues to cool. The material gradually solidifies, becoming solid when it returns to atmospheric pressure (point 6). The cooling phase ends when the temperature is low enough for the ejection phase.

When the part has cooled sufficiently to form a thick frozen layer, theoretically the ejectors would not damage the part. During this phase, the ejectors theoretically do

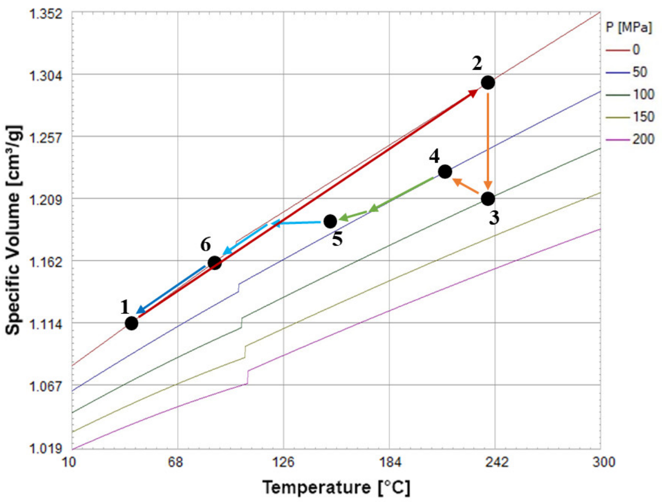

Figure 1.21: PVT of a commercial Desmopan DP 3695AU. Reproduced from Moldex3D Bank.

not damage the part, even if it is at higher than room temperature. Since there is no constraint for shrinkage after extraction, the deformation could be related to the geometry of the part, gravity and way of placing. Analysing this phase from the PVT curves, the temperature continues to decrease from the ejection temperature, as does the specific volume, which decreases, until it reaches room temperature (point 1).

In order to control the weight of the part, as much melt as possible should be pushed into the cavity before the end of packing. In this way, the difference in specific volume between the end of the holding phase (point 5) and the initial state (point 1) can be reduced to reduce the shrinkage.

1.4.5 Injection Molding Pressure

A typical pressure trend in injection molding is shown in Figure 1.22, the pressure is measured through the screw drive system. The pressure curves measured at the start and end of the part are also shown in the figure (red and blue curve respectively). The curve in the filling phase rises very slowly as the air inside the cavity is pushed out by the injected polymer. The melt reaches the gate of the part at the point G (2) and the pressure rises very rapidly, given the low compressibility of the polymer melt compared to the air. Once the melt reaches point E, the filling phase is complete (3) and the pressure is at its maximum at point G (4). From this point onwards the packing phase begins, in which the machine is set with a gradual reduction in pressure on the cavity, while the temperature in the mold decreases. At the end of the first packing phase (5) at point E, the pressure drops to zero (6). When the gate is frozen (7) so the packing phase is finished, the pressure at point G drops to zero (8) and the part starts to shrink.

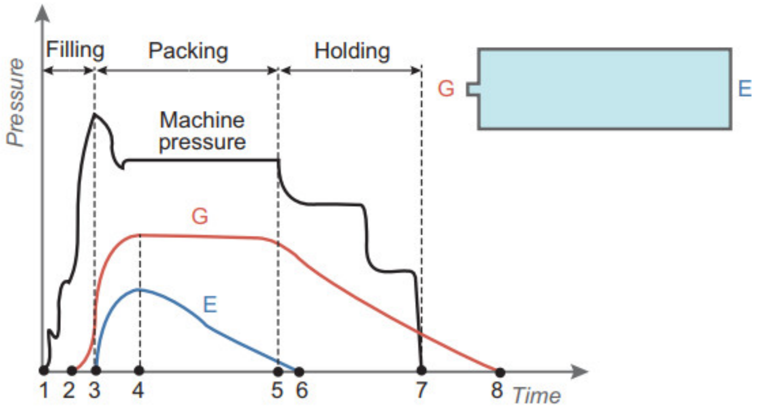

Figure 1.22: Melt pressure at different locations. Reproduced from [5].

1.5 Cavity measurements

1.5.1 The in-cavity condition

Nowadays, within the context of Industry 4.0 and the Internet of Things (IoT), a huge amount of data are needed for manufacturing process control, especially in the injection molding process that involves the production of high quality parts. The full control of injection molding involves three levels: Machine parameters, in-mold parameters and part quality control [60]. In fact, many times it is not possible to control or detect possible problems in the production process through machine parameters (e.g., gate freezing, melt compressibility and changes in melt viscosity), but it may be necessary and helpful to analyse what is happening inside the cavity to determines the quality of a finished part. For this reason, in-cavity control systems are increasingly being used to monitor the conditions inside the cavity. In many application fields, the most relevant data on the technological process, comes from the mold cavity through the use of sensors, which enable the quality of parts to be guaranteed [10]. Different kinds of sensors are available, for the in-cavity process control, the two predominant classes of sensors are pressure and temperature sensors [61]. Moreover, the use of sensors in the mold cavity allows automatic monitoring, but also optimization of the cycle time [62]. This results in waste reduction, reduction of energy costs, reduction of post-production control and the possibility to use a mold on different machine.

1.5.2 Cavity pressure measurement

In mass production, cavity pressure data are used to monitor and perform quality control on molded parts. In particular, their use is very useful in multi-cavity applications where a complete balance of mold filling is required. There are different types

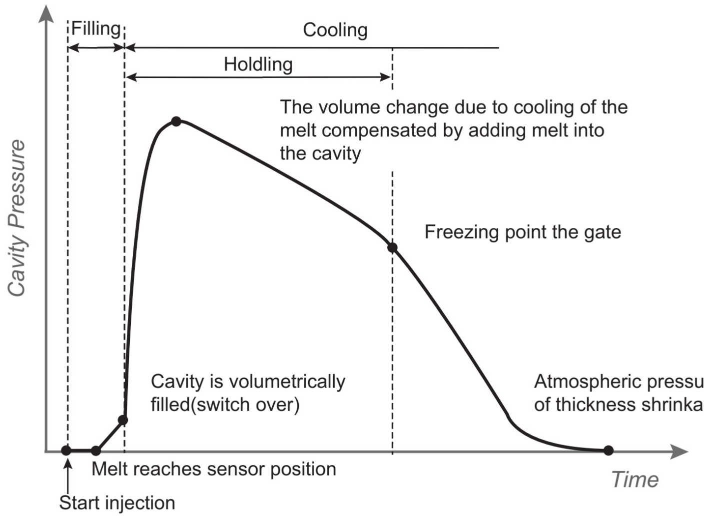

Figure 1.23: Pressure inside the cavity. Reproduced from [5].

of pressure sensors, the most commonly used being piezoelectric sensors, which are installed directly inside the cavity. Conversely, when it is not possible to touch the part directly, pressure sensors are placed on the back of an ejector which transfers the pressure to the sensor. In general, the right place to locate the pressure sensor is near the melt inlet into the mold, because more information can be gathered for the entire injection process. In Figure 1.23 is reported an example of pressure measured inside the cavity to the variation of injection time. Here it can be seen that pressure is transmitted mainly during the holding phase.

Starting from the filling phase, it is possible to monitor what is happening inside the cavity after the front flow of the material reaches the sensor. In this phase, the pressure inside the mold increases gradually and the rate at which pressure rises depends on injection speed, until the switch over point is reached. When the cavity volume is filled, the pressure increases rapidly to a maximum value directly depending on the holding pressure. During the holding phase, after the maximum pressure point is reached, the pressure decreases slowly until the gate is completely frozen. Once the gate freezing point has reached, the material can no longer be introduced into the cavity, achieving pressure drop at the end. Due to the difference PVT diagrams between semi-crystalline and amorphous, the compression behaviour will be different, in particular possible cavity pressure profile are shown in Figure 1.24. In amorphous polymers (Figure 1.24(a)), the cavity pressure decreases during the holding phase along with the decreasing temperature of the part, determining an increase in viscosity and no more transfer pressure from the machine. In contrast, in semi-crystalline polymers (Figure 1.24(b)), the cavity pressure is maintained for a longer time, until the part reaches freezing temperature. Below the freezing temperature, the crystallization of the polymer begins and volumetric contraction leads to a sharp drop in the measured pressure.

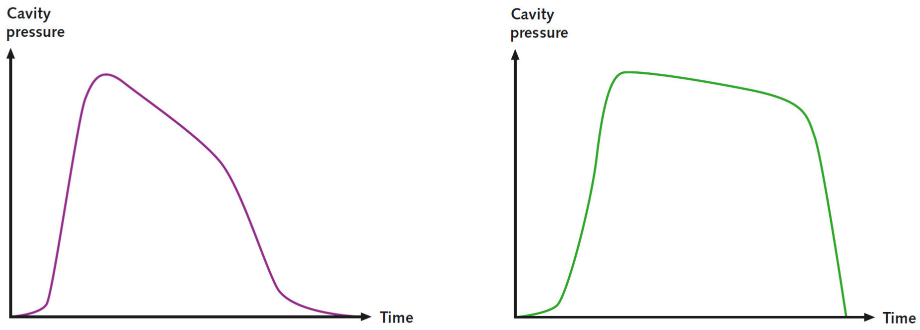

(a) (b)

Figure 1.24: Cavity amorphous (a) and semi-crystalline (b) pressure curve. Reproduced from Kistler catalogues.

1.5.3 Cavity temperature measurement

Cavity temperature sensors provide a much faster response than pressure sensors. They can be used for a variety of applications, such as: automatic balancing of multi-cavity molds by controlling the temperature of the hot runners; or used to determine the correct valve opening times in molds for large parts that require sequential filling. Generally, their use does not allow the temperature to be measured accurately, as the measurement is also influenced by the mold material surrounding the sensor. For this reason, the temperature sensor is often not employed to record the actual temperature in the cavity, but used to know the exact instant when the melt reaches a specific point.

There are two common types of temperature sensors: thermocouples and infrared (IR) sensors. The measuring principle of the first type is the same as for K-type thermocouples, with a light sensing element to ensure maximum responsiveness of the measurement. Differently, the second type is the IR type, which is used to measure the energy radiated by the molten polymer. Furthermore, since they are not affected by conductive and convective effects within the mold, they have a faster response than thermocouple-based sensors, as shown in Figure 1.25.

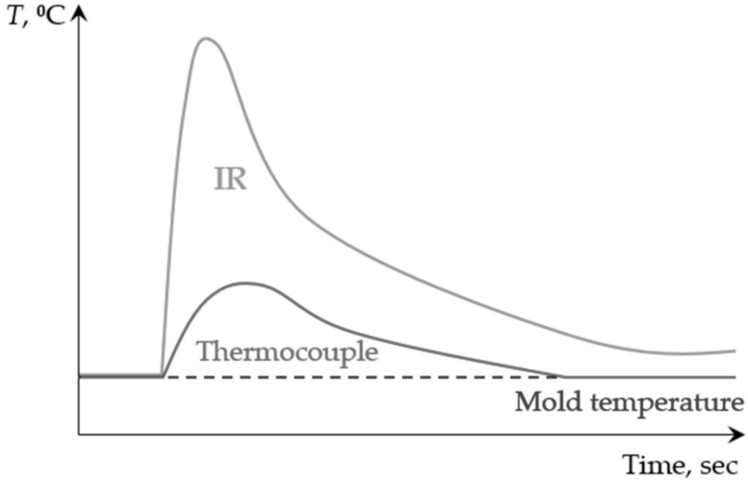

Figure 1.25: Comparison between IR and thermocouple sensors. Reproduced from [10].

In Figure 1.26 a typical pattern of temperature sensors is reported. The graph shows that until the melt front does not come in contact with the sensor, the recorded temperature is equal to the mold temperature, which is reached by the thermal conditioning effect of the cooling circuit. When the material reaches the temperature sensor, the signal increases very quickly, reaching a maximum peak considering all the surrounding effects, as described above. Finally, the temperature decreases more or less rapidly, depending on the efficiency of the cooling circuit in the area where the

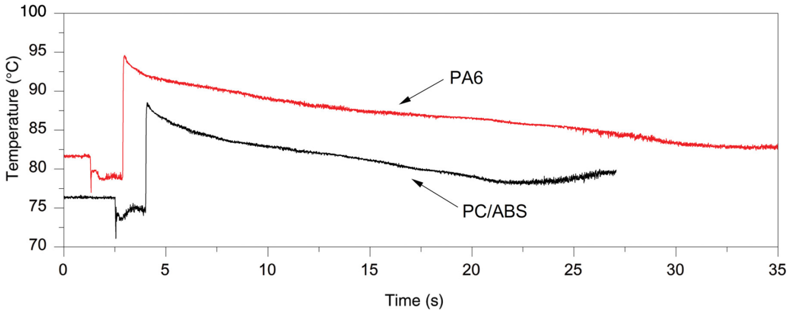

Figure 1.26: Temperature inside the cavity. Reproduced from [11].

sensor has been positioned.

1.5.4 Use of cavity temperature and pressure measurement

By analysing the signal from temperature and pressure sensors in the cavity, which are positioned in precise locations, it is possible to obtain information throughout the molding cycle. More specifically, when a pressure sensor is located near the gate entrance and the temperature sensor placed near the end of the fill cavity, material viscosity, including shear stress and shear rate and part compression can be monitored [63]. In particular, as depicted in Figure 1.27, the shear rate is calculated from the time Δt, that represent the flow distance between the pressure and the temperature sensor, while the shear stress is determined by ΔP at the time T1, in order to identified material viscosity variations from batch-to-batch.

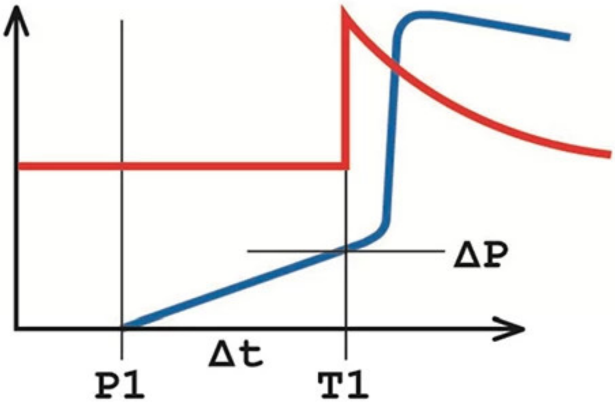

Figure 1.27: Priamus combined use of temperature and pressure sensors.

Chapter 2

Fabrication by Injection molding process

2.1 Instrumentation

The instrumentation used in this research activity consists of an injection molding machine, a polymer dryer, a temperature control system, the mold and a cavity measuring system. Specimens were molded by an injection molding machine (Arburg® Allrounder 370A). Before molding, the raw material was dried with a polymer dryer (Moretto® EH A V). A temperature control unit (Regloplas 90smart, capable to control the temperature up to 90°C) was used for the water thermoregulation, removing through a cooling channel on the mold, the transferred heat during the molding process. Regarding the mold and the in-cavity sensors will be discussed in detail in the following sections.

2.2 Mold design

2.2.1 Reference standards for mold design of thermoplastic specimens

In order to replicate a specimen with comparable properties, the mold was designed according to the ISO 294-1 [64]. The mold is able to manufacture different kind of specimens, such as a dog-bone (dimensions are defined in ISO 3167 — type A specimens [65]) or for rectangular bars typical of Charpy tests (type B mold). The main features for the construction of type A and type B ISO molds are reported as follows:

- the inlet feed channel diameter must be at least 4 mm
- the width and height (or diameter) of the secondary injection channels must be at least 5 mm
- cavities must have an inlet at one tip
- the inlet height must be at least two thirds of the cavity height and the inlet width must be equal to the cavity height, at the point where it enters the cavity

- the inlet must be as short as possible and must not exceed 3 mm in any case
- the draft angle of the secondary injection channels shall be at least 10°, without exceeding 30°. The draft angle of the cavity shall not be greater than 1°
- the main cavity dimensions must be in accordance with ISO 3167: thickness from 4.0 to 4.2 mm, central section width from 10.0 to 10.2 mm, length (mold type B) from 80 to 82 mm
- the heating/cooling system for the mold surfaces must be designed so that the temperature differences between each point on the surface cavity and between the plates are less than 5°Cunder operating conditions
- for multipurpose specimens molded with an ISO type A mold, it is recommended to use a cavity with a length of 170 mm
- multipurpose specimen molds must have secondary injection channels in the Z–or T–shape to balance the resulting force due to cavity pressure
- the cavity plate width can be influenced by the minimum distance between the connection points for the heating/cooling channels. In addition, a gap may be required in ISO type B molds for the installation of a special insert for the molding of notched bars for use in ISO 179
- the mold cavity surfaces must be carefully polished, with the polishing direction corresponding to the direction in which the specimen is loaded during the test

2.2.2 Mold description

Figure 2.1: Injection molding machine.

The design of the mold is mainly based on the specifications of the injection molding machine. In order to prevent the mold from opening due to the pressure inside the cavity, a permissible pressure was calculated as a function of the projected area. The injection molding machine available in the laboratory of the Polytechnic University of Marche is an Arburg® Allrounder 370A (Figure 2.1), whose main features are: 30 mm diameter screw, distance between tie-rods 370 × 370 mm, clamping force 600 kN and EUROMAP 170 injection unit.

The overall dimensions are shown in Figure 2.2, while the dimensions of the fixed and movable mold-holder plates are shown in Figure 2.3. In order to ensure anchoring and clamping, the thickness of the mold must be smaller than the maximum dimension of the clamping stroke between the two die plates.

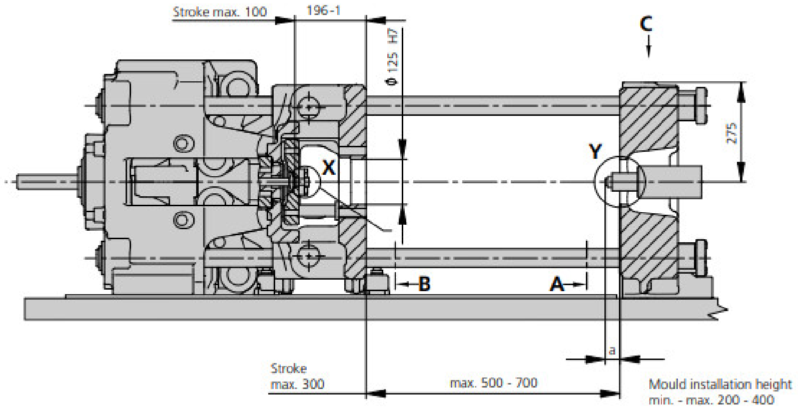

Figure 2.2: Arburg Allrounder 370A overall dimensions.

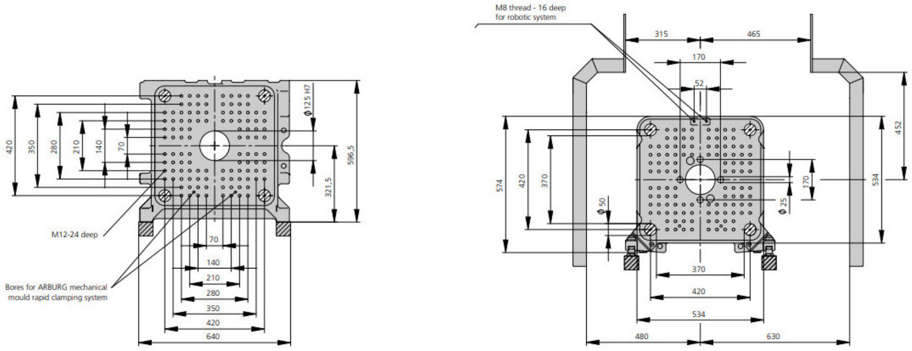

(a)

(b)

Figure 2.3: Fixed (a) and moving (b) mold mounting platen.

The mold thickness is therefore determined by 2 clamp plates to the machine 296 × 396 × 27 mm, a fixed cavity plate 296 × 296 × 76 mm, a movable cavity plate

296 × 296 × 76 mm and 2 parallel risers 296 × 44 × 86 mm, for a total of 292 mm, greater than the minimum required of 200 mm.

2.2.3 Design of the molding components

The mold was made in order to be able to realize specimens of different shapes according to the variety of mechanical tests, that can be carried out to characterize a material. In order to make the different sample shapes in one mold, the different cavities were arranged according to ISO standards. In particular:

- type A specimen for uniaxial tensile testing (ISO 527 [2])
- type B specimen for HDT test (Heat Deflection Test, ISO 75 [66])
- type B specimen for bending test (ISO 178 [67])
- type B specimen for Charpy test (ISO 179 [68])
- cylinder for quasi-static and high strain rate compression tests
- sacrificial ring in Hopkinson bar system [69]

The minimum mold die size was defined as a function of the largest specimen to be manufactured, which is the uniaxial test specimen. Runners were made for each type of specimen, which are feed from a single sprue gate in the centre of the figure. In particular, the different specimen shapes were arranged as shown in the Figure 2.4. In order to produce the Charpy specimens with or without notch, an insert was created to replace the figure in the same cavity. As for the ejectors, they have positioned under each figure to avoid a bending due to their pushing. The cold runners between the cavities are designed in a T-shape, according to the standards, with a U-shaped

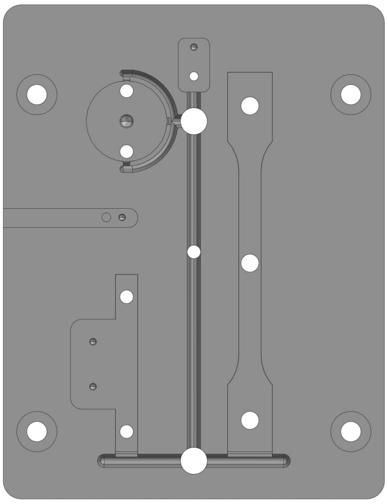

Figure 2.4: Mold die.

section, 6 mm wide and 4.5 mm high. In addition, flow selectors were provided at the T-nodes of the cold runners, in this way only the desired sample type could be produced. Cooling channels with 8 mm diameter were designed on both the core and cavity sides of the mold. Figure 2.5 shows wireframe core side, where are visible the molded part with the cooling channels. Finally, the side of the fixed plate have machined for the installation of Priamus pressure and temperature sensors, which will be described in the section 2.3. By using the sensors, it is possible to monitor the actual pressures and temperatures inside the mold cavity. Figure 2.6 shows the position of the sensors on the specimen.

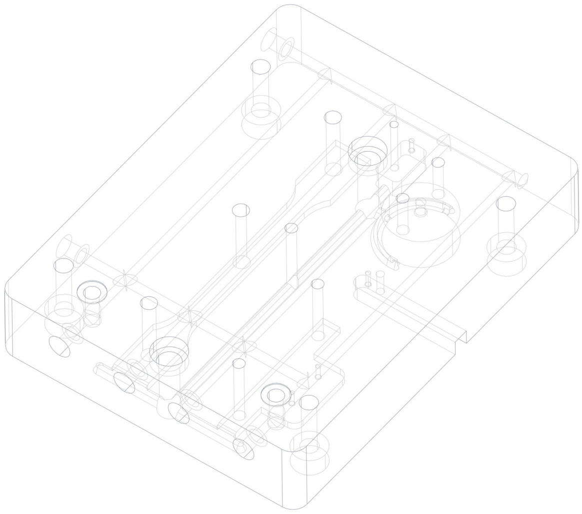

Figure 2.5: Wireframe representation core side.

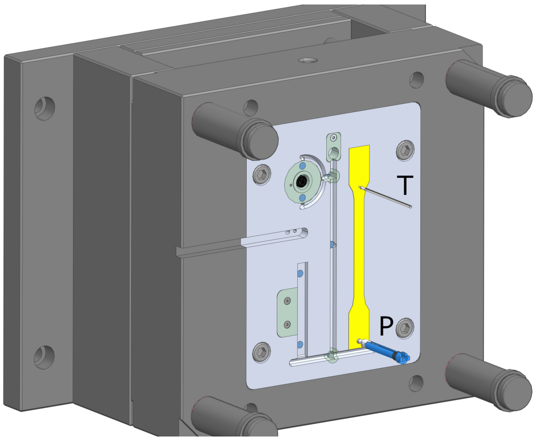

Figure 2.6: Machined mold and Sensor position on test specimen (where P indicates pressure sensor while T indicates temperature sensor respectively).

Exploded view of the mold is shown in Figure 2.7.

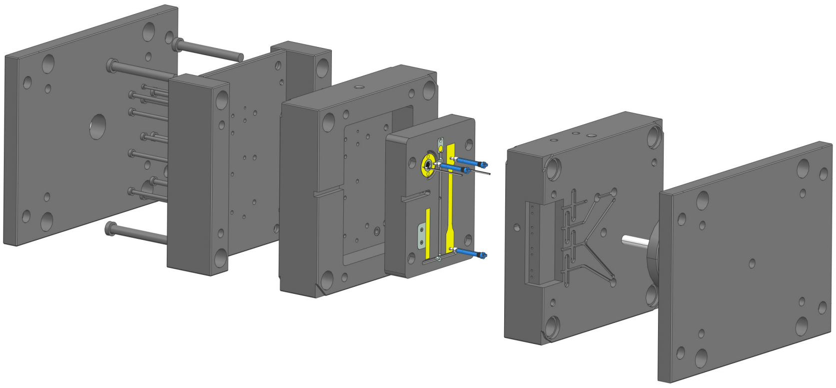

Figure 2.7: Exploded view of the mold.

2.3 Cavity Measurements

According to several experimental studies focused on injection molding [70], the injection parameters may affect the process cycle. Thus, the process stability and reliability were assessed through the analysis of cavity pressure and mold temperature, since they are the prevalent factors influencing the quality aspects of the produced specimen.

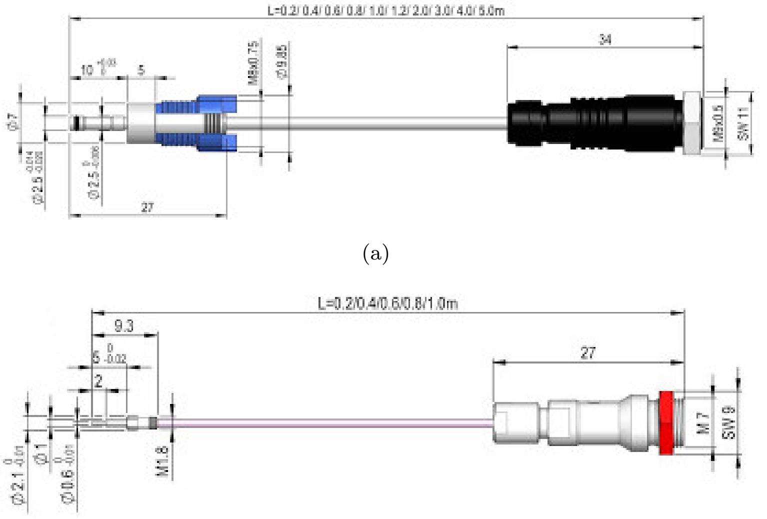

(a)

(b)

Figure 2.8: Pressure (a) and temperature (b) in-cavity sensors.

In particular, the in-cavity conditions were monitored by means of two sensors. The mold has been equipped with Priamus® pressure (Figure 2.8 (a)) and temperature (Figure 2.8 (b)) sensors [28], 6002Bx.x-102 and 4004Cx.x-101(-H) respectively. The main characteristics of the sensors are listed in Table 2.1 and Table 2.2.

Table 2.1: Priamus 6002Bx.x-102 specifications

Property	**Value**	**Unit**
Measuring range	0…2000	bar
Overload	2500	bar
Sensitivity	5	pC/bar
Maximum melt temperature	No limitation	°C
Maximum mold temperature	200	°C
Deviation of linearity	<±1	%
Natural frequency	>80	kHz
Insulation resistance	$>10^{13}$	Ω
Sensor front	machinable	

Table 2.2: Priamus 4004Cx.x-101(-H) specifications

Property	**Value**	**Unit**
Thermocouple	Type N	
Class	1	
Standard operating temperature	up to 600	°C
Operating temperature range (cable)	0. . . 200	°C
Operating pressure range	0. . . 2000	bar
Maximum deviations	dT=±0.004T or ±1.5	°C
Response time switch-over to holding pressure and sequential control with PRIAMUS amplifier	4	ms
Bending radius	12	mm

These sensors are placed inside the cavity along the dog-bone area: pressure sensor is near the specimen gate, while the other is on its end as depicted in Figure 2.9.

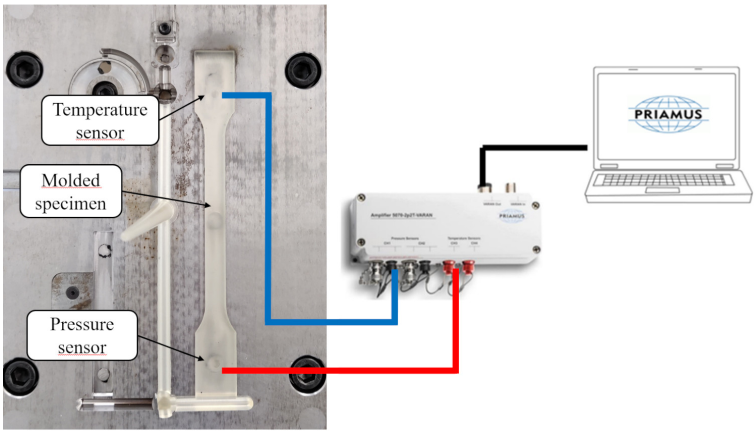

Figure 2.9: Sensors position.

The results given by these two sensors were carefully analysed to detect some possible defects of the samples and also optimize the process. In fact, the pressure transfer inside the cavity and the achievement of a homogeneous temperature after the cooling step represent potential issues in the injection molding process. In regard to SMPU both pressure and temperature mold settings are important aspects of proper molding process control.

2.4 Numerical model of the process

In order to better investigate the processability of SMPs, the injection molding process was simulated by Moldex3D® software. Initially, several simulations were carried out with the purpose of verifying if the designed mold was suitable to obtain a molding cycle, in terms of the dimensions of the feeding channels [71, 72] and the cooling channels [73, 74]. subsequently, the software was used to attempt an optimization of the molding cycle, before proceeding with the production of the test specimen.

2.4.1 Material properties

The material used in this study is a Polyurethane-based Shape Memory Polymer (SMPU), characterized by excellent recoverability of the deformation. The main physical and mechanical properties of this material are listed in Table 2.3, while in Table 2.4 are reported the recommended general processing parameters.

Table 2.3: Physical and Mechanical properties of SMPU

Property	**Value**	**Unit**	**Test Method**
Density	1200	kg/m^3	ISO 1183
Flexural Modulus (1 mm/min)	1900	MPa	ISO 178
Tensile Modulus (1 mm/min)	2066	MPa	ISO 527-2
Tensile Strain at Yield (1 mm/min)	3.3	%	ISO 527-2
Tensile Stress at Yield (1 mm/min)	58	MPa	ISO 527-2
Poison's ratio (1 mm/min)	0.29		

Table 2.4: General processing parameters of SMPU

Property	**Value**	**Unit**
Melt temperature	220 – 240	°C
Mold temperature	20 – 40	°C
Freeze temperature	120	°C
Injection speed	As high as possible	
Shrinkage	0.4 – 0.6	%
Screw back pressure	5 – 10	MPa
Surface temperature	5 – 10	°C under T_g

Since the rheological data of this material are not available in the Moldex3D® simulation software material library, an equivalent material, the Desmopan DP 3695AU with comparable characteristics, has used in the simulations. Some rheological properties have already been shown in Figure 1.20 and Figure 1.21 of section 1.3. Other relevant properties are:

- Density 1220 kg/m^3
- Ejection temperature 99.85 °C
- Freeze temperature 119.85 °C
- Melt temperature 215-235 °C
- Mold temperature 20-40 °C
- Tensile Modulus 2000 MPa

2.4.2 Numerical model description

The 3D geometry of the mold cavity was imported into Moldex3D$^{®}$ simulation software as an STP file and then processed to generate an STL mesh of the cavity surface, with a general mesh size of 1 mm (Figure 2.10). The complete model used to carry out the simulation is shown in Figure 2.11. The model consists of three main part: the specimen, the cooling channels and a control volume representing the mold.

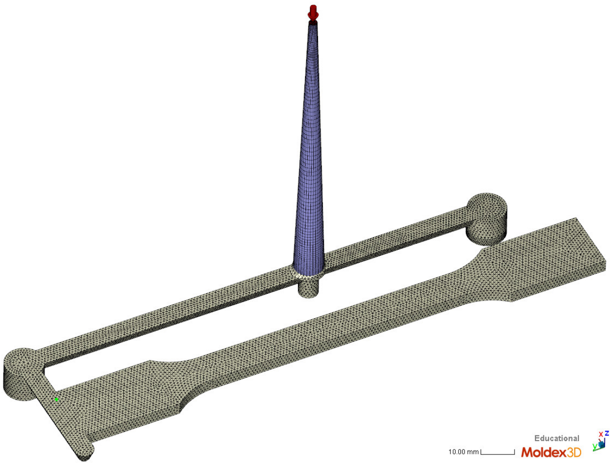

Figure 2.10: STL specimen mesh.

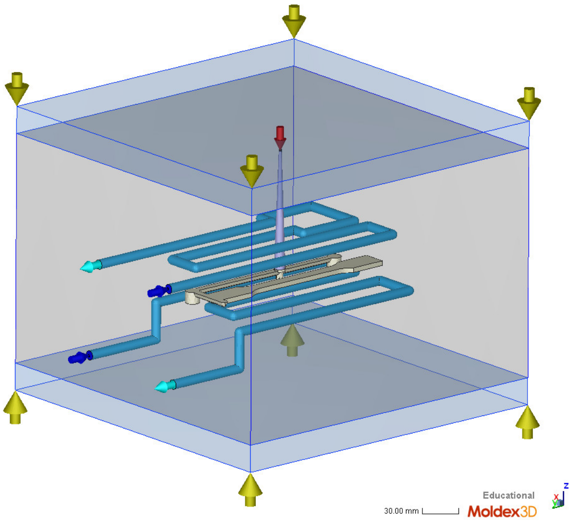

Figure 2.11: Numerical model of the mold.

The figure also depicts the boundary conditions, such as the melt entrance (represented by the red arrow) and the water inlets and outlets (represented by the blue arrows). In Figure 2.12 are reported other specific part of the model. As regards the

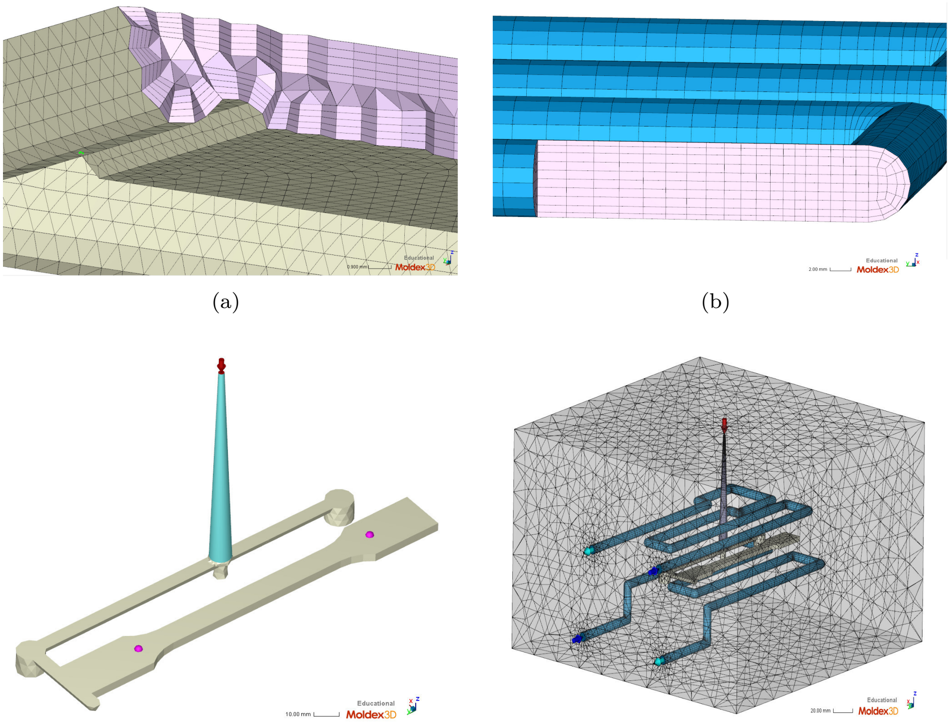

(a) (b)

(c) (d)

Figure 2.12: Mesh details: Tensile specimen (a), Cooling channel (b), Sensors node (c), Mold base (d).

specimen and the cold runner were discretized using a solid BLM (Boundary Layer Mesh) mesh [75, 76], by setting 5 layers of prismatic elements have been set on each side of the wall, while the inner part is occupied by tetrahedral elements as shown in Figure 2.12(a). This kind of hybrid mesh describes better some process aspects, such as the shear effect between the melt material and the mold walls. The cooling channels were made in accordance with those on the real mold with a diameter of 8 mm and discretized with a prismatic element mesh as shown in Figure 2.12(b). In addition, virtual sensors (Figure 2.12(c)) [77, 78] were added at the position of the pressure and temperature sensors in order to obtain more detailed information for comparison with the experimental measurements. The mold base is then modelled to more accurately calculate the heat exchange between the molten polymer and the mold steel, in particular the discretization was made by means of tetrahedral elements, as shown in Figure 2.12(d). At the end of the discretization phase, the total number of solid elements (prisms and tetrahedrons) is 921538, while the number of surface elements is 50348.

2.5 Injection/extrusion molding parameters

According to several experimental studies focused on injection molding [70], the injection parameters may affect the process cycle [79]. For this purpose, in order to obtain a stable transformation process for a shape memory polymer, different simulations were carried out by modifying the main molding parameters. The optimum parameters determined are discussed below. In particular, the injection molding process was simulated by using a melt temperature of 240°C and a mold temperature of 25°C. As regards the injection speed, given the variation in the cross-sections traversed by the material within the cavity, a variable injection profile was chosen, in such a way as to achieve a constant melt front flow progress. The injection speed profile respect to the injected volume is reported in Table 2.5 and expressed by the volumetric flow rate in cm^3/s.

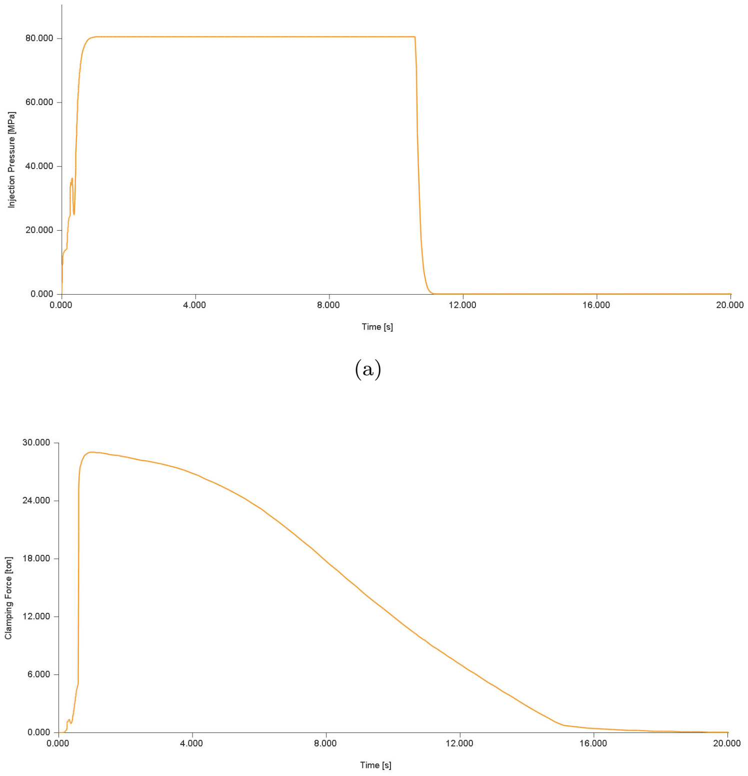

(a)

(b)

Figure 2.13: Injection pressure (a), Clamping force (b).

Melt front flow is an indicator of the melt front movement in different time of the filling phase and provides a very important aspect, as this can determine the aesthetic surface finish of an injection-molded part. The injection pressure curve resulting from the flow rate profile used is reported in Figure 2.13(a). The V/P switch-over has been

Table 2.5: Flow rate profile

Parameter	**Value**			**Unit**
	Fase 3	**Fase 2**	**Fase 1**	
Injection speed	20	35	25	cm^3/s
Injected volume	12	14	22	cm^3

set to 98% of the filled cavity volume, thus obtaining an ideal clamping force profile, as reported in Figure 2.13(b).

Differently, packing pressure and time are the two parameters that characterize the formation of defects in terms of sink marks [80] and high shrinkage [81]. Considering the maximum clamping force as 60 ton and the projected area in the mold-opening direction as 36.34 cm^2, resulting in a maximum cavity pressure possible around 218 MPa. Following all these considerations, the value of the packing pressure that minimize the volumetric shrinkage was at 80 MPa. The packing time is mainly derived from the temperature variation of the melt inside the mold. As the temperature of the melt increases during the filling phase, as the viscosity of the material decreases, enabling to push more material into the cavity during the packing phase. For this reason, to calculate the right packing time, the molten core condition reported in Figure 2.14 was evaluated. Molten core represents an outcome of the simulation that shows the temperature distribution inside the molten plastic, more specifically the enclosed region in the molding plastic that have not solidified. This result can be used to determine the freezing state of the melt around the gate area, which represents the condition when the pressure will not be longer transferred inside the cavity. Observing also, the measured pressure curve in Figure2.15, at the sensor node

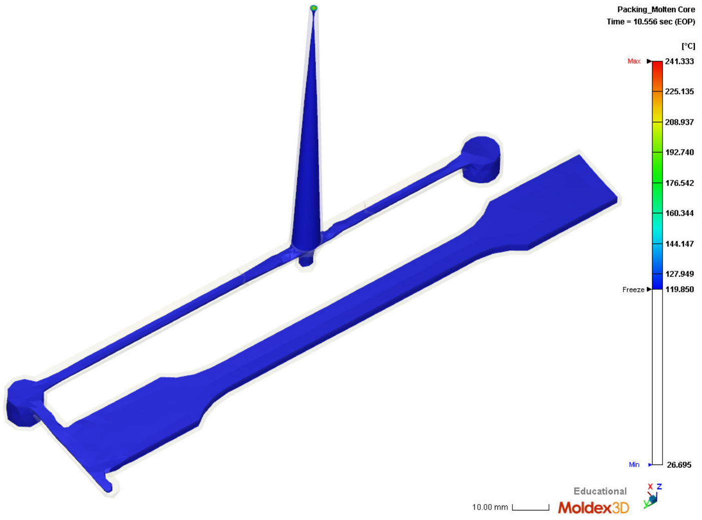

Figure 2.14: Molten core.

position (Figure2.12(c)), is noticeable that at the time instant of 12 s there is a further pressure transfer inside the tensile specimen, although the weight of the part appears to be almost constant.

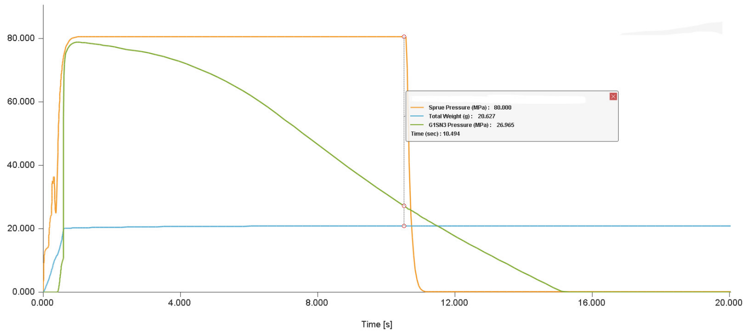

Figure 2.15: Packing time.

Finally, the cooling time was evaluated considering the analysis of the time required, to achieve a well-defined extraction temperature within the whole volume of the cavity. This time is usually influenced by the thickness of the part to be molded, which in this case for the specimen equal to 4 mm, and the imposed ejection temperature. In the simulation the ejection temperature established was 25°C, differently to the ejection temperature condition reported in section 2.4.1. The setting of this temperature will be discussed in section 2.7.2. Figure 2.16 depicts the time required to reach the extraction temperature inside the core of the sample is approximately 72 s. So after a holding time of 12 s, a supplementary 60 s of cooling time are required to perform the ejection phase.

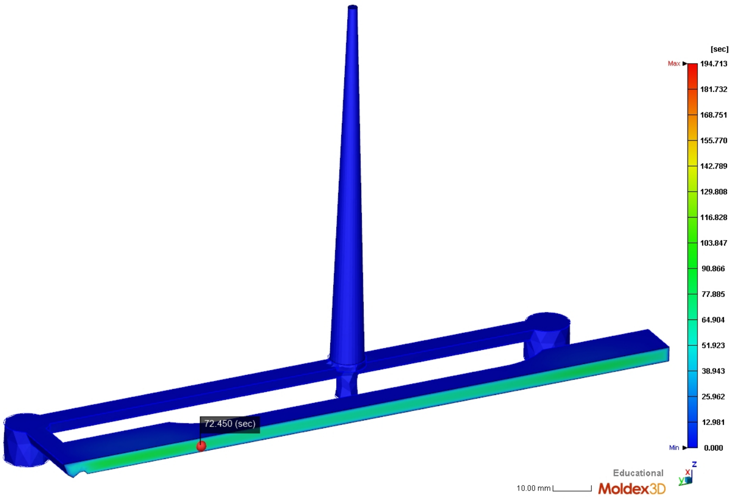

Figure 2.16: Time to reach ejection temperature.

2.6 Injection/extrusion molding parameters on the machine

The parameters retrieved in the previous section, by the simulations analysis, were subsequently used on the injection molding machine. The imposed barrel temperatures and flow rate profile, from the feed section to nozzle, are reported in Table 2.6. Additionally, the main parameters as holding pressure and time, screw back pressure, mold temperature and cooling time are reported.

Table 2.6: Injection molding parameters

Parameter	**Value**			**Unit**
	Nozzel	**Transition section**	**Feed section**	
Melt temperature	240	230 to 220	200 to 190	°C
	Fase 3	**Fase 2**	**Fase 1**	
Injection speed	20	35	25	$\mathrm{cm}^3\ \mathrm{s}^{-1}$
Ram position	12	14	22	cm^3
Holding pressure		800		bar
Holding time		12		s
Screw back pressure		6		MPa
Mold temperature		25		°C
Cooling time		60		s

Before molding, the grains was previously dried at a temperature of 70°C for 12 hours, reaching an optimal condition to remove the overall moisture content.

2.7 Comparison of the injection molding process and simulation

The process stability and reliability were assessed through the analysis of cavity pressure and mold temperature, since they are the prevalent factors influencing the quality aspects of the produced specimen. In order to compare the experimental and simulated data, the in-cavity conditions were monitored for the overall cycle time, by pressure and temperature sensors.

2.7.1 Pressure measurement comparison

The pressure curve recorded by the sensor inside the cavity is shown in Figure 2.17(a). Otherwise, the pressure graph extrapolated from the simulation is depicted in Figure2.17(b). Focusing on the pressure trend, after the switchover, a sudden drop has observed during the holding step, which is typical of amorphous materials, as described in the section 1.5.2.

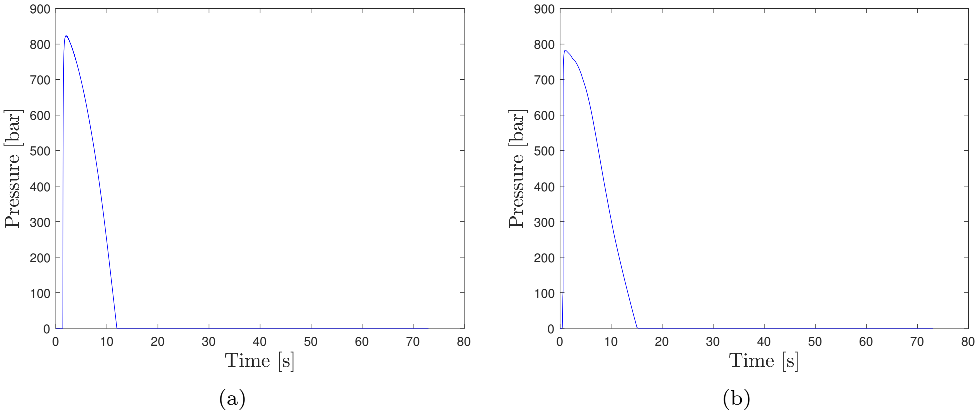

(a) (b)

Figure 2.17: Measured pressure curves cavity (a), simulation (b).

Comparing the curves obtained, the relevant aspect is represented by the freezing point of the gate. In fact, once the maximum pressure peak has been reached, the freezing point in the graph obtained from the simulation is later than that obtained by the sensors in the mold cavity. This effect could be traced back to a localized freezing in the area of the pressure sensor, thus recording a decrease in the pressure recorded in the holding phase.

The pressure profile was controlled for each injection cycle in order to provide the same level of compaction for all specimens.

2.7.2 Temperature measurement comparison

The temperature curve recorded by the sensor inside the cavity and the temperature curve extrapolated from the simulation are depicted in Figure 2.17(a) and

Figure2.17(b).

A comparison of the curves shows that once the maximum temperature peak has been reached, the speed of decrease obtained by the virtual sensor in the simulation is much faster than the real one. This effect is due to the effect that the temperature sensor, in addition to being influenced by the temperature of the mold that surrounds it, is also placed inside the sample, thus recording a temperature variation that is not exactly that of the surface.

Moreover, from the analysis of Figure 2.18, the cavity temperature increases quickly as the melt flows over the sensor, whereas requires a long time to reach the initial value. For this reason, the cooling time of the cycle was set to provide a uniform temperature of the molded part, to ensure that the entire melt reached a temperature below the shape transition temperature (obtained by a following section 3.3.2). The combination of mold temperature and cooling time allowed to easily eject the sample from the mold, without inducing undesired deformations.

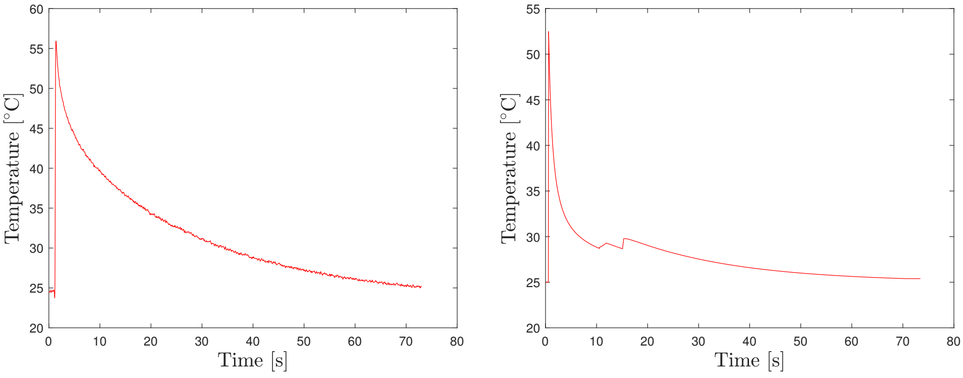

(a) (b)

Figure 2.18: Measured temperature curves cavity (a), simulation (b).

Chapter 3

Mechanical properties

3.1 Mechanical Tests

3.1.1 Quasi-static tensile specimen

Test specimens were prepared in the dog bone shape according to ISO 527-2 for tensile testing of plastics. The Figure 3.1 shows a drawing of the test specimen and related dimensions (Table 3.1) accordance with ISO standard.

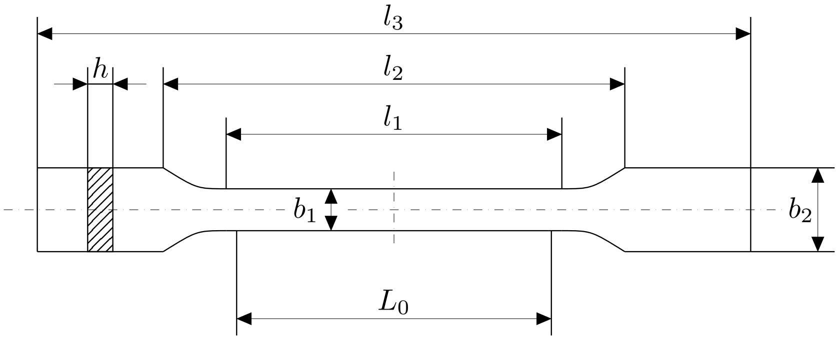

Figure 3.1: Drawing of tensile specimen (following ISO 527-2).

Table 3.1: Dimensions of test specimens

	Specimen type	Value	Unit
l_3	Overall length	170	mm
l_2	Distance between broad parallel-sided portion	109.3 ± 3.2	mm
l_1	Length of narrow parallel-sided portion	80 ± 2	mm
b_2	Width at ends	20.0 ± 0.2	mm
b_1	Width at narrow portion	10.0 ± 0.2	mm
L_0	Gauge length	75.0 ± 0.5	mm
h	Thickness	4.0 ± 0.2	mm

The specimens were obtained with the mold and the injection molding parameters described in the previous chapter 2.

3.1.2 Quasi-static biaxial specimen

The material used to realize the specimen was a SMPU, supplied by MAIP GROUP® in a 0.4 mm thickness laminated foil. In particular, the test specimens were cut by means of a punching machine. The Figure 3.1 shows a drawing of the test specimen and related dimensions (Table 3.1).

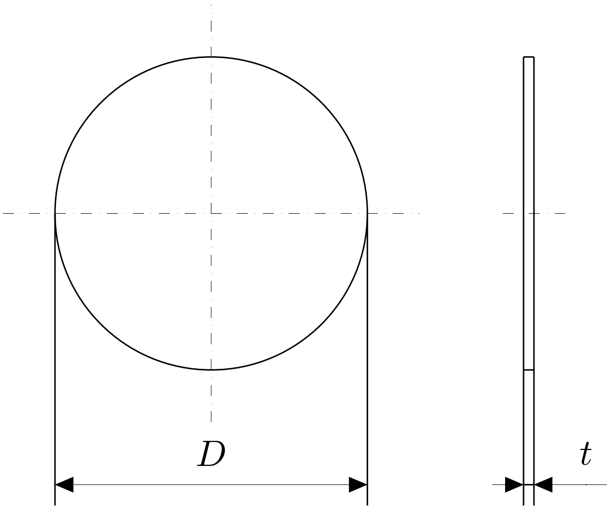

Figure 3.2: Drawing of bulge test specimen.

Table 3.2: Dimensions of biaxial specimens

Specimen type		Value	Unit
D	Diameter	140 ± 3	mm
t	Thickness	0.4 ± 0.02	mm

3.1.3 Measurement of the deformation

Techniques based on the Digital Image Correlation (DIC) are increasingly used as methods for the experimental measurement of full-field deformation [82]. This technique provides non-contact deformation field measurements, by using cameras. During the tests performed, the whole deformation history of specimens was recorded employing two Pixelink® BU371F cameras (1280×1024 pixel^2 8-bit sensor). In general, displacement fields are determined throw each central point of a virtual grid formed from subsets, by comparing the reference image (before deformation) and the deformed images as shown in Figure 3.3. Subsequently, the deformation field can be obtained by deriving the displacement field [83]. In order to correlate the images, contrast patterns are applied to the surface of the test specimen or the part to be measured. In

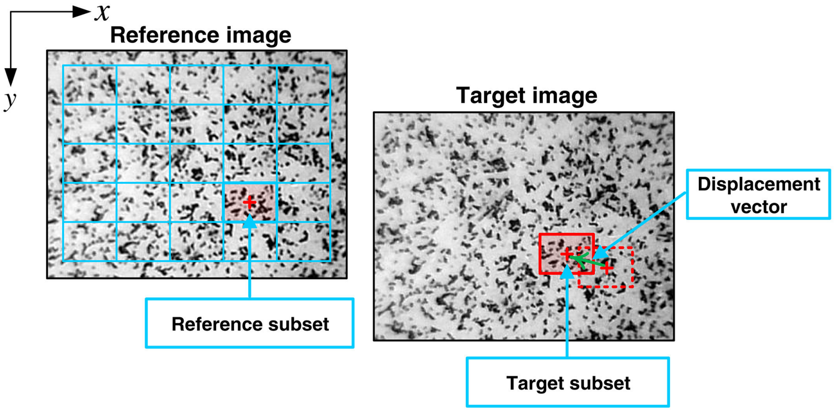

Figure 3.3: Schematic illustration of the undeformed subset and the corresponding deformed subset. Reproduced from [12].

particular, a speckle pattern is applied, consisting of a random distribution of points. Here, the image analysis has been performed by commercial software MatchID® 2021.

3.1.4 Experimental Setup of mechanical tests

The mechanical behaviour of SMPU has been investigated by means of uniaxial tensile tests and the programming sequence of thermomechanical cycles. The mechanical tests have been conducted under temperature control, employing a climatic chamber. The

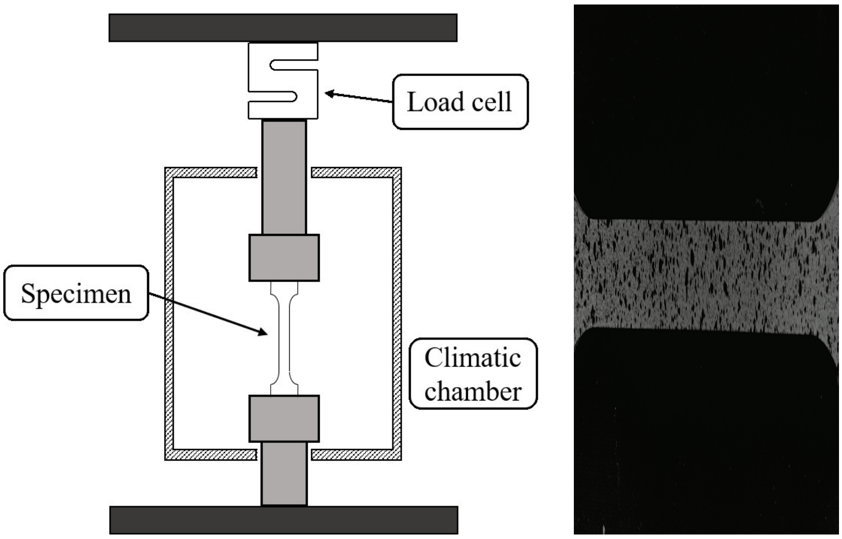

(a) (b)

Figure 3.4: Set up tensile and thermomechanical tests (a) and specimen with speckle pattern (b).

average temperature was monitored and recorded by using 3 K type thermocouples suspended on the specimen. The temperature signals have been acquired through National Instruments SCXI 1000DC acquisition system, equipped with NI 1102C multichannel signal conditioner module. In order to perform quasi-static tensile and thermomechanical tests at different strain and strain rate, a standard electromechanical machine (Zwick/Roell® Z050), equipped with a 500 N load cell with an accuracy of 0.01 N, has been used at different crosshead speed (Figure 3.4(a)). Full strain field was measured using stereo Digital Image Correlation (DIC) technique, in order to accurately determine the Young's modulus and Poisson's ratio. A high contrast random speckle pattern was prepared on the specimens by means of a thin layer of black spray paint on a white background as shown in Figure 3.4(b).

3.1.5 Experimental Setup of biaxial tests

The thermomechanical tests in balanced biaxial stress condition were conducted using a Hydraulic Bulge Test (HBT) machine. In order to activate the shape memory nature of the material, the machine was placed inside a climatic chamber to maintain a constant temperature of the sample. In particular, the temperature inside the climatic chamber was regulated by employing a system of resistors. Furthermore, to ensure a homogeneous heating of the specimen during the experimental tests, also the water used for forming the specimen was maintained at temperature above T_{trans} (i.e., 70°C), while the fluid pressure was measured with a pressure transducer with an accuracy of 0.01 bar. Mean temperature was monitored and recorded, by using 3 K-type thermocouples suspended on the specimen. The temperature signals were acquired through National Instruments SCXI 1000DC acquisition system, equipped with Ni 1102C multichannel signal conditioner module. A schematic view of the set-up is reported in Figure 3.5. As with the uniaxial tests, biaxial tests full strain field was

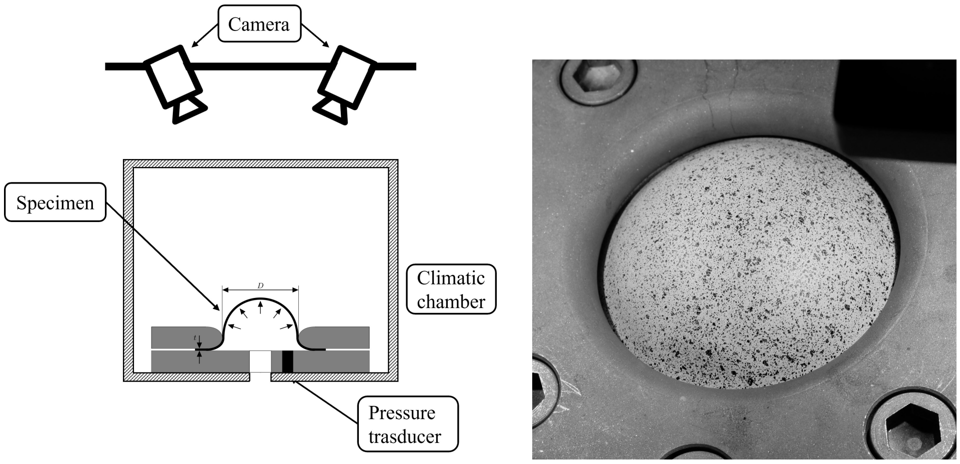

(a) (b)

Figure 3.5: Set up biaxial tests (a) and biaxial specimen with speckle pattern (b).

measured by stereo Digital Image Correlation (DIC) technique, in order to accurately determine strain and curvature of the radius. A high contrast random speckle pattern was prepared on the specimens by means of a thin layer of black spray paint on a white background as shown in Figure 3.5(b).

3.2 Chemical and physical properties

3.2.1 Differential Scanning Calorimetry

In order to investigate the SME behaviour, DSC analysis testing has been used to make the thermal characterization of the SMPU under study. For determining the material transition temperature heat flow of the samples as a function of temperature, in the range from 0°C to 240°C, as reported in ASTM D 3418 standard [84]. The DSC analyses presented in this work were carried out by means of a Seiko® EXSTAR6000 calorimeter. A sample of ∼10 mg was cut from the dog-bone specimens obtained by injection molding, were placed in aluminium crucibles (ϕ 5 mm, height 2 mm), which were inserted in heat cell together with an identical empty crucible, used as reference. Each temperature scanning was conducted by using a scan rate of 20°C min^{-1}, under a dry nitrogen flux having a flow rate of 50 mL min^{-1} during the whole measurement session. The test were repeated at least three times and the most representative results were reported in the present work.

3.3 Uniaxial characterization

3.3.1 Literature review

In the literature, the thermal characterization of SMPs, used to study the thermal properties including the crystallinity, phase transitions and glass transition behaviour, are investigated throw techniques such as DMA and DSC [85, 86, 87].

The static mechanical properties of SMPs has been mainly evaluated by conventional uniaxial tensile [88] and compression [89] tests, for investigating how the temperature affects the mechanical properties [90]. Another interesting aspect, largely studied, is the influence of strain rate on Young's modulus and Poisson's ratio [91]. As such, both the uniaxial tensile and compression tests provide the main mechanical properties related to the analysed material.

Although widely exploited for many type of materials, the SMPs require a specific thermomechanical cycle to quantitatively assess the capability to change and recovery the original shape from the temporary one [92, 93]. This experimental cycle provides two important measurements that characterize the SME strictly related to the deformation applied in the programming sequence, employed in different works [94, 95]. In details, the shape Fixity ratio and the shape Recovery ratio: the former estimates the ability to maintain a temporary shape, while the latter evaluates the capability to restore the original shape [14, 15]. Both Fixity and Recovery ratios characterize the SME of the examined polymer. It is important to observe that the value of these parameters is strongly affected by several factors in literature already investigated. Such as the influence of the prescribed strain on the thermomechanical cycle studied by Bilim et al. (2008) [96]. Yang et al. (2006) [97], investigated the effects of moisture thermomechanical properties on SMPs, due to the significantly decreasing of the glass transition temperature after immersion in water. Differently, Castro et al. (2011) [98] has investigated the amount of the recoverable strain and the recovery rate of an epoxy-based SMP under different thermal conditions.

Regarding the SME fatigue, Lendlein and Kelch (2002) [99] defined a "total strain recovery" parameter for multiple cycle, which removes the dependence on the previous cycle performance. This recovery definition uses the original pre-deformed configuration as the reference value for all thermomechanical cycles to which the material is subjected, and therefore provides a measure of the performance of the material in reference to its original state. For this reason, this parameter results completely different from the once defined by Tobushi (1996) [55], in which it does not involve decay of the recovery behaviour of the material with the increasing number of cycles.

This parameter has been adopted by many researchers, Schmidt et al. (2008) [100] examined functional fatigue of the SME of Veriflex and found that the styrene-based resin exhibited recovery values between 65 and 85% with a large decay from the first cycle to the eighteenth. The decay of the prescribed deformation recovery, demonstrates that the recovery behaviour of the material continues to decrease as the number of cycles is increased [101].

3.3.2 Glass Transition Temperature Pellet material

Figure 3.6 depicts the normalized heat flow versus temperature, in the range from 0°C to 240°C. Given the absence of other thermal events going towards the upper scan limit, in Figure 3.7 the normalized heat flow versus temperature, in the temperature range 0-80°C is reported. Only the glass transition temperature (T_g) has been observed by means of DSC analysis. The determination of the glass transition region has been obtained drawing two lines that ideally continue the baseline before and after the transition and the line corresponding to the inflection point of the curve, between the two baselines. The intersection of these lines allow the definition of the temperature range, corresponding to the start and the end of the glass transition. In particular,

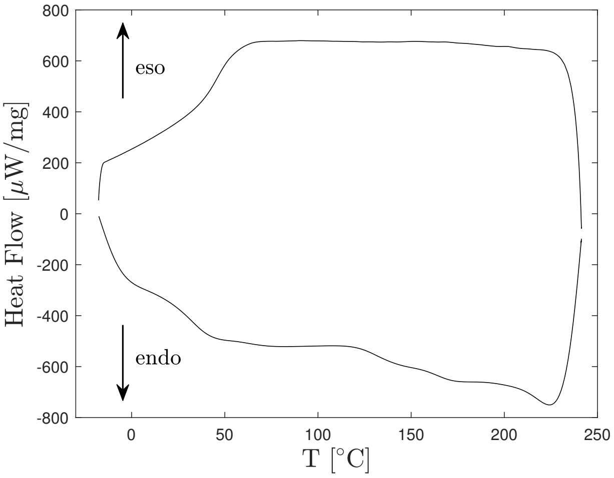

Figure 3.6: Total DSC result of SMPU pellet material.

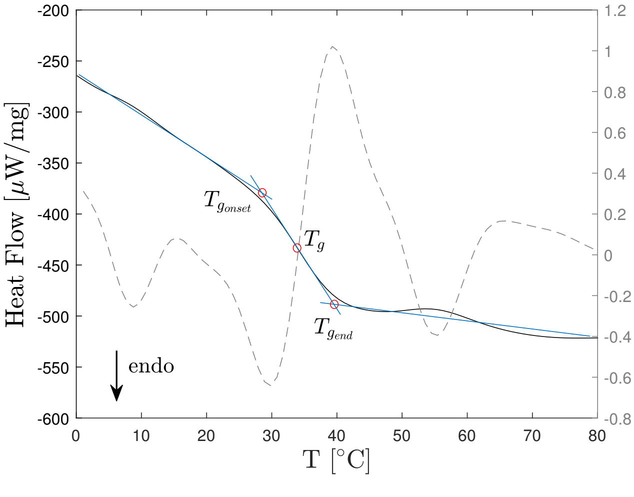

Figure 3.7: DSC result of SMPU pellet material, where the dashed line represent the second derivative of the heat flow.

the temperature at the transition start is represented by the onset temperature $T_{g_{onset}}$ equal to 30.1°C and similarly the transition $T_{g_{end}}$ equal to 39.8°C. The glass transition temperature, T_g, of the SMPU was determined conventionally as the temperature corresponding to the inflection point, equivalent to 34.1°C [102]. For an accurate determination of this value, it has been obtained by the maximum of the numeric second derivative of curve reported as dashed line in Figure 3.7. Given this result, the thermomechanical cycles were carried out at T_h temperature of 50, 60 and 70°C.

The region between $T_{g_{onset}}$ and $T_{g_{end}}$ is named Glass Transition region, whereas, the region under $T_{g_{onset}}$ is named Glassy region and the region over $T_{g_{end}}$ is named Rubbery region. At $T < T_g$, both soft and hard chain segments are frozen and the material is stiff and difficult to deform. On the contrary, when $T > T_g$, the soft segment are free to move and the material results flexible and easy to deform. The difference of the mechanical properties of SMPU in these different regions will be discussed in the following section.

3.3.3 Uniaxial tensile tests of Pellet material

With the purpose to investigate the dependence of mechanical behaviour of the SMPU on temperature, several tensile tests under uniaxial stress state have been carried out. The tensile tests have been performed on different dog-bone specimens manufactured by injection molding process, as previously described in chapter 2. The samples have been tested at different temperatures, in the range 20÷70°C, at constant strain rate of 10^{-4} s^{-1}.

Uniaxial tensile tests in Glassy Region

Initially the specimens were tested at temperature of 20 and 25°C as shown in Figure 3.8. At these temperatures, the material is in a region called Glassy. Below the T_g the

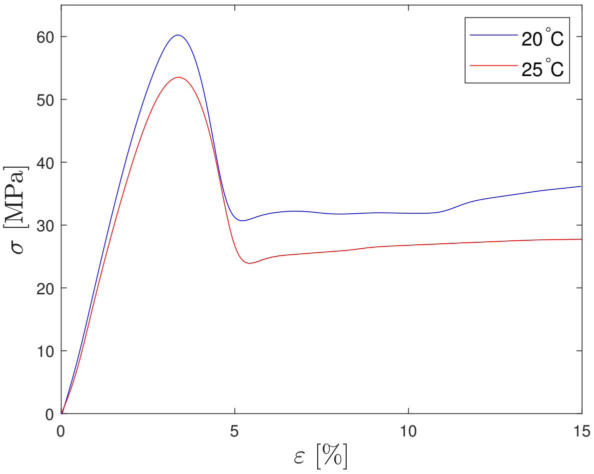

Figure 3.8: Tensile curves in glassy region.

material has high stiffness and exhibits a behaviour characterized by a small linear elastic phase reaching a distinct upper yield, followed by an apparent plateau in plastic regime. The plateau, similar to the well-known Luder band phenomenon, is followed by necking formation and propagation on the specimen, as can be observed in Figure 3.9 for the specimens tested at 25 and 32°C. The hardening is a result of the reorientation of polyurethane SMP molecular chains, which induces crystallization. The elongation limit of this material is over 200% (Figure 3.10) in terms of the engineering strain, and increases with the decrease of the strain rate. Furthermore, the yield strength increases with the increase of the strain rate, while the ultimate strength is opposite.

Figure 3.9: Specimens tested in glassy region.

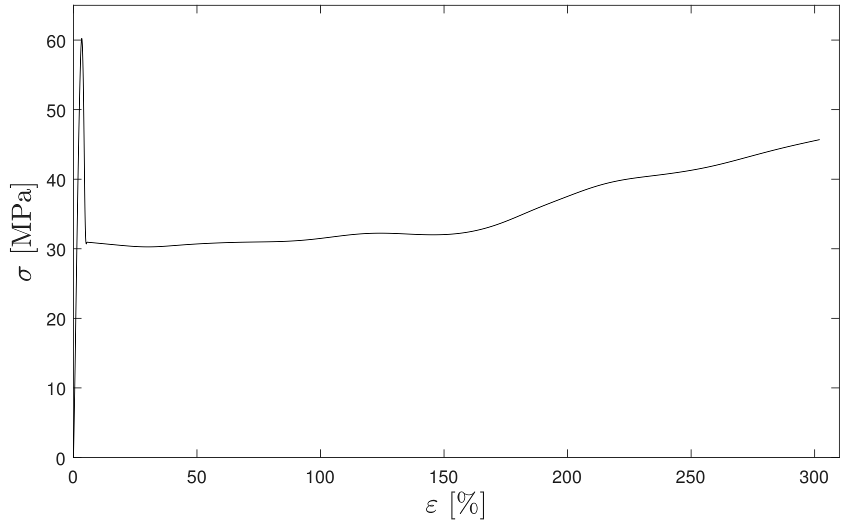

Figure 3.10: Tensile curves in glassy region.

Uniaxial tensile tests in Glass transition Region

Moreover, uniaxial tensile tests were conducted in the interval called Glass Transition Region as shown in Figure 3.11. In this temperature range of 30 to 37°C, can be observed how the mechanical behaviour of the material changes. Is possible to notice that up to 33°C behaviour similar to that observed in the Glassy Region, i.e., with the presence of an upper yield which decreases sharply with increasing temperature, followed by a plateau in plastic regime. Noticeable, in Figure 3.12 among the specimens tested at 33 and 34°C, the disappearance of localized necking, while results clearly visible at 32°C.

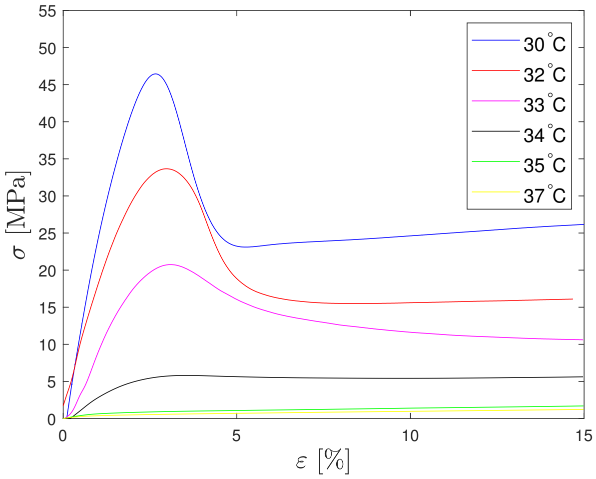

Figure 3.11: Tensile curves in glass transition region.

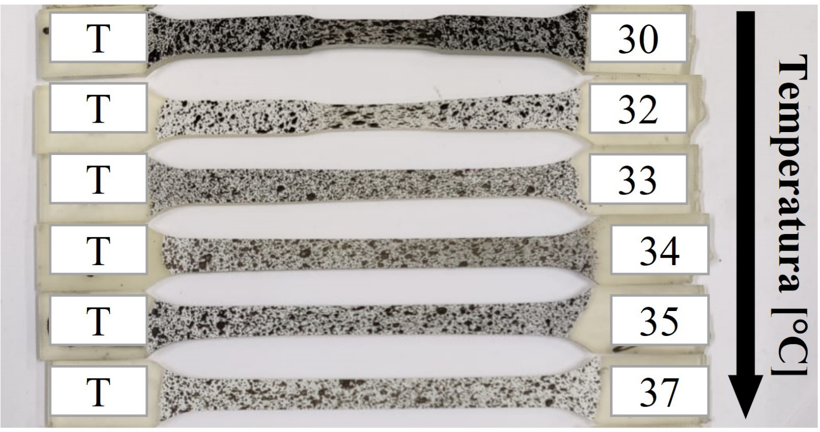

Figure 3.12: Specimens tested in glass transition region.

Uniaxial tensile tests in Rubbery Region

Uniaxial tensile tests were carried out also at temperature $T_g + 6°C$, where the SMPU is in the Rubbery region. The stress-strain curves obtained at different temperature are reported in Figure 3.13. Conversely, at temperatures over the T_g the obtained responses reveals the typical viscoelastic properties, similar to an elastomer, where the elongation increases continuously with little variation of the applied force and necking has not been observed, as shown in Figure 3.14 for the specimens tested at temperature over 37°C. Along the transition region the material shows a strong alteration of the mechanical behaviour of the SMPU, both in terms of Young modulus and Poisson's ratio, in a limited range of temperature variation.

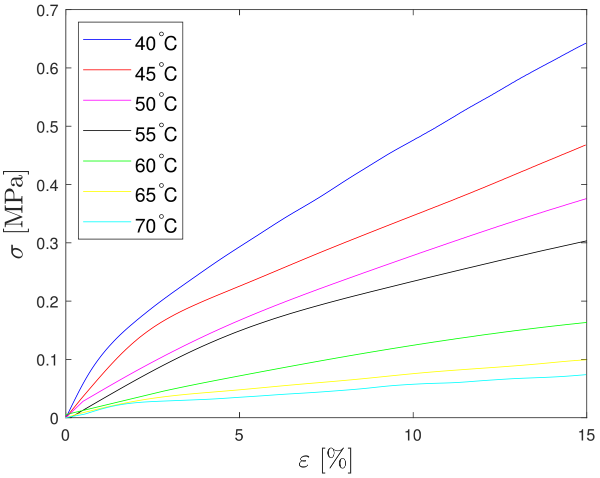

Figure 3.13: Tensile curves in rubbery region.

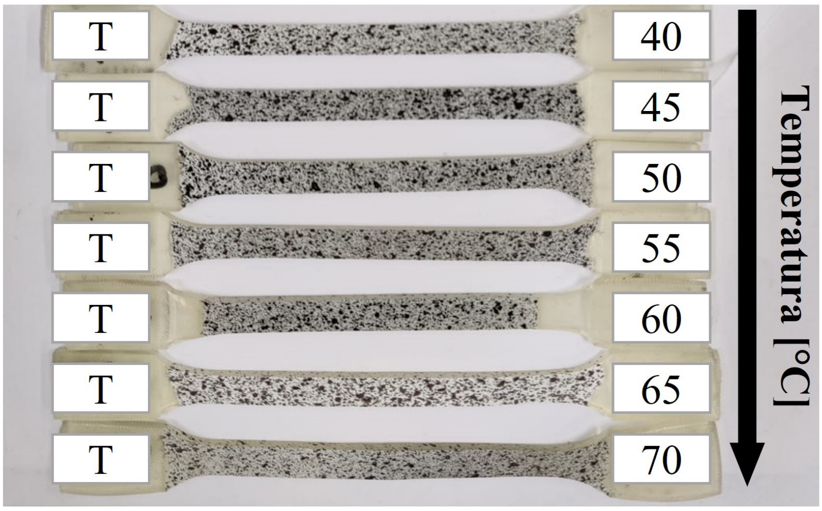

Figure 3.14: Specimens tested in rubbery region.

3.3.4 Effect of temperature on Young's modulus and Poisson's ratio

The Young's modulus (E) and Poisson's ratio (ν) have been determined by analysing the measured strains with the DIC technique in terms of Hencky strain; their dependence with test temperature is shown in Figure 3.15, from which it can be noted that strong decrease of the material stiffness and increase of Poisson's ratio occurs with increasing temperature [103].

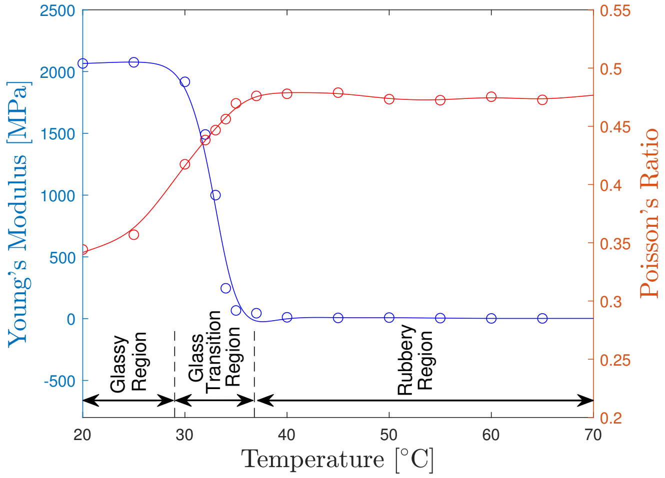

Figure 3.15: Temperature dependence on polymer stiffness and Poisson ratio.

The results in Figure 3.15 can be grouped into three different regions, in which the material exhibits a unique and characteristic mechanical behaviour: Glassy, Glass Transition and Rubbery.

Below the T_g the material has high stiffness and exhibits a behaviour characterized by a small linear elastic phase reaching a distinct upper yield, followed by an apparent plateau in plastic regime. The plateau is followed by necking formation and propagation on the specimen, as shown in Figure 3.12 for the specimens tested at 25 and 32°C.

Conversely, at temperatures over the T_g the material behaves differently, similar to an elastomer, where the elongation increases continuously with little variation of the applied force and necking has not been observed, as shown in Figure 3.12 and Figure 3.14 for the specimens tested at 34 and 35°C and over.

Along the Glass Transition region the material shows a strong alteration of the mechanical behaviour of the SMPU, both in terms of Young's modulus and Poisson's ratio, in a limited range of temperature variation.

3.3.5 Thermomechanical characterization at different temperature, strain and strain rate

In this section, in order to determine the influence of strain, strain rate and temperature on the Fixity and Recovery ratios, thermomechanical tests were carried out according to the cycle reported in Figure 1.13. More specifically, as shown in section 3.3.2, after the determination of the glass transition temperature by means of DSC, the thermomechanical cycles were carried out at three T_h values higher than T_{trans}. Furthermore, the thermomechanical tests were conducted up to three different values of prescribed engineering strain, i.e., 25, 50, and 80%. In order to submit the specimen to different strain rates in the loading step (10^{-3}, 10^{-2} and 10^{-1} s^{-1}), tests have been performed at different crosshead speed. The tests were conducted in displacement-control for the first two steps and in force-control for the last two. Differently, the unloading step was performed at a low strain rate, 10^{-4} s^{-1} in all tests. In the climatic chamber, the heating and cooling rates have been set at 5°C min^{-1}.

The results of all thermomechanical cycles conducted are reported in Appendix. For sake of brevity, just one results of thermomechanical cycle obtained is reported in Figure 3.16, here referred to T_h of 50°C ε_p of 25%.

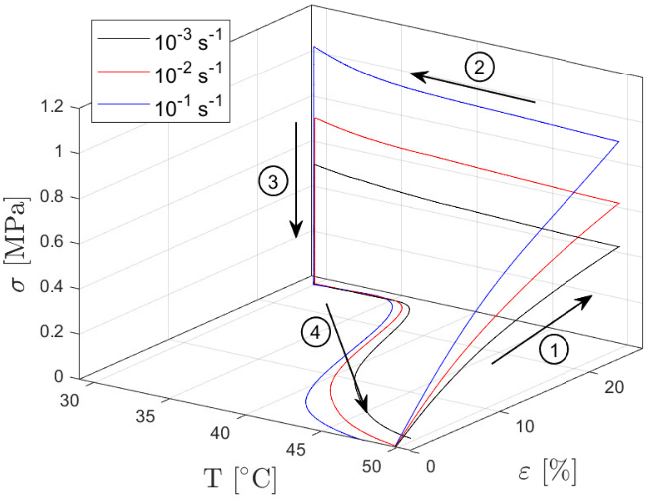

Figure 3.16: Thermomechanical cycle at 50°C and 25% prescribed deformation.

With the purpose of examining the effects of temperature, strain and strain rate, each step of the cycle has been investigated separately.

In the *Loading step* ① the specimen is deformed at the temperature above T_g up to the prescribed value of deformation. Figure 3.17(a) shows the thermomechanical cycle in the stress-strain plane, at three different strain rates (i.e. 10^{-1}, 10^{-2} and 10^{-3} s^{-1}). The curves show the typical rubbery behaviour; in addition a clear strain rate sensitivity is visible. Reporting the maximum stress (σ_p) achieved at 25% of

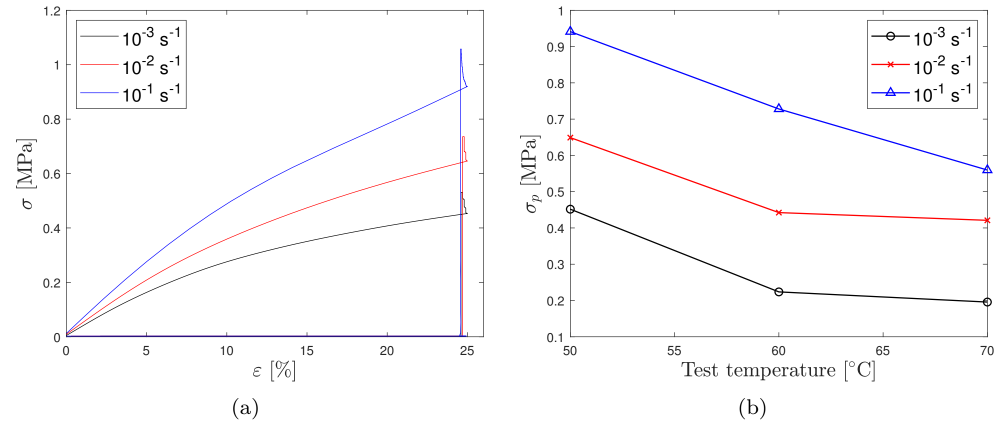

Figure 3.17: Stress vs strain during *Loading step* at 25% prescribed strain (a) and stress achieved at 25% of strain (b).

deformation (Figure 3.17(b) over different temperatures, it can be observed that the material becomes softer while increasing the temperature, whereas is stronger while increasing the strain rate [91].

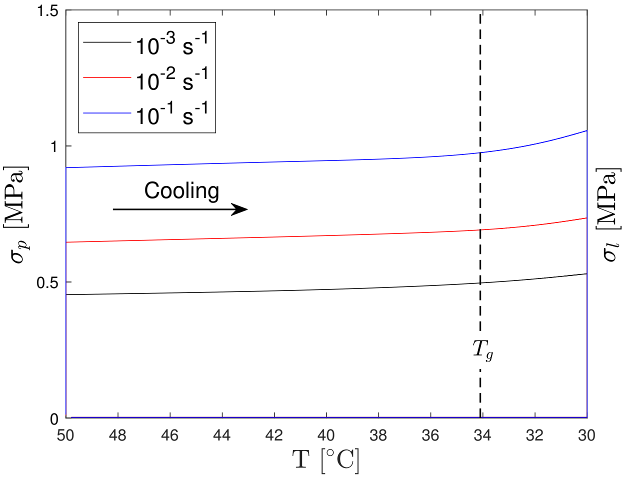

Figure 3.18: Strain vs temperature during *Cooling step* at 25% prescribed strain.

Once the established ε_p is reached, the *Cooling step* ② (Figure 3.16) starts while the sample is kept at the constant strain. In this step, a stress increment has observed from σ_p to σ_l, due to the combination of thermal effects and the applied constraint. In fact, the increase of stress is induced by the thermal contraction and the increment of Young's modulus, while temperature crosses the glass transition region [96]. According to this, Figure 3.18 it is noted that the stress increases more significantly when the material is cooled below the T_g.

The material is then cooled down to the T_l temperature, here referenced as room temperature. Hence, the *Unloading step* ③ (Figure 3.16) begins, in which the specimen is in its glassy state and brought to a zero-stress condition. This unload slightly impacts on the prescribed strain ε_p, reaching a stored strain ε_u at the end of this step. After the *Unloading step* of the thermomechanical cycle, the Fixity ratios have been computed according to Equation 1.1. As reported in Table 3.3, 3.4, 3.5, the SMPU reached high values of Fixity ratio, close to 100%. These results underline that the tested SMPU has an excellent ability to maintain the imposed temporary shape.

Table 3.3: Fixity Ratio R_f at 50°C

Strain rate [s^{-1}]	**Prescribed strain** ε_p [%]		
	25	**50**	**80**
10^{-3}	99.45	99.76	99.81
10^{-2}	99.63	99.90	99.83
10^{-1}	99.46	99.16	99.88

Table 3.4: Fixity Ratio R_f at 60°C

Strain rate [s^{-1}]	**Prescribed strain** ε_p [%]		
	25	**50**	**80**
10^{-3}	99.89	99.98	99.93
10^{-2}	99.85	99.92	99.86
10^{-1}	99.87	99.93	99.91

Table 3.5: Fixity Ratio R_f at 70°C

Strain rate [s^{-1}]	**Prescribed strain** ε_p [%]		
	25	**50**	**80**
10^{-3}	99.88	99.86	99.89
10^{-2}	99.91	99.90	99.90
10^{-1}	99.60	99.67	99.78

In the last part of thermomechanical cycle, the *Reheating step* ④ (Figure 3.16), the specimen remains unloaded while the stored strain is gradually recovered. The strain recovery of the material is shown in Figure 3.19, where the strain-temperature curves for the three different strain rates are displayed. In particular, by increasing the temperature, the strain remains constant until the glass transition region is reached; at this point the material stiffness starts to decrease and strain recovery begins. Here, most of the strain is recovered, compared to what occurs in the rubbery state. More specifically, by observing the curves it is possible to notice an inflection point, in the glass transition temperature region. This step ends when the material arrives to the loading temperature T_h and an irrecoverable deformation ε_{ir} is observed. According to Equation 1.2, the value of the Recovery ratios have been determined from the all performed thermomechanical test and reported in Table 3.6, 3.7, 3.8.

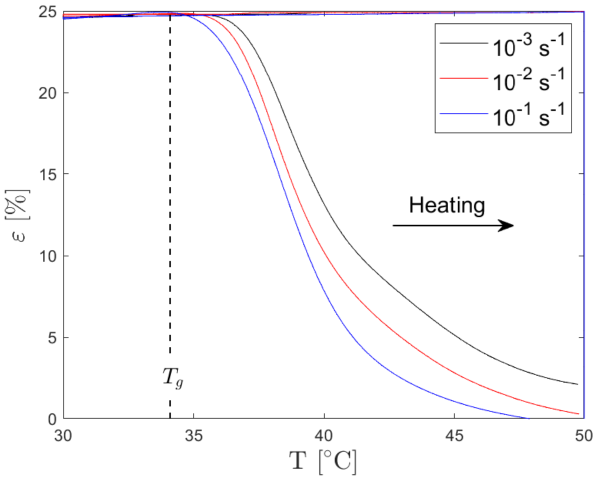

Figure 3.19: Strain vs temperature during *Reheating step* at 25% prescribed strain.

Table 3.6: Recovery Ratio R_r at 50°C

Strain rate [s^{-1}]	**Prescribed strain** ε_p [%]		
	25	**50**	**80**
10^{-3}	91.00	89.49	82.24
10^{-2}	98.69	93.03	92.88
10^{-1}	99.24	94.54	93.98

Table 3.7: Recovery Ratio R_r at 60°C

Strain rate [s^{-1}]	**Prescribed strain** ε_p [%]		
	25	**50**	**80**
10^{-3}	81.13	67.61	63.07
10^{-2}	95.78	87.55	81.70
10^{-1}	97.17	94.54	90.53

Table 3.8: Recovery Ratio R_r at 70°C

Strain rate [s^{-1}]	**Prescribed strain** ε_p [%]		
	25	**50**	**80**
10^{-3}	77.25	64.11	56.95
10^{-2}	94.02	87.43	80.85
10^{-1}	96.04	91.87	89.77

The dependence of Recovery ratio from strain, strain rate and temperature is discussed in next section.

3.3.6 Main effect analysis

Influence of Strain Rate

In order to carry out a sensitivity analysis on the variation of the Fixity and Recovery ratio, the values of R_f and R_r vs prescribed strain ε_p are shown in Figure 3.20 and Figure 3.21; in each Figure (a), (b) and (c) refer to strain rates of 10^{-1}, 10^{-2} and 10^{-3} s^{-1} respectively.

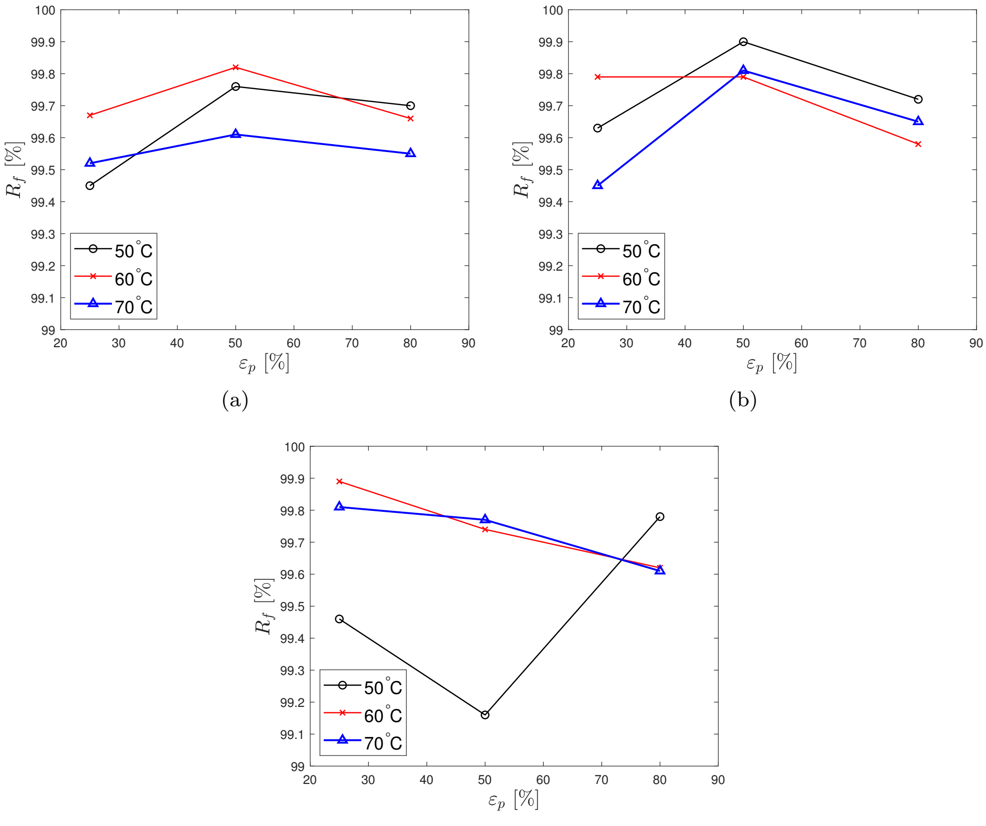

(a)

(b)

(c)

Figure 3.20: Dependence of Fixity ratios R_f on prescribed strain ε_p at 10^{-3} s^{-1} (a), 10^{-2} s^{-1} (b) and 10^{-1} s^{-1} (c).

In the previous section, it was found that the Fixity ratio is nearly 100% for all tested conditions (Table 3.3, Table 3.4 and Table 3.5). As depicted in Figure 3.20, it is clearly visible that the Fixity ratio is not affected by the test temperature or the strain rate variation.

On the other hand, the Recovery ratio is strongly influenced by thermomechanical cycle parameters. For any given strain rate, it is noticeable that the Recovery ratio decreases as the test temperature increases. In addition, the difference in R_r at different temperatures decreases with increasing strain rate (Figure 3.21(c), compared to Figure 3.21(a) and Figure 3.21(b)), as well as the Recovery ratio increases with

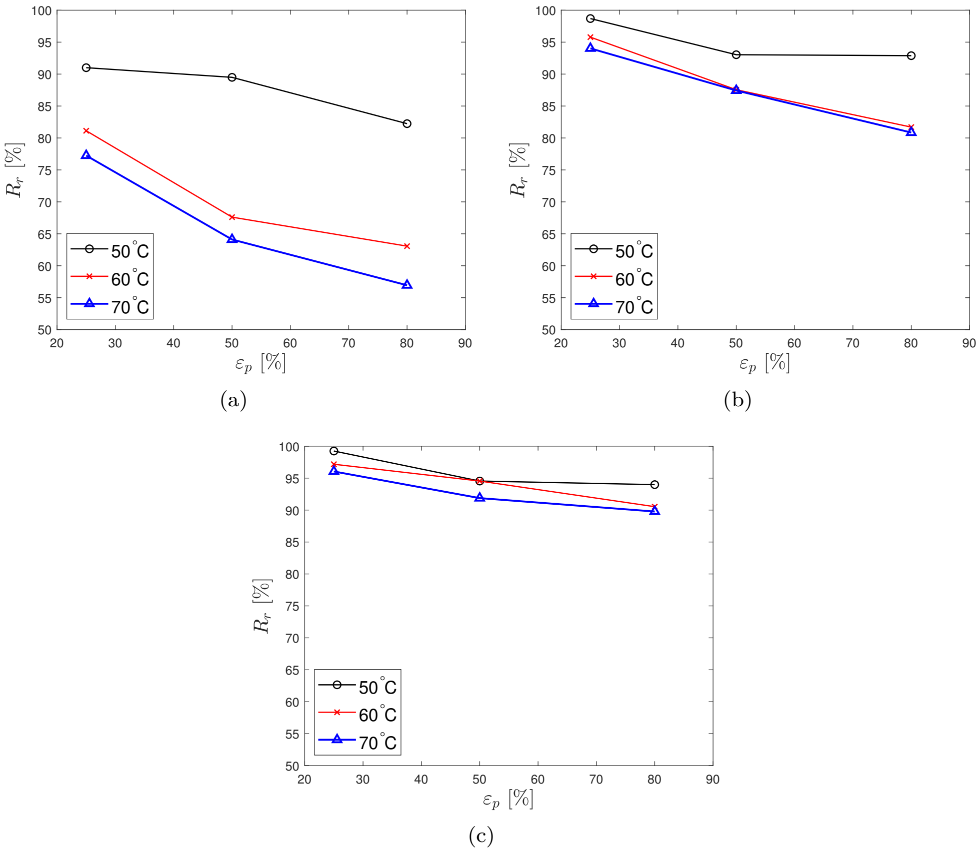

(a)

(b)

(c)

Figure 3.21: Dependence of Recovery ratios R_r on prescribed strain ε_p at 10^{-3} s^{-1} (a), 10^{-2} s^{-1} (b) and 10^{-1} s^{-1} (c).

strain rate. Regarding the tests carried out at 50°C, the Recovery ratio increases more significantly with the strain rate only between 10^{-3} and 10^{-2} s^{-1} (Figure 3.21(a) and Figure 3.21(b), respectively). These findings can be interpreted by considering the entropy related to molecular conformations of the polymer chains in the amorphous regions of the examined material, stimulated by temperature, under and above T_g, and by the prescribed mechanic deformations. In fact, the SME is linked with the variation of molecular entropy state of such chains during the whole thermomechanical cycle. According to the literature mentioned in section 1, the relative arrangement of macromolecules during the cycle is influenced by the imposed conditions, which may or may not facilitate the relative slippage and then their conformation changes in order to regain their stable state characterized by a high entropy at the end of the *Reheating step*. Focusing on Figure 3.21, two extreme conditions can be observed. Firstly, if the thermomechanical cycle is performed at high temperatures in the *Loading step*, the initial molecular conformations state is characterized by a high entropy [104]. This means that the molecular chains are freer to slip and can be more oriented by the prescribed deformation, which will considerably reduce the entropy [105, 106]. The lowering of strain rate further contributes to a significant reduction of entropy in the *Loading step* because more time is available for a high orientation of the macromolecules, during the deformation to a given prescribed strain. Therefore, after reheating, starting from an elevated degree of molecular order, the Recovery ratio is reduced, higher is the initial loading temperature and lower is the stain rate, which is more visible in Figure 3.21(a) compared to the other ones. On the other hand, the opposite condition is characterized by a high entropy, produced at low loading temperature and high strain rates, meaning that the molecular chains are less free to slip and cannot be easily oriented by the deformation. The entropy change due to deformation is therefore lower, even more when the prescribed strain is low and the strain rate increases, which is related to the resistance of macromolecules to deformation increases. As a result, the *Reheating step* of the thermomechanical cycle, which activates the SME, determines a higher SMPU recovery (high R_r) of the original shape, since a smaller amount of entropy variation must be recovered, almost independently of the prescribed strain and the temperature at the highest strain rate (see Figure 3.21(c) compared to the other two).

Main effects

The global influence of the investigated parameters (strain, strain rate and temperature) on the SME of the studied SMPU can be summarized in the "main effect chart" shown in Figure 3.22 and Figure 3.23. In these graphs, the black markers represent the average value of the Fixity and Recovery ratio for a given parameter kept constant while the others are varied in the considered range; the thin bars indicate the minimum-to-maximum range. The dashed lines represent the linear regression relating the investigated parameters and the Fixity and Recovery ratio.

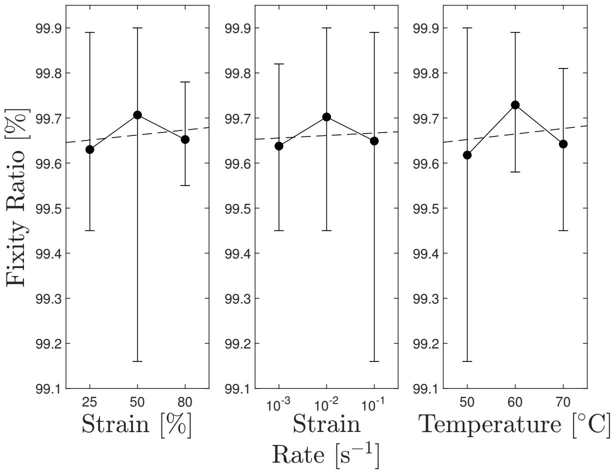

Figure 3.22: Stress vs temperature during *Reheating step* at 25% prescribed strain.

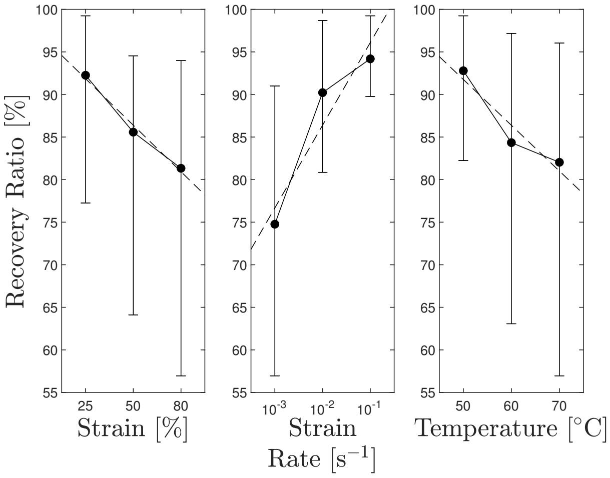

Figure 3.23: Stress vs temperature during *Reheating step* at 25% prescribed strain.

The main effects analysis on the Fixity ratio, as depicted in Figure 3.22, evidence that an increase of the prescribed Strain, Temperature or Strain Rate in the thermomechanical cycle does not have a relevant effect on the capability to maintain the temporary shape.

Differently, the main effects analysis on the Recovery ratio, as can be observed in the Figure 3.23, proves that an increase of the prescribed Strain and the Temperature in the thermomechanical cycle have a negative effect, while Strain rate has a positive effect. The slopes of the regression lines determine that the Recovery ratio decreases by 0.2% for each percentage point of increase in prescribed strain or temperature, while it increases by about 10% as the strain rate increases by one decade. It is worth noting that in the centre graph, in addition to an increase in the mean value of the Recovery ratio, the minimum-to-maximum range decreases as the strain rate increases. This underlines that the effect of strain rate is of paramount importance in the use of SMPUs.

Design chart

Finally, in studying or designing real applications with SMPU, the absolute values of irrecoverable strain can be of interest. In this context, determining the material behaviour, in terms of R_r or ε_{ir}, under specific operating conditions (e.g., strain, strain rate and temperature) is relevant. Hence, the results can be proposed also as parametric curves of the irrecoverable strain ε_{ir} vs prescribed strain ε_p, as shown in Figure 3.24. In this chart, the oblique thin black lines represent the conditions of Recovery ratio from 0% to 100%, namely when the irrecoverable strain is total and null. Since the irrecoverable strain is a fraction of the prescribed one, lines with constant Recovery ratio have been added to simplify the diagrams readability. For each set of strain rate, the value of irrecoverable strain ε_{ir} increases with the prescribed strain ε_p, meaning that the original shape recoverability is reduced. On the other hand, for

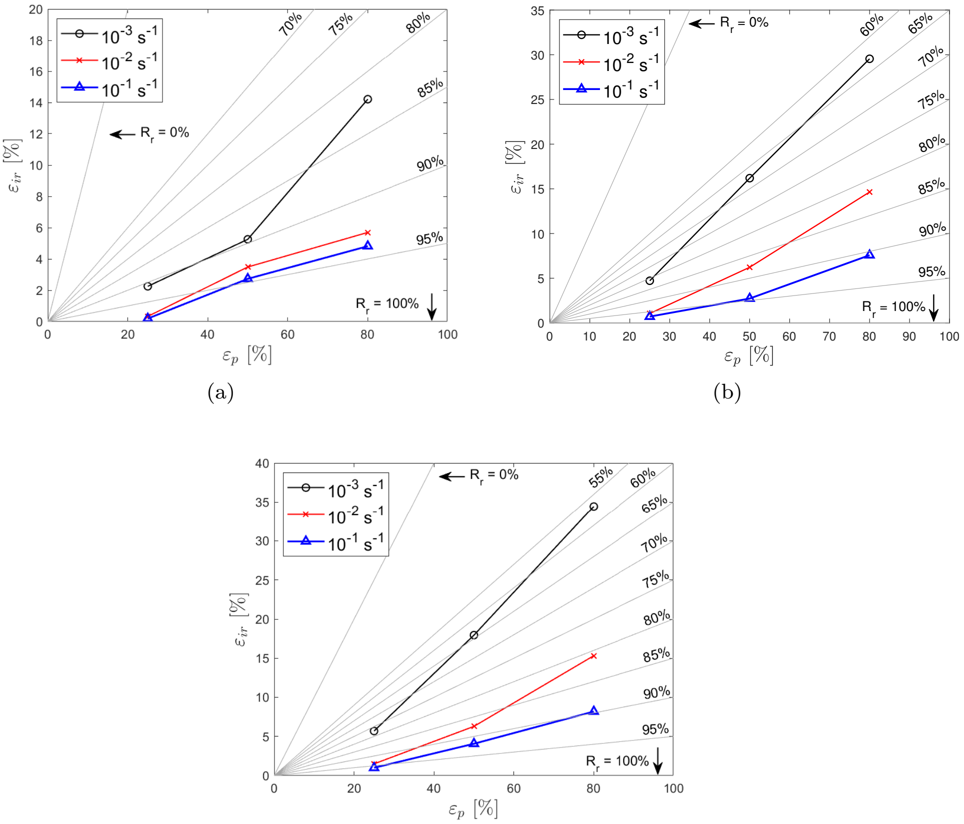

(a)

(b)

(c)

Figure 3.24: Dependence of irrecoverable strain ε_{ir} on prescribed strain ε_p at 50°C (a), 60°C (b) and 70°C (c).

a constant prescribed strain, the value of ε_{ir} decreases with the increase of strain rate. This effect results in a higher Recovery ratios values in the last step of the thermomechanical cycle, namely a greater recovery of the original shape as the strain rate increases in the *Loading step*.

3.3.7 Influence of repeated cycles on the shape memory effect

In order to evaluate the fatigue of the SME of SMPU, the thermomechanical cycles were performed multiple times for each sample. The prescribed strain ε_p was kept constant for each cycle and equal to 25% of the original gauge length and the temperature T_h, was imposed at 50°C. The cycles were performed five times for each specimen and were analysed the SME for two different strain rate, 10^{-3} and 10^{-1} s^{-1} respectively.

In Figure 3.25 a comparison analysis between the total Recovery ratio $R_{r,tot}$ and the Recovery ratio R_r are presented. More specifically, R_r is evaluated according to the Equation 3.1, while $R_{r,tot}$ according to the Equation 3.2.

$$R_r(N) = \frac{\varepsilon_p - \varepsilon_{ir}(N)}{\varepsilon_p - \varepsilon_{ir}(N-1)} \times 100 \tag{3.1}$$

$$R_{r,tot}(N) = \frac{\varepsilon_p - \varepsilon_{ir}(N)}{\varepsilon_p} \times 100 \tag{3.2}$$

The R_r ratio was defined by Tobushi et al. in (1996) [55] to evaluate the performance of the material if it is subjected to several thermomechanical cycles. The equation compare the deformation of the material after recovery in the current cycle (numerator) with the deformation after recovery in the previous cycle (denominator).

Differently, $R_{r,tot}$ was defined by Lendlein and Kelch (2002) [99] as "total strain recovery" parameter for cycle N. This ratio $R_{r,tot}$ in respect to R_r, removes the dependence on the previous cycle performance, always referring to the initial shape.

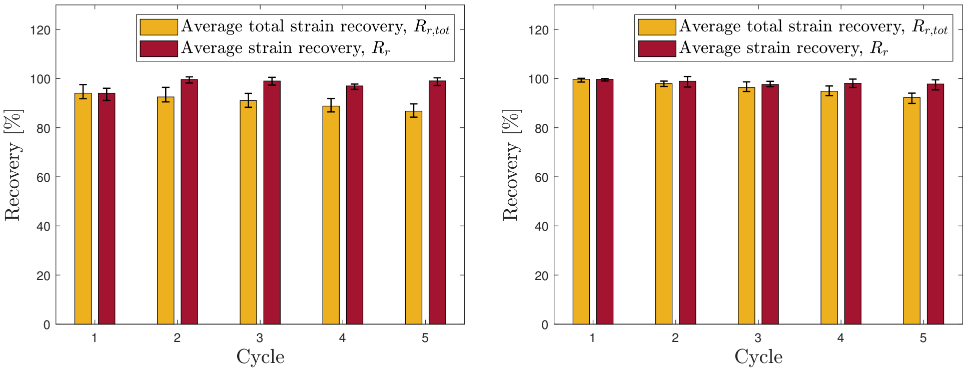

(a)

(b)

Figure 3.25: Recovery ratio and Total recovery ratio comparison at 10^{-3} s^{-1} (a) and 10^{-1} s^{-1} (b).

The figures illustrate how, by taking the R_r for calculating of the recovery, can vary the recovery capability of the material and remain constant as the number of cycles increases (see red bar). In fact, the polymer does not completely recover its original shape, but simply recovers most of the prescribe deformation from the previous cycle. In contrast, by considering for all the cycles performed the recovery capacity ($R_{r,tot}$)

in relation to its original shape, it can be observed that the Recovery ratio decreases as the number of cycles increases.

For this purpose, the following Figure 3.26 and 3.27, shown the average of: Fixity ratio (R_f), Total recovery ratio ($R_{r,tot}$) and maximum stress (σ_{max}) for four specimens. Note that for each bar are reported also the extreme values. In particular, Figure 3.26 shown the value extrapolated for the cycles conducted at 10^{-3} s^{-1} strain rate, while Figure 3.27 shown the value extrapolated for the cycles conducted at 10^{-1} s^{-1} strain rate. Histograms show that the average of the trend of the Fixity ratio remains high for both strain rates, with values of R_f above 98% throughout the cycles (Figure 3.26(a) and Figure 3.27(a)). Otherwise, the Recovery ratio decreases as the number of cycles increases at both the strain rates. More specifically, at 10^{-3} s^{-1} strain rate, the average of R_r begins at 91% and drop to 85% (Figure 3.26(b)). The same decrease occurs for cycles conducted at strain rate 10^{-1} s^{-1}, observing a decrease of the same magnitude, but with a higher average $R_{r,tot}$ going from 99% to 92% by the five cycles (Figure 3.27(b)). By comparing the histograms obtained at 10^{-3} and 10^{-1} s^{-1}, it is possible to observe that the effect of the strain rate continues to occur not only in

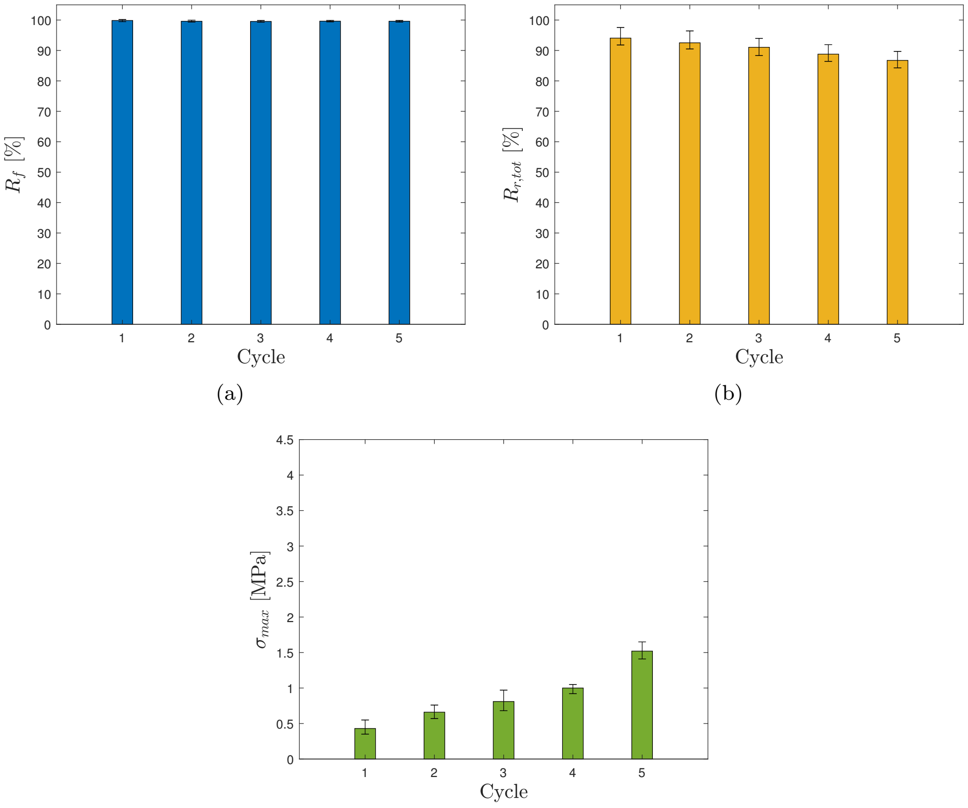

(a)

(b)

(c)

Figure 3.26: Fixity ratio (a), Recovery ratio (b), and Maximum stress (c) for five thermomechanical cycles (Strain rate of 10^{-3} s^{-1}).

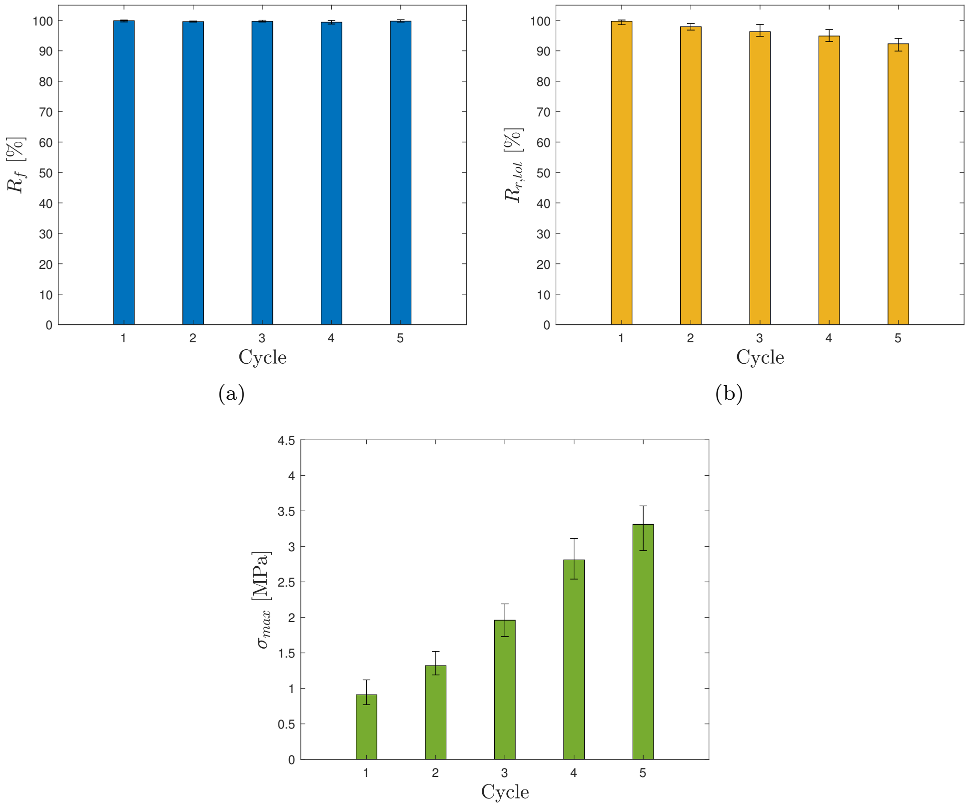

(a)

(b)

(c)

Figure 3.27: Fixity ratio (a), Recovery ratio (b), and Maximum stress (c) for five thermomechanical cycles (Strain rate of $10^{-1}\ s^{-1}$).

the first thermomechanical cycle, but also in subsequent cycles. On the other hand, the maximum stress, measured in the *Loading step* has an ascending tendency as the number of cycles increases. For the cycles performed to strain rate of $10^{-3}\ s^{-1}$, the average of σ_{max} rises from 0.43 MPa to 1.52 MPa (Figure 3.26(c)), differently for the strain rate of $10^{-1}\ s^{-1}$, the average of σ_{max} moves up from 0.91 MPa to 3.32 MPa (Figure 3.27(c)).

3.4 Uniaxial characterization

3.4.1 Uniaxial tensile tests Laminated foil material

In Figure 3.28 the true stress-strain curves below and above the transition temperature, up to 15% of strain, are reported.

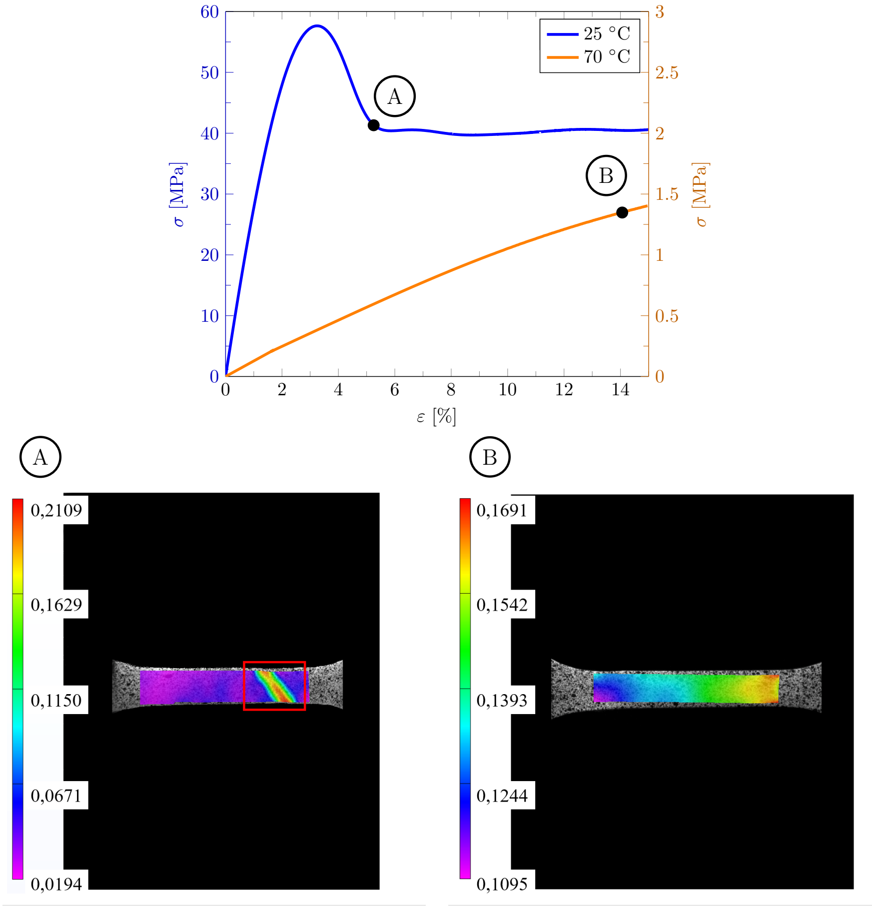

Figure 3.28: Experimental Stress and Strain curves at two different temperatures with DIC measured strain fields.

Here it is possible to observe that at 25°C the material exhibits the typical mechanical response characterized by an elastic phase reaching the upper yield point, followed by a softening behaviour and a constant plateau region (as also reported in section 3.3.3); here the DIC measurement highlights the formation on a necking zone, as shown in Figure 3.28A. Differently, above the glass transition temperature of the material, namely 70°C, the material shows an almost liner behaviour, in accordance with the rubbery nature, without the formation of necking (Figure 3.28B). The Young's modulus and the Poisson's ratio determined from the tests are reported in Table 3.9.

Table 3.9: Region properties

	Glassy Region	**Rubbery Region**
E [MPa]	2460	13
ν	0.29	0.49

3.4.2 Uniaxial thermomechanical test Laminated foil material

The efficiency of the SME of the SMPU laminated foil, in terms of Fixity and Recovery ratios, has been estimated by performing an uniaxial thermomechanical cycle. In Figure 3.29 is reported the cycle performed at 70°C and 20% of prescribed strain. In particular, according to Equation 1.1 and Equation 1.2, from the curve of the cycle has been possible to determine the Fixity ratio $R_f = 99.14\%$ and the Recovery ratio $R_r = 83.67\%$.

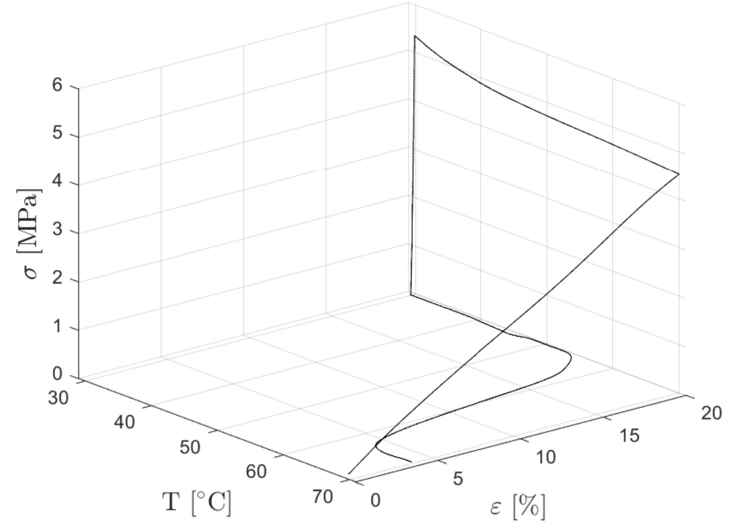

Figure 3.29: Thermomechanical uniaxial cycle.

These data, together with the elastic properties in the Glassy and Rubbery region of SMPU retrieved from the pure uniaxial tensile tests, have been used to calibrate the HBT simulation.

3.5 Biaxial characterization

3.5.1 Literature review

A large number of studies concerning the effects of environmental factors dependence on the thermomechanical behaviour of SMPs were investigated experimentally, but including only few experimental data on a thin film of shape memory polymers. Hence, along with the need to investigate the behaviour of the SMPs above the T_g, Poilâne et al. (2000) [107] have conducted a non-conventional mechanical tests, such as nanoindentation, bulging and point membrane deflection. The indicated kind of test has often been utilized to perform biaxial tensile tests on rubbers and polymers at room temperature [108]. Hydraulic bulge test in a temperature-controlled environment has been performed by Lee et al. (2014) [109] on advanced high strength steels under warm conditions (test temperature below 100°C); in this case, the experimental setup employed a LVDT combined to an extensometer in order to provide a simultaneous measurement of the bulge height and the in-plane elongation at the pole of the specimen simultaneously. By Kalkman et al. (2003) [110], a high-temperature bulge test was developed for the elastic and plastic behaviour of thin films, employing a scanning laser beam for retrieving the bulge dome height. The application of the Digital Image Correlation technique [111], in fact, allows the determination of the full-field deformation history on the specimen surface, offering the capabilities to include the observation of gradients and inhomogeneities associated with the material behaviour or loading conditions.

3.5.2 Glass Transition Temperature of Laminated Foil material

The material used for the biaxial characterization is always an SMPU, but obtained by lamination process and with different transition temperature, differently from the one used in section 3.3. For this reason, some DSC analyses were carried out to detect the exact transition temperature, according to the procedure described in section 3.2.1.

In Figure 3.30 is reported the normalized heat flow versus temperature, in the range from 0°C to 240°C. Due to the absence of other thermal events beyond the glass transition temperature (T_g), the DSC analysis for the SMPU laminated foil, was evaluated in the temperature range 40-80°C, as reported in Figure 3.31.

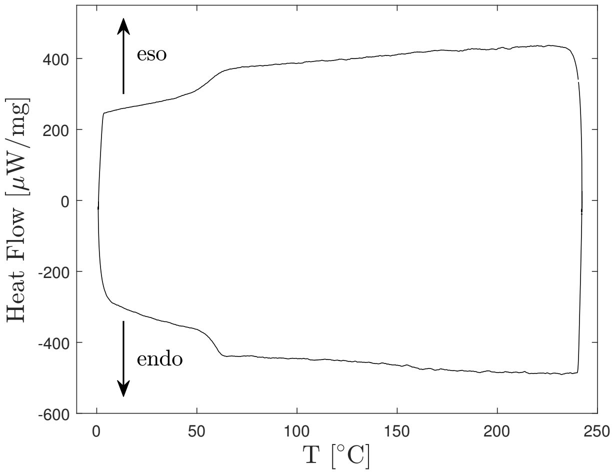

Figure 3.30: Total DSC result of SMPU laminated foil.

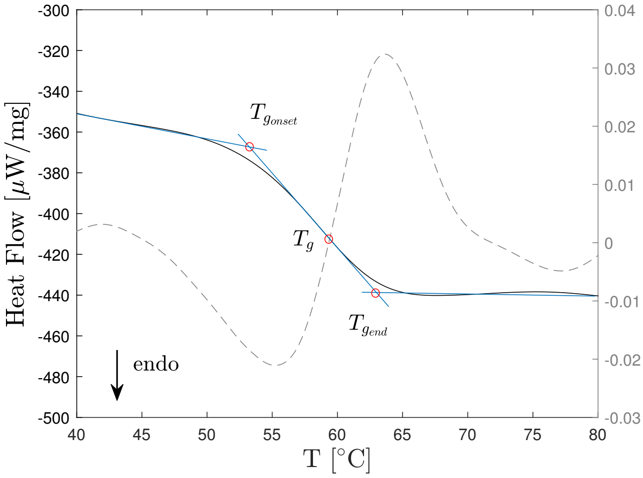

Figure 3.31: DSC result of SMPU laminated foil, where the dashed line represent the second derivative of the heat flow.

As described before, the definition of the glass transition region was determined by the intersection of two points obtained from: two lines ideally continuing the baseline before and after the transition and the line corresponding to the inflection point of the curve. For an accurate determination of this value, it has been obtained by the maximum of the numeric second derivative of curve reported as dashed line in Figure 3.31. In particular, can be observed that the transition starts at the onset temperature $T_{g_{onset}}$ equal to 53.30°C and ends at the transition $T_{g_{end}}$ equal to 63.48°C. The glass transition temperature, T_g, has been determined as the inflection point, equivalent to 59.45°C. Here, the glass transition region, between $T_{g_{onset}}$ and $T_{g_{end}}$, is higher compared to that of the pellet determined before.

Given this result, T_g is not only the glass transition temperature, but also shape recovery temperature in thermally responsive SMPs, at which the SME is activated. To activate the SME and have the soft segment free to move, resulting in flexible and deformable state of the material, the thermomechanical cycles were carried out at T_{trans} higher than the $T_{g_{end}}$ temperature of 70°C.

3.5.3 Biaxial Thermomechanical Characterization

Strain profiles during the thermomechanical cycle

In order to perform, the thermomechanical tests in balanced biaxial stress condition, a HBT machine was used. Here, in Figure 3.32, the comparison between the deformation along x and y is reported. The red line describe the ideal case in which the strain ratio is equal to one, so when the deformations are perfectly equal in both directions during the test. Furthermore, two steps of the thermomechanical cycle can be observed, namely the *Loading* and *Reheating step*. In the *Loading step*, represented by the black curve below the red one, the strain ratio is very close to the ideal strain ratio, resulting in a biaxial strain state. On the contrary, in the *Reheating step*, represented by the black curve above the red one, the strain ratio is different and not very close to

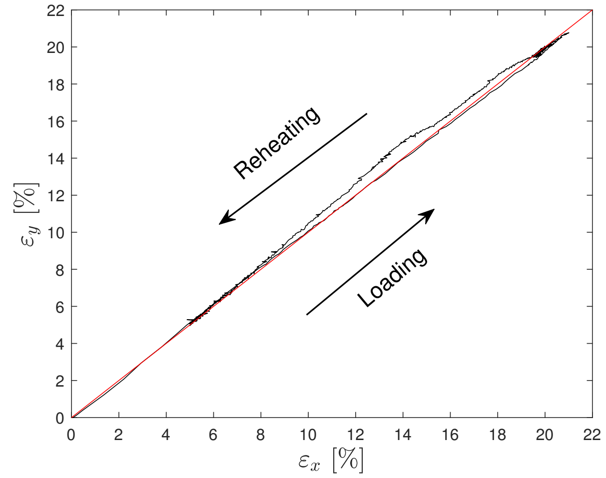

Figure 3.32: Comparison between the deformation along x and y.

the ideal strain ratio, resulting in a not perfectly biaxial strain state. The imperfect deformation ratio is maintained until the deformation comes to an asymptotically stabilized, achieved at the end of the step.

This result is more visible in Figure 3.33, where the trend of strain, ε_x and ε_y, during the overall thermomechanical cycle, are depicted. Analysing the curves, it is possible to notice that the deformation values, after the unloading deformation ε_u, are different up to the point of reaching the same deformation ε_{ir}, in x and y direction.

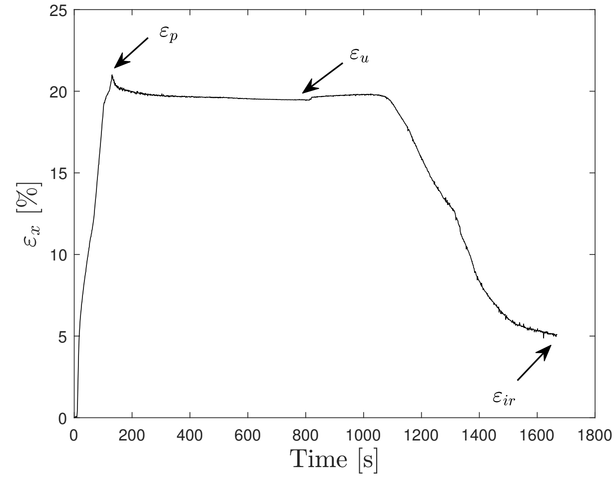

(a)

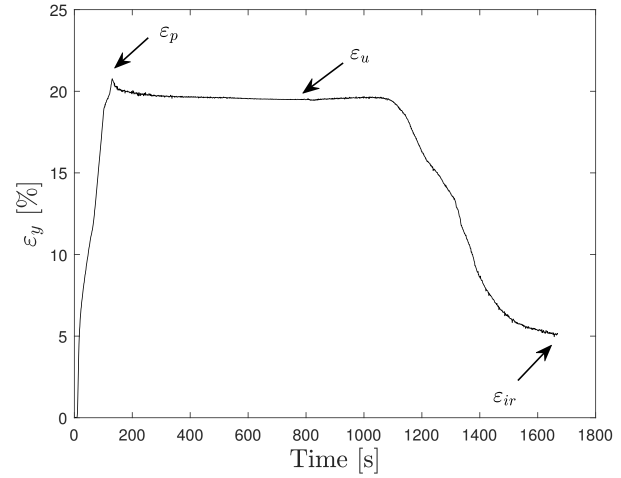

(b)

Figure 3.33: Deformation along x direction (a), y direction (b).

More specifically, evaluating the deformations in the individual step of the thermomechanical cycle, it is possible to determine the Fixity and Recovery ratio. In particular, at the end of the *Loading step* a prescribed deformation ε_p is about 21% was achieved, in both directions. After the *Loading step*, the reached pressure was maintained throughout the *Cooling step*, until the temperature decreased below the T_{trans}. In the strain pattern shown in the figure, after reaching $varepsilon_p$, the strain decreases until it stabilizes. The decrease of the strain, is mainly due to the cooling rate as well as the presence of a temperature gradient along the radius of the specimen. When the pressure was unloaded to get the zero-stress condition, the corresponding unloading strain ε_u is about 19.45%. This represents the amount of the deformation, that the material can store from the previous step, resulting in a Fixity ratio of 92.62%. Finally, heating again without any constraints, the specimen reacted by recovering its initial shape, up to the irrecoverable deformation ε_{ir} around 5.10%. The Recovery ratio determined at the end of thermomechanical cycle was 76.35%.

Determination of biaxial stress-strain curves

To find out the biaxial stress-strain curve, a simple membrane stress state of a thin-walled spherical pressure vessel is assumed. This simplification implies that, according to ISO/DIS 16808 [13], the equi-biaxial tensile stress caused by internal pressure in thin walled structures was calculated according to the equation:

$$\sigma_1 = \sigma_2 = \frac{PR}{2t}, \qquad \sigma_3 = 0 \tag{3.3}$$

In particular, P was the pressure of the water, measured by a pressure transducer and depicted in Figure 3.35(a). Differently, the curvature k, determined throw the DIC technique were used to define R, that represent the radius of curvature. In order to obtain a stable radius of curvature, a best-fit sphere can be calculated on the basis of a circular area defined by a radius r_1 (see Figure 3.34), with centre at the apex of the dome defined at the end of the *Loading step*.

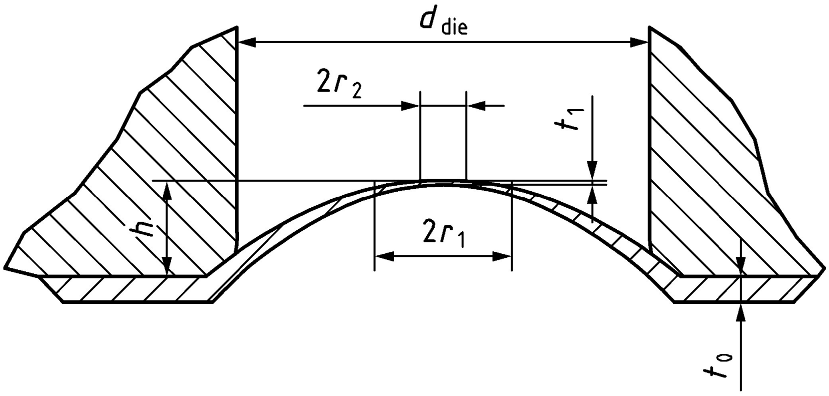

Figure 3.34: Choice of r_1 and r_2 for calculation of true stress and true strain. Reproduced from [13].

$$r_1 = (0,125 \pm 0,025) \times d_{die}$$

$$r_2 = (0,05 \pm 0,01) \times d_{die}$$

The mean curvature radius R, was determined according to the following equation and the trend is reported in Figure 3.35(b)

$$R = \frac{1}{k}, \qquad k = \frac{1}{2}(k_{xx} + k_{yy})$$

On the other hand, for valid values of the actual deformation and thinning in the apex, the average value is taken over a second circular area, defined by a radius r_2 (see Figure 3.34). Assuming total deformation over the thickness by the total major and minor true strain:

$$\delta_3 = ln(\varepsilon_3 + 1) = -(\delta_1 + \delta_2)$$

Finally, the thickness t were defined by using the deformation and the initial thickness of the specimen t_0. In Figure 3.35(d) the thickness evolution is shown.

$$t = t_0 e^{\delta_3}$$

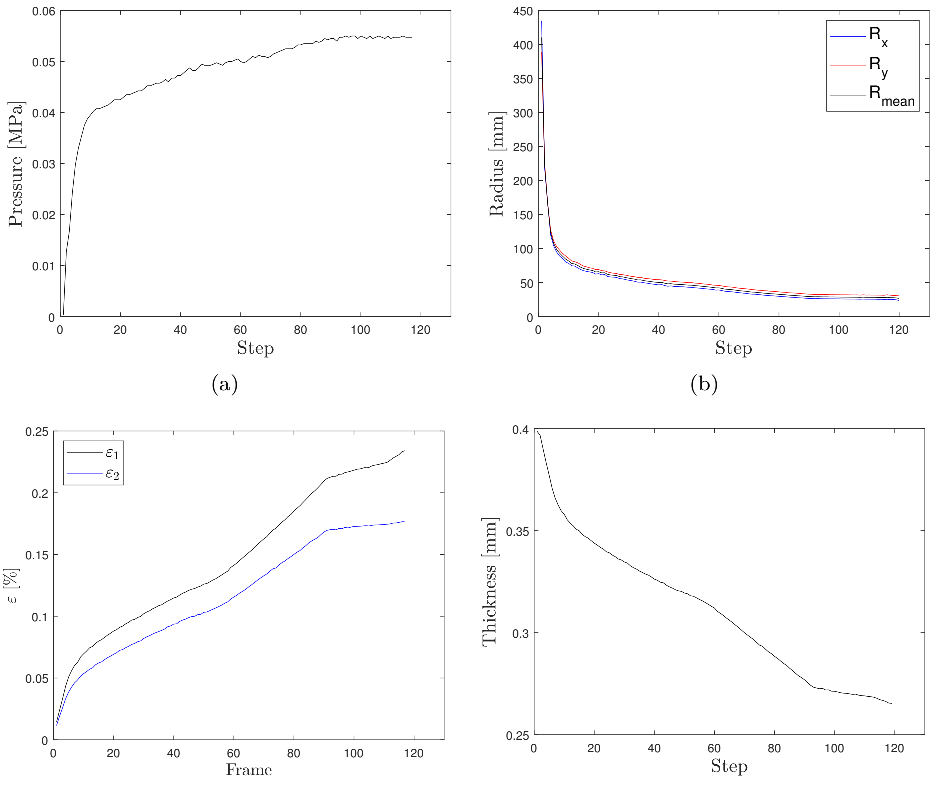

(a) (b)

(c) (d)

Figure 3.35: Pressure (a), Radius of curvature (b), Strain (c) and Thickness (d) trend during the loading step.

Using the above approaches and equations for the bulge radius and thickness measurements/calculations, the stress curve was determined and reported in Figure 3.36.

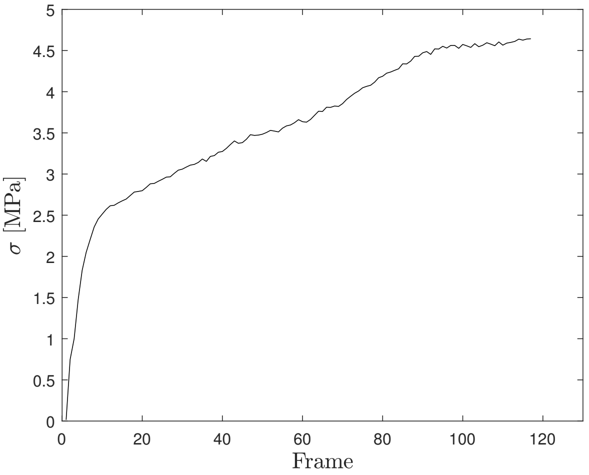

Figure 3.36: Stress trend during the loading step.

Finally, the stress strain curve, according to Equation 3.3, is determined and reported in Figure 3.37.

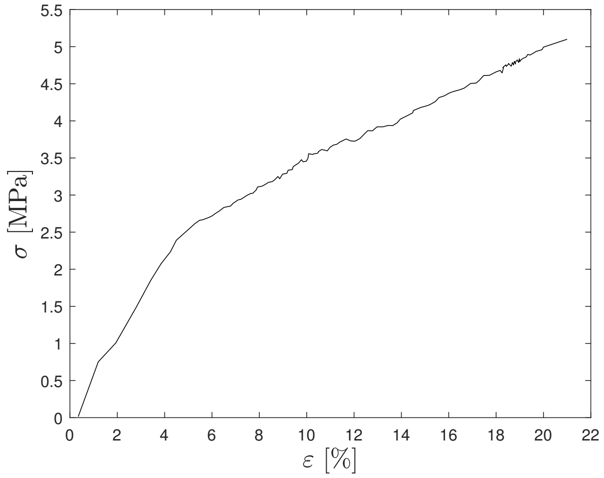

Figure 3.37: Stress — Strain biaxial curve during the loading step.

Dome profile

Figure 3.38 shows the DIC measured displacement of the bulge in the out-of-plane direction at the end of each step of the thermomechanical cycle.

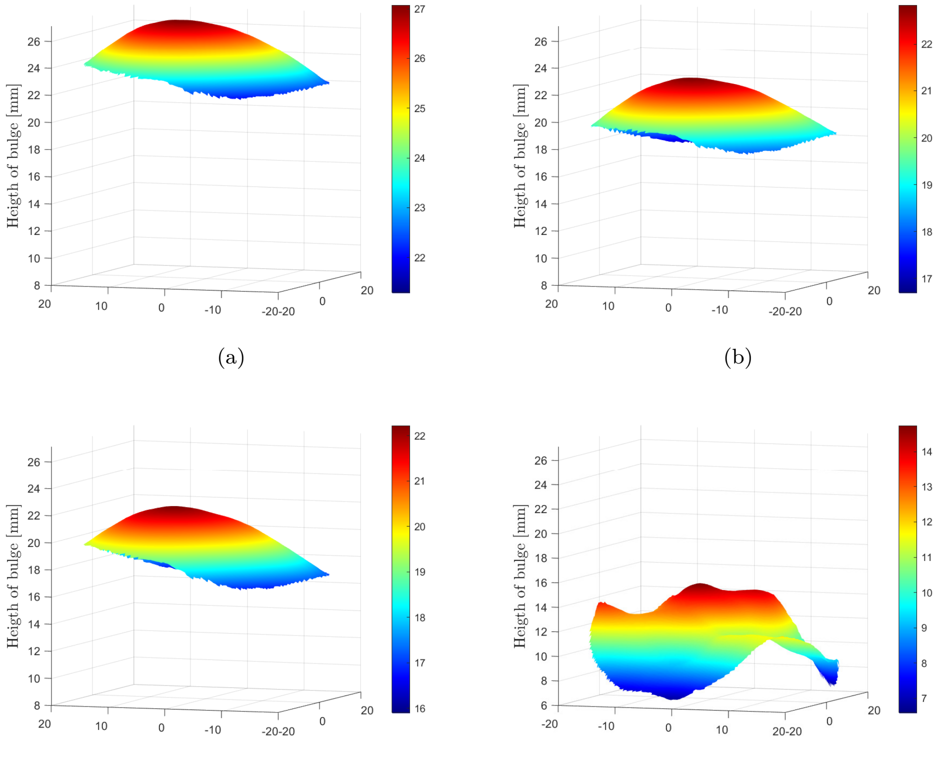

(a) (b)

(c) (d)

Figure 3.38: Displacement of the bulge in the out-of-plane direction for Loading step (a), Cooling step (b), Unloading step (c) and Reheating step (d).

- Loading step: initially the specimen was uniformly heated at 70°C and then the pressure was applied, the specimen reached with a pressure of 0.3 bar a maximum of the dome at 27 mm as depicted in Figure 3.38(a).
- Cooling step: the pressure was kept constant reaching a pressure of 0.33 bar at the end of the cooling step and the apex of the dome dropped to 22.8 mm as shown in Figure3.38(b), at this point the pressure was removed.
- Unloading step: at the end of unloading step without pressure applied, a temporary shape was fixed and the maximum of the dome reached 22.2 mm as shown in Figure 3.38(c).
- Reheating step: by heating again the specimen at the end of the reheating step, the original shape is recovered but not uniformly, reaching 14.6 mm as a maximum and 7.4 mm as a minimum, as depicted in Figure 3.38(d).

The height of bulge vs radius curves of the dome, extrapolated from experimental results at the end of four different steps of the test are depicted in Figure 3.39. The profiles of the dome were determined by averaging over the radius.

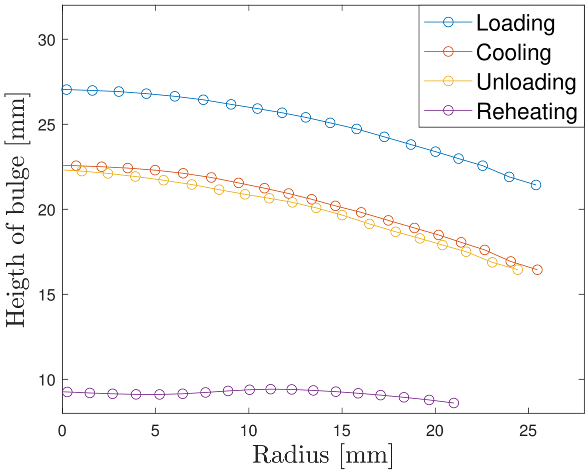

Figure 3.39: Height of bulge vs radius curves at the end of different step.

Biaxial thermomechanical cycle

According to the stress determined previously, the strain and the temperature (monitored during the thermomechanical bulge test), the biaxial cycle performed is reported in Figure 3.40.

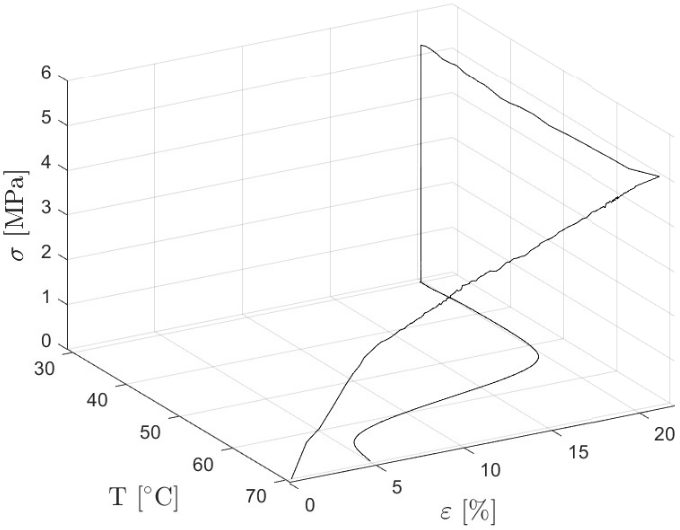

Figure 3.40: Biaxial thermomechanical cycle.

Chapter 4

A constitutive model for the thermomechanical behaviour of SMP

4.1 Literature review of constitutive models

The increasing use of SMPs in the design of intelligent devices requires not only an investigation of the mechanical behaviour, but also the introduction of a constitutive model to describe the material. In terms of constitutive modelling, countless advances have been made in recent years from the previous simple stress-strain relationships [112]. However, a generic constitutive model is not able to provide reliable results on SMPs due to different material behaviour. The description of shape memory behaviour is very difficult, given the large number of existing polymers and the external stimuli that responds [113].

In particular, Nguyen et al. (2008) [114] examined the effects of stress relaxation on the structure of amorphous SMPs, by incorporating the nonlinear Adam-Gibbs relaxation model and modified Eyring viscous flow model into the continuum finite deformation thermoviscoelastic framework. Based on the tensile experiment of styrene SMP, a numerical simulation analysis in Zhou et al. (2009) [115] established the three dimensions constitutive equation. However, many developed models have been studied for thermo-responsive SMPs, as Habibao et al. (2013) [116].

Mainly, in literature, for describing the behaviour of thermo-responsive SMPs two different approach are used. The first, as in Diani et al. (2006) [117], is based on the study of viscoelastic behaviour models commonly used to simulate polymers and better describe the physical mechanisms. Differently, the second is based on the phase transition of the material, in particular, a rule of mixture is used. Basically, the models are based on Young's modulus variation with the temperature: assumed softer at high temperature (referred to the Rubbery region) and harder at low temperature (referred to Glassy region). For this reason, the strain in the SMP segment is decomposed into two components, a fraction of the material is in the glassy state while the residual is in the rubbery state [118, 119, 120, 121].

Hence, the main difference is that the first approach better describes the viscoelastic behaviour of the polymer, such as chain mobility, whereas the second reproduces the overall macroscopic behaviour of the material.

4.2 The approach of constitutive model

In this thesis, the material model employed to describe the shape memory behaviour of the SMPU is the one proposed by Boatti et al. (2016) [48].

This three-dimensional finite-strain phenomenological model, is based on the temperature-dependent response of SMPs, identifying different regions corresponding to the Glassy and Rubbery region, respectively above and below the T_{trans}. In particular, the model describes the four steps in Figure 1.13, and consider allows to employ the parameters describing both the imperfect shape-fixing and incomplete shape-recovery.

$$\sigma = z^g \sigma^g + (1 - z^g)\sigma^r \tag{4.1}$$

The total Cauchy stress σ can be derived through a rule of mixture, where the Cauchy stresses for the glassy and rubbery phases are considered. The Cauchy stresses can be derived according to:

$$\begin{cases} \sigma^g = J^{eg-1} F^{eg} S^{eg} F^{egT} \\ \quad \sigma^r = J^{r-1} F^r S^r F^{rT} \end{cases} \tag{4.2}$$

The expression of the second Piola-Kirchoff stress tensors of the phase glassy (S^g), rubbery (S^r) and thermodynamic force (X^g) related to the plastic deformation are reported:

$$\begin{cases} S^g = F^{pg-1}(\lambda^g tr(E^{eg})I + 2\mu^g E^{eg})F^{pg-T} - 3\alpha^g k^g(\theta - \theta_{ref})I \\ \qquad S^g = \lambda^g tr(E^{er} I + 2\mu^r E^{er}) - 3\alpha^r k^r(\theta - \theta_{ref})I \\ \qquad X^g = C^{eg}(\lambda^g tr(E^{eg} I) + 2\mu^g E^{eg}) - hF^{pg} E^{pg} F^{pgT} \end{cases} \tag{4.3}$$

Otherwise the amount of phases present at a given temperature is regulated by z^g, that represent the volume fraction of the glassy phase and results function of the transition temperature as show below:

$$z^g = \begin{cases} 1 & if\ \theta \leq \theta_t - \Delta\theta \\ \frac{1}{1+e^{2w(\theta-\theta_t)}} & if\ \theta_t - \Delta\theta < \theta < \theta_t + \Delta\theta \\ 0 & if\ \theta \geq \theta_t + \Delta\theta \end{cases} \tag{4.4}$$

where θ_t is the transition temperature and $\Delta\theta$ represents the half-width of the transition temperature range, differently the parameter w is a positive constant related to the smoothness of the curve within the transition temperature range. According to the Equation 4.4, z^g is dependent from the temperature θ, is equal to 0 when the material is in the rubbery state, while is equal to 1 when the material is in the glassy state.

4.3 Calibration of the model

A three-dimensional finite element model of Hydraulic Bulge Test (HBT) have been developed to simulate the thermomechanical tests and then compared with the experimental data obtained.

Aiming to calibrate the SMP constitutive model, the elastic properties associated with the Glassy and Rubbery regions of the SMPU and the Fixity and Recovery ratios are essential to describe the non-ideal SME behaviour in numerical simulation. These parameters have been retrieved from uniaxial tensile tests and a thermomechanical cycle, conducted under controlled temperature.

4.3.1 Calibration of the parameters

In order to properly determine the calibration parameters for the constitutive model, the results of the experimental tests reported in the previous section has been used. Starting with DSC analysis in section 3.5.2, to determine the transition temperature (θ_t) of the material and the temperature range of the transition region ($\Delta\theta$), through to the determination of Young's modulus and the Poisson's ratio from tensile tests in the Rubbery and Glassy region, E^r, E^g, ν^r and ν^g respectively (reported in section 3.4.1). Finally, the uniaxial thermomechanical test, shown in section 3.4.2, has been necessary to determine the c and c_p coefficients, which indicate how efficiently the material is able to maintain the temporary shape and recover the original shape. The model parameters are reported in Table 4.1. Additionally, in the Table are listed two different coefficients of c and c_p, which are used differently to simulate the ideal and non-ideal case, in which the material maintains perfectly or imperfectly the temporary shape and recovers correctly or incorrectly the original shape in the last step of the thermomechanical cycle.

Table 4.1: Model parameters non-ideal case

Symbol	**Value**	**Unit**
E^r	13	MPa
E^g	2460	MPa
ν^r	0.49	
ν^g	0.29	
$\Delta\theta$	10	K
θ_t	330	K
w	0.2	K^{-1}
c	0.9914 (non-ideal case) — 1 (ideal case)	
c_p	0.1633 (non-ideal case) — 0 (ideal case)	

4.4 Numerical results

The numerical results obtained, by the reported calibration parameters above, are shown in Figure 4.1, where is noticeable the differences between the ideal and the non-ideal cases.

Analysing the results it is possible to observe that, in the *Loading step* (time instant between 1 and 2 s in Figure 4.1(a, b) and Figure 4.1(c)) the behaviour among ideal and non-ideal cases is the same. Differently, the ability of the model to represent the imperfect shape-fixing of the non-ideal case, is demonstrated during the *Cooling step*, where an increment of stress is produced (time instant between 2 and 3 s in Figure 4.1(b)), due to the increased stiffness of the Glassy region in which the material is arriving. In addition, during the *Unloading step* the stress decreases until zero is reached (time instant between 3 and 4 s in Figure 4.1(b)), producing an elastic return of deformation, meaning only a part of the strain is accumulated (time instant between 3 and 4 s in Figure 4.1(a)). Otherwise, in the ideal case, all the applied prescribed strain is stored as “frozen”, leading to perfect strain maintenance (time

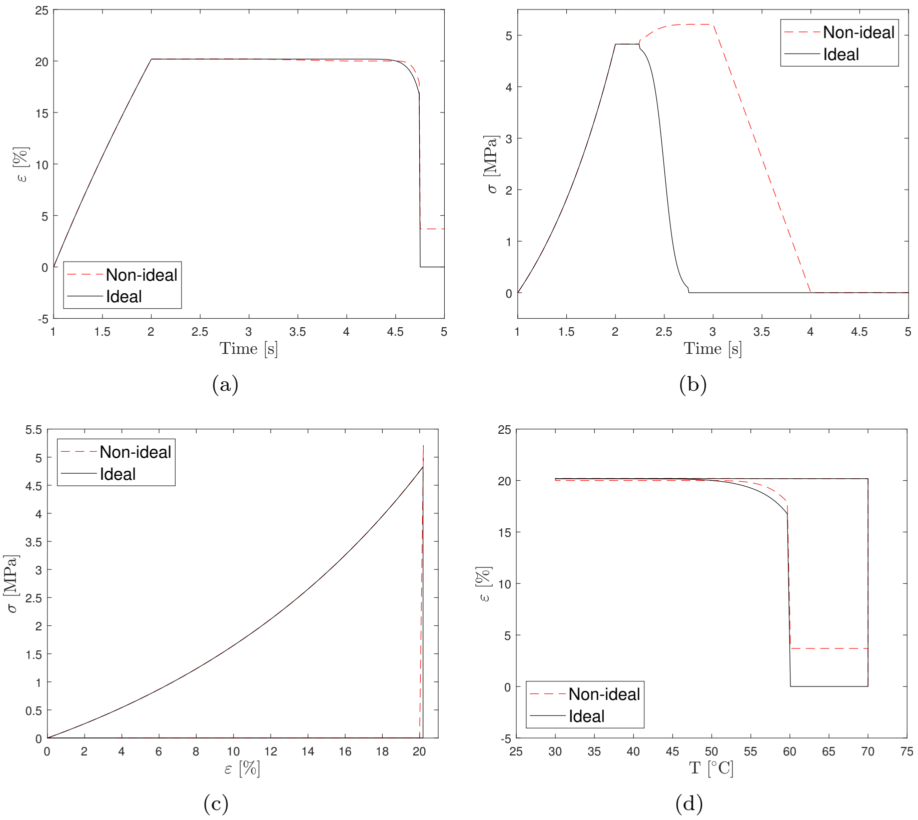

(a)

(b)

(c)

(d)

Figure 4.1: Comparison between ideal and non-ideal case: Strain vs Time curve (a); Stress vs Time curve (b); Stress vs Strain curve (c); Strain vs Temperature curve (d).

instant between 3 and 4 s in Figure 4.1(a)) and a zero-stress condition at the end of the *Cooling step* (time instant between 2 and 3 s in Figure 4.1(b)).

On the contrary, the ability of the model to represent the imperfect shape-recovery, can be noted in Figure 4.1(d) and at time instant between 4 and 5 s in Figure 4.1(a), where the final strain is different. In particular, in the ideal case the strain returns to zero, while in the non-ideal case a residual strain is present, thus representing the two cases in which the original shape is totally or partially recovered.

4.5 Finite Element Model

The Finite Element (FE) models of uniaxial and biaxial test were developed in the nonlinear commercial code ABAQUS/Standard®. The material was implemented in the FE code by means of a material user subroutine (UMAT), used in previous work in literature by Boatti et al. (2016) [48].

4.5.1 Uniaxial model

The numerical model of the uniaxial thermomechanical test has been composed by the dog-bone specimen (see Figure 4.2), with a gauge length of 25 mm and a thickness of 0.4 mm. Due to the low number of elements, the model symmetry has not been exploited. Nevertheless, the calculation time has been maintained extremely short. The specimen has been discretized by using 8-node full-integration brick elements (C3D8) and one element has been assigned through the thickness. The thermomechanical test information about the geometry and the characteristic of the used FEM uniaxial model are listed in Table 4.2. Fixed boundary conditions have been imposed to one side of the specimen, while on the other side a displacement has been applied to describe the movement of the tensile machine. Regarding the temperature have been applied to the whole specimen, in order to activate the SME. The FE mesh of the specimen is reported in Figure 4.6. Specifically, the sequence of the loading histories that has been

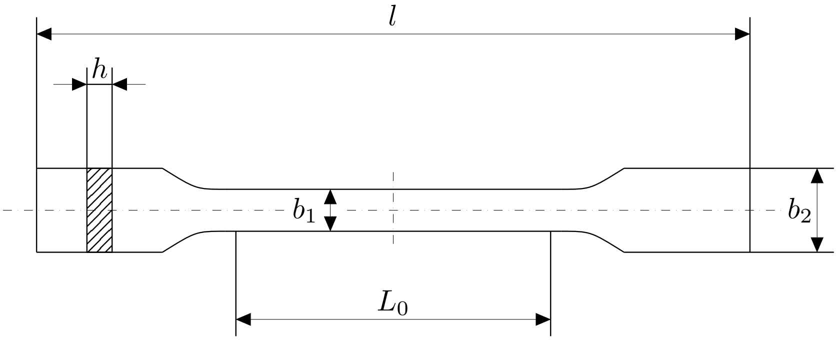

Figure 4.2: Dog-bone specimen of the uniaxial thermomechanical test FE model.

Table 4.2: Characteristics of the FE model

Geometry		FEM characteristics	
Gauge length L_0	25 mm	Type of element	C3D8 (8-nodes, full-integration)
Overall length l	85 mm		
Thickness h	0.4 mm	Number of elements	560
Width at narrow b_1	7 mm		
Width at ends b_2	14 mm		

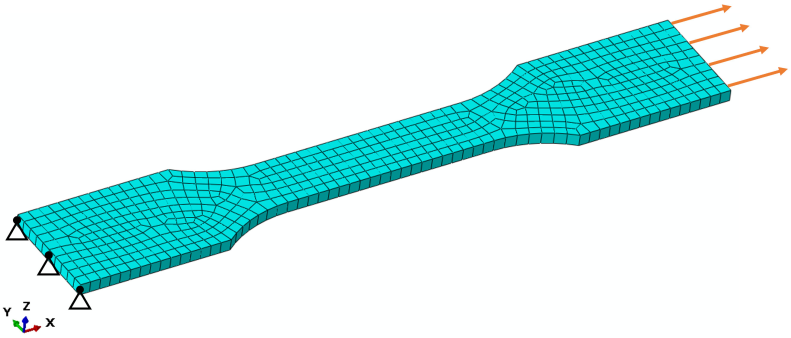

Figure 4.3: Schematic view of the finite element model of the thermomechanical tensile test.

applied to simulate the tests performed, in terms of the imposed displacement and assigned temperature, is depicted in Figure 4.7.

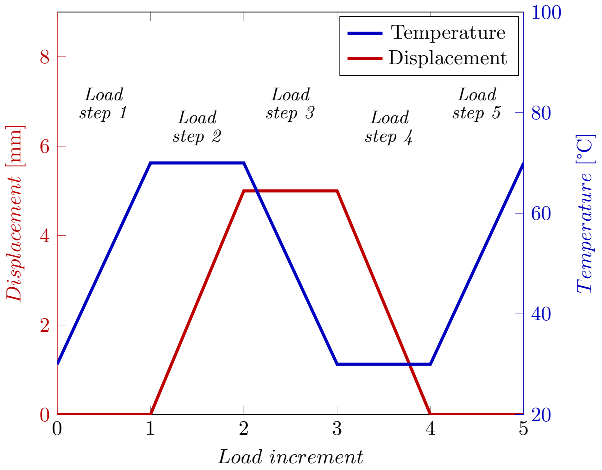

Figure 4.4: Loading histories for the thermomechanical tensile test simulation.

In the simulation high-temperature shape-fixing has been performed, according to Figure 1.13. Initially, the fixed boundary condition have been applied without any load and the temperature has been raised above the T_{trans} (*Load step 1*). Then, the displacement has been applied at temperature of 70°C (*Load step 2*) and subsequently, cooled to 30°C while the displacement has been maintained constant (*Load step 3*). Subsequently, the material has been unloaded at low temperature (*Load step 4*), in order to reach the zero-stress condition. Finally, the temperature has been increased again up to 70°C to trigger shape-recovery, while the specimen has been not constrained (*Load step 5*).

4.5.2 Biaxial model

Basically, the numerical model of the bulge test is composed by two main parts: a thin sheet (specimen) and a clamping ring (see Figure 4.5). In particular, the specimen and the ring have been modelled exploiting $\frac{1}{4}$ symmetry of the problem. The specimen has been discretized by using 8-node full-integration brick elements (C3D8) and two elements have been assigned through the thickness. In order to enhance the computational efficiency of the simulation, only the upper clamping ring has been introduced in the simulation, this latter modelled as an analytical rigid surface. Then, the tangential behaviour has been described by assuming a frictional contact between the upper clamping ring and the specimen surface, imposing a static frictional coefficient of $\mu = 0.35$, typical of polymer-steel surfaces. The geometry and the characteristics of the hydraulic bulge test simulation, used for implementing FE model, are listed in Table 4.3.

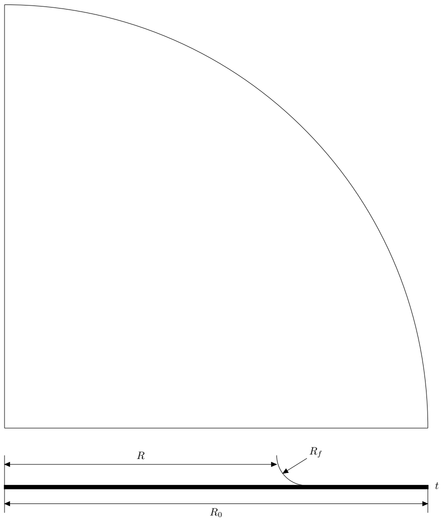

Figure 4.5: Membrane specimen and cross-section of the bulge test FE model.

Table 4.3: Characteristics of the FE model

Geometry of HBT		FEM characteristics	
Blank size R_0	140 mm	Type of element	C3D8
Die diameter R	90 mm		(8-nodes, full-integration)
Die fillet radius R_f	0.4 mm	Number of elements	8820
Thickness t	0.4 mm		

Fixed boundary condition have been imposed at the outer edge of the quarter of the specimen. The pressure has been applied to the inner surface of the specimen to describe the fluid flow underneath. Differently, the temperature has been applied to the whole specimen, in order to activate the SME. The FE mesh of the specimen is reported in Figure 4.6, where it can be noticed that the number of elements, and consequently the number of nodes, has been increased in the areas of contact with the upper clamping ring and in the central part. In particular, the sequence of the loading histories applied to simulate the tests performed, in terms of the imposed pressure and the assigned temperature, is depicted in Figure 4.7. In the simulation high-temperature shape-fixing has been performed, according to Figure 1.13. Initially, the temperature has been raised above the T_{trans} (*Load step 1*) without any load applied. Then, the pressure has been applied at temperature of 70°C (*Load step 2*) and subsequently, cooled to 30°C while the pressure has been maintained constant (*Load step 3*). At this point, the material has been unloaded at low temperature (*Load step 4*), in order to reach the zero pressure condition. Finally, the temperature has been increased again up to 70°C to trigger shape-recovery, while the specimen has been not constrained (*Load step 5*).

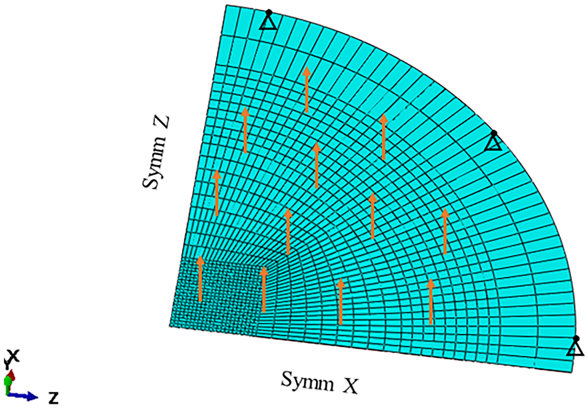

Figure 4.6: Schematic view of the finite element model of the thermomechanical bulge test.

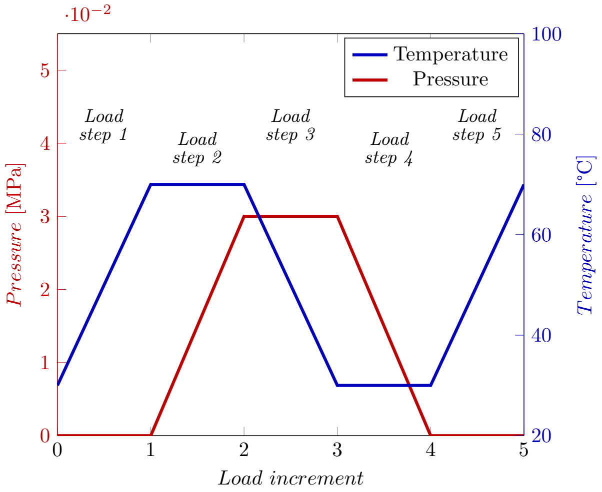

Figure 4.7: Loading histories for the thermomechanical bulge test simulation.

4.6 Comparison between numerical simulation and experimental data

Here, a comparison of the numerical results with the experimental data obtained is presented, to perform a validation of the model. In order to illustrate the use of the model, a comparison between free-recovery experimental tests and the numerical results has been made by considering two different types of stress states, the uniaxial and the biaxial. The free recovery test begins with a high-temperature shape fixity procedure; subsequently, the material is heated to trigger shape recovery, respectively, in an unconstrained condition to allow free recovery of the shape. The model parameters adopted for the comparisons of both stress states reported below, are listed in Table 4.1. Firstly, a comparison with the experimental results, in uniaxial stress state,

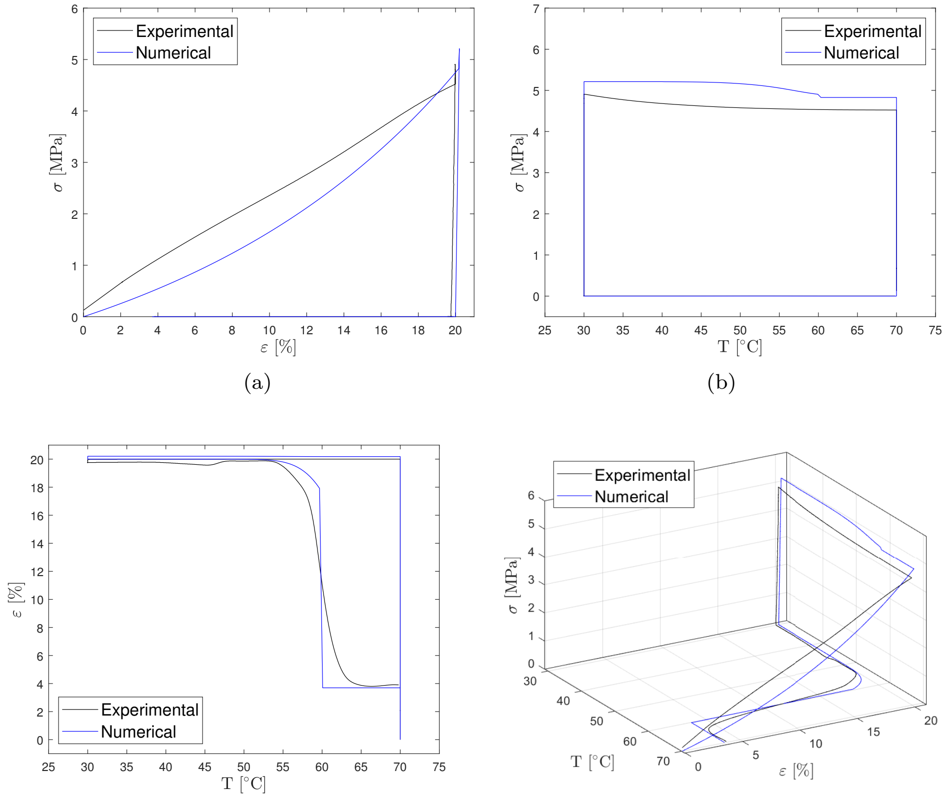

(a) (b)

(c) (d)

Figure 4.8: Comparison of thermomechanical uniaxial cycle between experimental data and numerical simulation. Stress vs Strain curves (a); Stress vs Temperature curves (b); Strain vs Temperature curves (c); Thermomechanical cycle curves (d).

presented in Figure 3.29 is provided. As can be seen in Figure 4.8(d), the numerical curve well represents the experimental thermomechanical cycle carried out, in terms of engineering stress, strain and temperature curve. More specifically, the numerical model underestimates the stress in the *Loading step* (Figure 4.8(a)), while overestimates it in the *Cooling step* (Figure 4.8(b)). Differently, the trend of the strain with temperature, in Figure 4.8(c), match well the experimental curve showing the capability of the model to replicate the imperfect shape-recovery.

In the following Figure 4.9(d), the comparison between the experimental data and the numerical model of the HBT is reported. As noted before, the numerical model underestimates the stress in the *Loading step* Figure 4.9(a), while overestimates it in the *Cooling step* (Figure 4.9(b)), also in the biaxial stress state. Furthermore, in comparison with the uniaxial case, the analysis shows that the ultimate strain is significantly lower in the simulated case, indicating that the SME is different from an uniaxial to a biaxial stress condition. In particular, the experimental thermomechanical cycle in biaxial condition points out a reduction of the Recovery ratio, whose value is $R_r = 76.35\%$, respect to the $R_r = 83.67\%$ in the uniaxial condition.

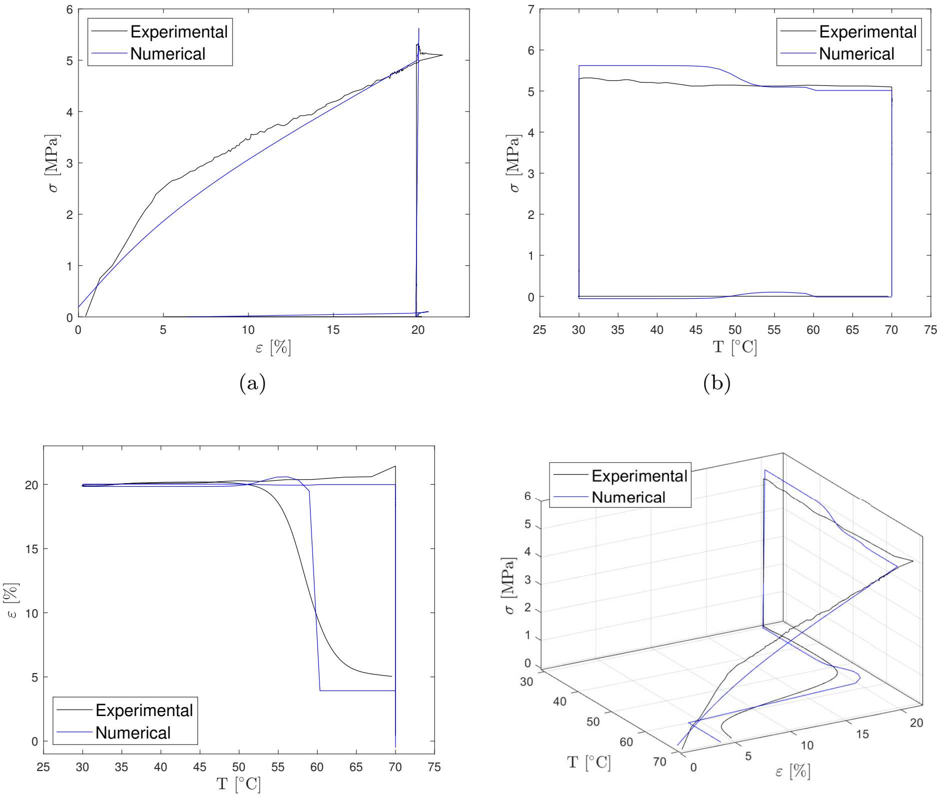

(a)

(b)

(c)

(d)

Figure 4.9: Comparison of thermomechanical biaxial cycle between experimental data and numerical simulation of HBT. Stress vs Strain curves (a); Stress vs Temperature curves (b); Strain vs Temperature curves (c); Trend of the height of bulge (d); Thermomechanical cycle curves (e).

Chapter 5

Conclusions

5.1 Conclusions and future developments

This thesis is focused on injection molding process and thermomechanical behaviour of thermoplastic SMPs. Regarding the injection molding process, the quality of the manufactured parts are mainly dependent on the used molding parameters, that can be controlled by the machine settings. Moreover, by installing the sensors on the mold, it is possible to collect real-time data and to continuously monitor what is occurring to the molten material inside the cavity. The use of sensors and acquired signals allow the improvement of the process quality and consequently the production, through the reduction of both cycle times and production waste. For what concerns the SMPs, among the mechanical properties, the SME is the most important one, representing the ability to memorize and to recover a temporary shape, fixed under appropriate conditions by an original shape. The activation of SME strictly depends on both the molecular architecture of the polymer and an appropriate thermomechanical sequence of external stimuli.

In the literature, uniaxial tensile and compression tests have been performed for investigating how the temperature affects the mechanical properties of the SMPs material. In the same way, the thermomechanical cycle of SMPs has been examined as a process with the variation of temperature and prescribed strain.

However, a systematic study focused on the combined effect of strain, strain rate and temperature on injection molded SMPs has not been yet conducted, to the best of author's knowledge. Therefore, the purpose of this research activity was to explore different stress states and the influence of specific variables (i.e., strain, strain rate and temperature), that characterize the thermomechanical cycle. In detail, the SME performance was assessed in terms of Fixity and Recovery ratios.

First of all, a mold has been designed to manufacture a standard specimen, employed in the analysis of the SMPs mechanical behaviour in quasi-static condition. Secondly, since the mold provides specimens compliant with both dimension and process, according to the standards ISO, either pressure and temperature sensors were installed to monitor the conditions inside the cavity. By using the in-mold sensors and the process simulations, injection molding parameters were optimized to reduce as much as possible the cycle time.

The material used in the experimental tests is a commercial shape memory polymers polyurethane based, whose chemical and physical properties were determined and verified through the DSC analysis. In the analysis performed, no other thermal events were detected, thus determining that the glass transition temperature corresponds to the transition temperature for SME activation of the material.

Regarding the test methodology, the uniaxial tensile, thermomechanical and cyclic tests were conducted by using an electromechanical testing machine, while the biaxial stress state was assessed by using a hydraulic bulge test machine. The entire experimental campaign was carried out by employing a climatic chamber to control the specimen temperature and to exploit the DIC technique to the deformation evolution on the specimen surface.

The uniaxial tensile tests, conducted at several temperatures in the Glassy, Glass Transition and Rubbery region, revealing a different yield behaviour that lead to a reduction of Young's modulus and an increment of Poisson's ratio.

Thermomechanical tests, during the loading phase, show a stress/strain behaviour, differing significantly with the strain rate. Differently, during the Cooling step of the specimen when constraints are applied, there is no relevant variation in stress until the temperature is reduced below the glass transition temperature. Thereafter, tensile stresses occur internally due to the increased polymer stiffness. By releasing the specimen after the cooling, the material exhibits an exceptional ability to maintain the temporary shape (resulting in high Fixity ratio). Then, when the polymer is reheated without any constraint, the shape recovery does not start until the temperature reaches the glass transition temperature. The polymer ability to recover the original shape has been measured in terms of Recovery ratio. Comparing the Fixity and Recovery ratios, it was found that the former results to be less influenced by the test conditions, with respect to the last one. In detail, an increase of the strain rate determines an improvement of the strain recovery capability (i.e., high Recovery ratio), almost independently of the prescribed strain and the temperature; conversely, the strain recovery is reduced as the test temperature or the prescribed strain increases.

The cyclic tests on the specimen exhibit high Fixity ratio (i.e., R_f), irrespective of strain rates variation and number of cycles. Differently, the values of $R_{r,tot}$ increase for specimens cycled at strain rate $10^{-1}\ s^{-1}$, while decrease as the number of cycles increases. As a result, the configuration including a strain rate equal to $10^{-1}\ s^{-1}$ achieves a better recovery of the original shape, with respect to that one cycled at $10^{-3}\ s^{-1}$. However, an elevated strain rate requires higher force to deform the material into temporary shape, hence greater stress levels in the Loading step (i.e., σ_{max}).

The SME behaviour was also studied in the biaxial stress state, by a HBT on a thin membrane of SMPU. The tests conducted shown, once more, an excellent fixation of the temporary shape, while an imperfect recovery of the shape in the last step of the thermomechanical cycle. This results in a worse recovery of the original shape in respect to the uniaxial case.

The experimental results presented in this thesis, indicate that the SME of the material is a function of strain, temperature and strain rate variation during the thermomechanical cycle, in addition to the number of thermomechanical cycles performed and the stress state. These details are essential to define the design space of a SMPs and to optimize, properties and performance for a defined application.

Finally, a constitutive model for SMPs was implemented in this thesis, in order to describe the SME. The model used, is based on a phase-transition approach and could be useful to represent the macroscopic phenomenology of the material to solve engineering problems. The material coefficients regulating the SMPs constitutive model were calibrated from uniaxial tensile and thermomechanical cycle. The efficiency of the model obtained was evaluated by comparing the uniaxial and biaxial (hydraulic bulge test) experimental data with numerical simulations. The FE validation shown the ability in reproducing both fixing and recovery of the shape, also providing the real material behaviour as imperfect shape-fixing and incomplete shape-recovery (by using Fixity and Recovery ratios).

This thesis revealed that the mechanical behaviour of SME is influenced by several parameters. Future developments of this work may be the extension of the values and unstudied parameters, as the cooling and heating rate, and the characterization of the SME through thermomechanical compression tests. This research may be extended to different kind of polymers and triggered by different external stimuli. In addition, the SME may be studied on other manufacturing process such as blow molding and thermoforming process.

Appendix

In Figure 5.1, 5.2 and 5.3 are shown all the thermomechanical cycle performed.

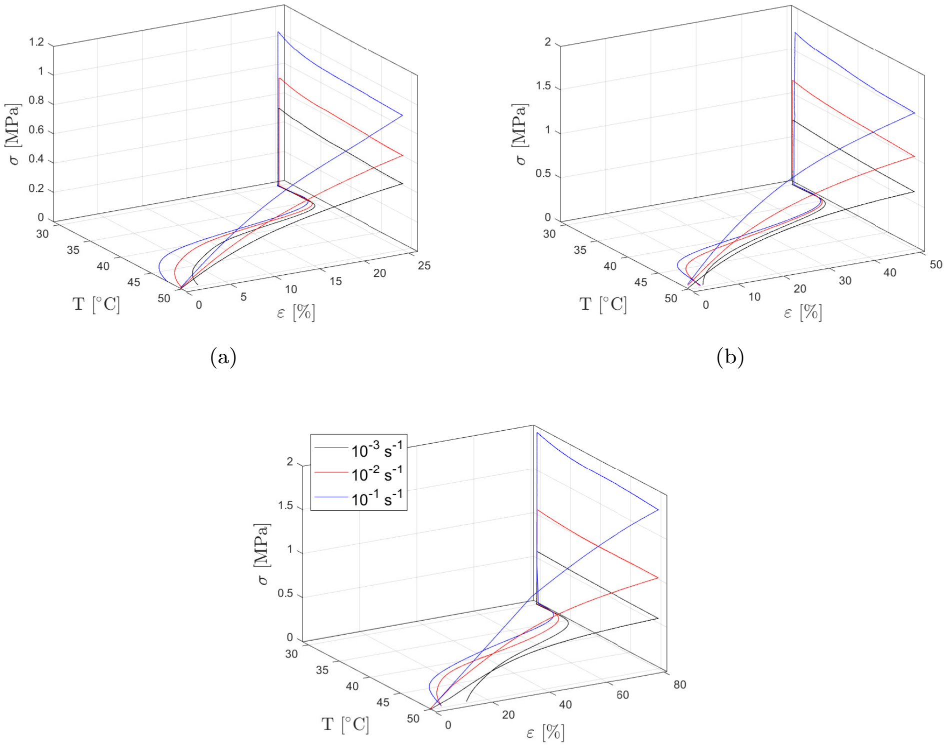

(a)

(b)

(c)

Figure 5.1: Thermomechanical cycle at 50°C and prescribed strain of 25% (a), 50% (b), 80% (c).

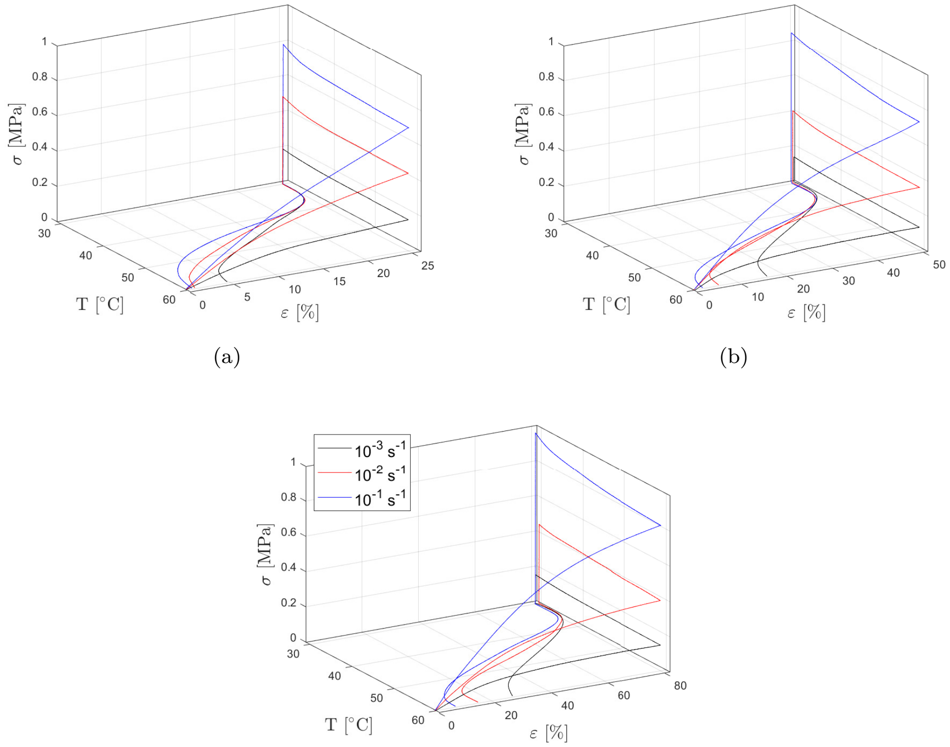

(a)

(b)

(c)

Figure 5.2: Thermomechanical cycle at 60°C and prescribed strain of 25% (a), 50% (b), 80% (c).

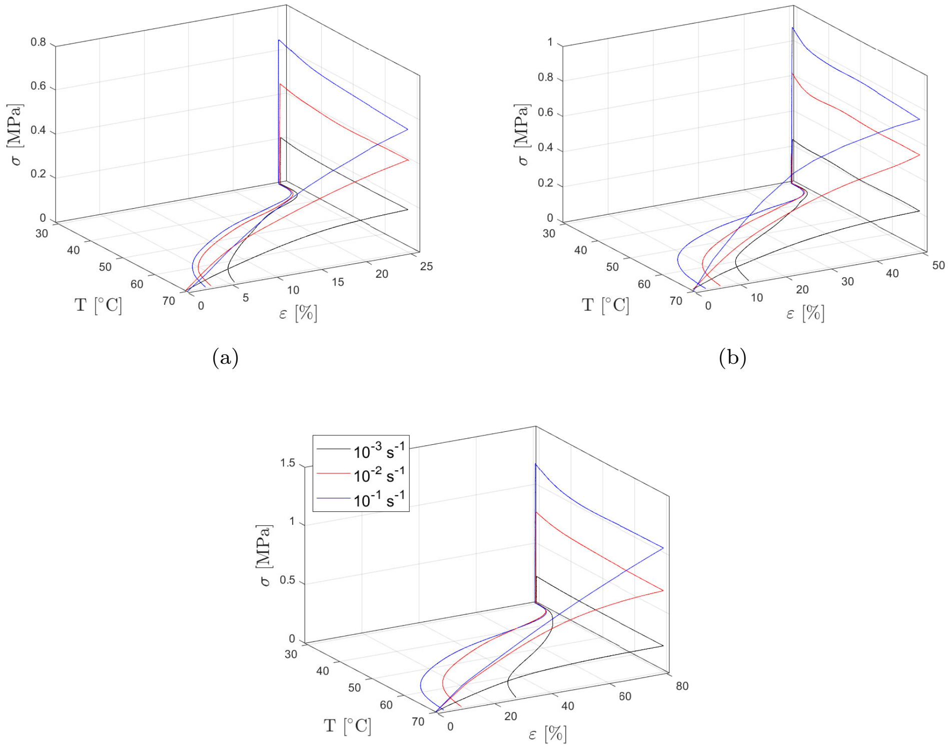

(a) (b)

(c)

Figure 5.3: Thermomechanical cycle at 70°C and prescribed strain of 25% (a), 50% (b), 80% (c).

Bibliography

[1] J. Gabor and J. Kovacs, *Analyzing the Warpage in the Injection Molding Using SLS Tool Inserts*, pp. 449–456. 01 2002.

[2] "Iso 527-1:2019 plastics — determination of tensile properties — part 1: General principles.," 2019.

[3] J. Milisavljević, E. Petrović, I. Ćirić, M. Mančić, D. Marković, and M. Đorđević, "Tensile testing for different types of polymers," in *DAS-29, 29th Danubia-Adria Symposium, University of Belgrade, Serbia*, pp. 266–269h, 2012.

[4] H. F. Brinson and L. C. Brinson 2015.

[5] M.-L. Wang, R.-Y. Chang, and C.-H. D. Hsu, "Molding simulation: Theory and practice," in *Molding Simulation: Theory and Practice* (M.-L. Wang, R.-Y. Chang, and C.-H. D. Hsu, eds.), Hanser, 2018.

[6] L. Sun, W. M. Huang, Z. Ding, Y. Zhao, C. C. Wang, H. Purnawali, and C. Tang, "Stimulus-responsive shape memory materials: a review," *Materials & Design*, vol. 33, pp. 577–640, 2012.

[7] G. Locati and A. Fiocca, "La «plastica». conoscerla per apprezzarla," in *La «plastica». Conoscerla per apprezzarla* (P. Editore, ed.), 2016.

[8] J. Shoemaker, "Manuale dello stampaggio progettato," in *Moldflow design guide: a resource for plastics engineers* (F. E. C. H. V. G. . C. KG, ed.), Tecniche Nuove, 2006.

[9] G. Bertacchi, "Manuale dello stampaggio progettato," in *Manuale dello stampaggio progettato*, Tecniche Nuove, 2002.

[10] T. Ageyeva, S. Horváth, and J. G. Kovács, "In-mold sensors for injection molding: On the way to industry 4.0," *Sensors*, vol. 19, no. 16, p. 3551, 2019.

[11] D. Sykutera, P. Czyżewski, A. Kościuszko, P. Szewczykowski, Ł. Wajer, and M. Bieliński, "Monitoring of the injection and holding phases by using a modular injection mold," *Journal of Polymer Engineering*, vol. 38, no. 1, pp. 63–71, 2018.

[12] J. Zhao, Y. Sang, and F. Duan, "The state of the art of two-dimensional digital image correlation computational method," *Engineering Reports*, vol. 1, no. 2, p. e12038, 2019. e12038 ENG-2019-04-0110.R2.

[13] "Iso/dis 16808:2012 determination of biaxial stressstrain curve by means of bulge test with optical measuring systems.," 2012.

[14] S. A. Abdullah, A. Jumahat, N. R. Abdullah, and L. Frormann, "Determination of shape fixity and shape recovery rate of carbon nanotube-filled shape memory polymer nanocomposites," *Procedia Engineering*, vol. 41, pp. 1641–1646, 2012. International Symposium on Robotics and Intelligent Sensors 2012 (IRIS 2012).

[15] K. Yu, Q. Ge, and H. J. Qi, "Reduced time as a unified parameter determining fixity and free recovery of shape memory polymers," *Nature Communications*, vol. 5, jan 2014.

[16] R. Bouaziz, F. Roger, and K. Prashantha, "Thermo-mechanical modeling of semi-crystalline thermoplastic shape memory polymer under large strain," *Smart Materials and Structures*, vol. 26, p. 055009, apr 2017.

[17] S. David, G. Dailyn, F. Francesc, S. Àngels, and D. la Flor Silvia, "Bio-based epoxy shape-memory thermosets from triglycidyl phloroglucinol," *Polymers*, vol. 12, no. 3, 2020.

[18] T. K. Kim, J. K. Kim, and O. C. Jeong, "Measurement of nonlinear mechanical properties of pdms elastomer," *Microelectronic Engineering*, vol. 88, no. 8, pp. 1982–1985, 2011. Proceedings of the 36th International Conference on Micro- and Nano-Engineering (MNE).

[19] A. Muc, P. Romanowicz, and M. Chwał, "Description of the resin curing process—formulation and optimization," *Polymers*, vol. 11, no. 1, 2019.

[20] E. J. B. and G. J. K., "Time–temperature–transformation (ttt) cure diagram: Modeling the cure behavior of thermosets," *Journal of Applied Polymer Science*, vol. 28, no. 8, pp. 2567–2591, 1983.

[21] D. Åkesson, M. Skrifvars, S. Lv, W. Shi, K. Adekunle, J. Seppälä, and M. Turunen, "Preparation of nanocomposites from biobased thermoset resins by uv-curing," *Progress in Organic Coatings*, vol. 67, no. 3, pp. 281–286, 2010.

[22] A. Crosky, N. Soatthiyanon, D. Ruys, S. Meatherall, and S. Potter, "9 - thermoset matrix natural fibre-reinforced composites," in *Natural Fibre Composites* (A. Hodzic and R. Shanks, eds.), pp. 233–270, Woodhead Publishing, 2014.

[23] X. P. Morelle, J. Chevalier, C. Bailly, T. Pardoen, and F. Lani, "Mechanical characterization and modeling of the deformation and failure of the highly crosslinked RTM6 epoxy resin," *Mechanics of Time-Dependent Materials*, vol. 21, pp. 419–454, jan 2017.

[24] Y. Singh, J. Singh, S. Sharma, T.-D. Lam, and D.-N. Nguyen, "Fabrication and characterization of coir/carbon-fiber reinforced epoxy based hybrid composite

for helmet shells and sports-good applications: influence of fiber surface modifications on the mechanical, thermal and morphological properties," *Journal of Materials Research and Technology*, vol. 9, no. 6, pp. 15593–15603, 2020.

[25] N. Hiremath, S. Young, H. Ghossein, D. Penumadu, U. Vaidya, and M. Theodore, "Low cost textile-grade carbon-fiber epoxy composites for automotive and wind energy applications," *Composites Part B: Engineering*, vol. 198, p. 108156, 2020.

[26] T. Yalcinkaya, "Synthesis and characterization of epoxy/boron nitride composite for aerospace applications," *Journal of Aeronautics and Space Technologies*, vol. 12, pp. 87–94, Jan. 2019.

[27] F. Schmidt, Y. L. Maoult, and S. Monteix, "Modelling of infrared heating of thermoplastic sheet used in thermoforming process," *Journal of Materials Processing Technology*, vol. 143-144, pp. 225–231, 2003. Proceedings of the International Conference on the Advanced Materials Processing Technology, 2001.

[28] E. Farotti and M. Natalini, "Injection molding. influence of process parameters on mechanical properties of polypropylene polymer. a first study.," *Procedia Structural Integrity*, vol. 8, pp. 256–264, 2018. AIAS2017 - 46th Conference on Stress Analysis and Mechanical Engineering Design, 6-9 September 2017, Pisa, Italy.

[29] C. Bauwens-Crowet, J. C. Bauwens, and G. Homès, "Tensile yield-stress behavior of glassy polymers," *Journal of Polymer Science Part A-2: Polymer Physics*, vol. 7, no. 4, pp. 735–742, 1969.

[30] M. Grasso, L. Azzouz, P. Ruiz-Hincapie, M. Zarrelli, and G. Ren, "Effect of temperature on the mechanical properties of 3d-printed pla tensile specimens," *Rapid Prototyping Journal*, 2018.

[31] Z. Jia, G. Yuan, H.-l. Ma, D. Hui, and K.-t. Lau, "Tensile properties of a polymer-based adhesive at low temperature with different strain rates," *Composites Part B: Engineering*, vol. 87, pp. 227–232, 2016.

[32] J. Wendorff, H. Finkelmann, and H. Ringsdorf, "Structure and morphology of liquid-crystalline polymers," in *Journal of Polymer Science: Polymer Symposia*, vol. 63, pp. 245–261, Wiley Online Library, 1978.

[33] J. Phillips, "Topology of covalent non-crystalline solids i: Short-range order in chalcogenide alloys," *Journal of Non-Crystalline Solids*, vol. 34, no. 2, pp. 153–181, 1979.

[34] H. Li, J. Fan, Z. Shi, M. Lian, M. Tian, and J. Yin, "Preparation and characterization of sulfonated graphene-enhanced poly (vinyl alcohol) composite hydrogel and its application as dye absorbent," *Polymer*, vol. 60, pp. 96–106, 2015.

[35] A. R. Torrado, C. M. Shemelya, J. D. English, Y. Lin, R. B. Wicker, and D. A. Roberson, “Characterizing the effect of additives to abs on the mechanical property anisotropy of specimens fabricated by material extrusion 3d printing,” *Additive Manufacturing*, vol. 6, pp. 16–29, 2015.

[36] S. Dıez-Gutiérrez, M. Rodrıguez-Pérez, J. De Saja, and J. Velasco, “Dynamic mechanical analysis of injection-moulded discs of polypropylene and untreated and silane-treated talc-filled polypropylene composites,” *Polymer*, vol. 40, no. 19, pp. 5345–5353, 1999.

[37] J. Zhou and S. S. Sheiko, “Reversible shape-shifting in polymeric materials,” *Journal of Polymer Science Part B: Polymer Physics*, vol. 54, no. 14, pp. 1365–1380, 2016.

[38] V. Sessini, M. P. Arrieta, A. Fernández-Torres, and L. Peponi, “Humidity-activated shape memory effect on plasticized starch-based biomaterials,” *Carbohydrate Polymers*, vol. 179, pp. 93–99, 2018.

[39] A. M. Schmidt, “Electromagnetic activation of shape memory polymer networks containing magnetic nanoparticles,” *Macromolecular Rapid Communications*, vol. 27, no. 14, pp. 1168–1172, 2006.

[40] X. Li, L. Wang, Z. Zhang, D. Kong, X. Ao, and X. Xiao, “Electroactive high-temperature shape memory polymers with high recovery stress induced by ground carbon fibers,” *Macromolecular Chemistry and Physics*, vol. 220, no. 17, p. 1900164, 2019.

[41] E. Havens, E. A. Snyder, and T. H. Tong, “Light-activated shape memory polymers and associated applications,” in *Smart Structures and Materials 2005: Industrial and Commercial Applications of Smart Structures Technologies* (E. V. White, ed.), vol. 5762, pp. 48 – 55, International Society for Optics and Photonics, SPIE, 2005.

[42] J. Leng, X. Lan, Y. Liu, and S. Du, “Shape-memory polymers and their composites: Stimulus methods and applications,” *Progress in Materials Science*, vol. 56, no. 7, pp. 1077–1135, 2011.

[43] T. Chen, O. R. Bilal, K. Shea, and C. Daraio, “Harnessing bistability for directional propulsion of soft, untethered robots,” *Proceedings of the National Academy of Sciences*, vol. 115, no. 22, pp. 5698–5702, 2018.

[44] M. T. Tolley, S. M. Felton, S. Miyashita, L. Xu, B. Shin, M. Zhou, D. Rus, and R. J. Wood, “Self-folding shape memory laminates for automated fabrication,” pp. 4931–4936, 2013.

[45] A. Melocchi, M. Uboldi, N. Inverardi, F. Briatico-Vangosa, F. Baldi, S. Pandini, G. Scalet, F. Auricchio, M. Cerea, A. Foppoli, A. Maroni, L. Zema, and A. Gazzaniga, “Expandable drug delivery system for gastric retention based on shape

memory polymers: Development via 4d printing and extrusion," *International Journal of Pharmaceutics*, vol. 571, p. 118700, 2019.

[46] J. Shintake, V. Cacucciolo, D. Floreano, and H. Shea, "Soft robotic grippers," *Advanced Materials*, vol. 30, no. 29, p. 1707035, 2018.

[47] Y. Liu, H. Du, L. Liu, and J. Leng, "Shape memory polymers and their composites in aerospace applications: a review," *Smart Materials and Structures*, vol. 23, p. 023001, jan 2014.

[48] E. Boatti, G. Scalet, and F. Auricchio, "A three-dimensional finite-strain phenomenological model for shape-memory polymers: Formulation, numerical simulations, and comparison with experimental data," *International Journal of Plasticity*, vol. 83, pp. 153–177, 2016.

[49] M. Giuliano, *Differential Scanning Thermal Analysis of Shape-Memory Polymers, Polymer Blends and Composites*, pp. 153–166. 01 2020.

[50] W. Xu, S. Wu, G. P. Balamurugan, M. R. Thompson, F. A. Brandys, and K. E. Nielsen, "Evaluating shape memory behavior of polymer under deep-drawing conditions," *Polymer Testing*, vol. 62, pp. 295–301, 2017.

[51] E. M. Zirdehi, H. Dumlu, G. Eggeler, and F. Varnik, "On the size effect of additives in amorphous shape memory polymers," *Materials*, vol. 14, no. 2, 2021.

[52] T. Xie, "Recent advances in polymer shape memory," *Polymer*, vol. 52, no. 22, pp. 4985–5000, 2011.

[53] X. Guan, Y. Dong, H. Xia, J. Yao, and Q.-Q. Ni, "Mechanical and shape memory performance of shape memory polyurethane-based aligned nanofibers," *Polymer Testing*, vol. 91, p. 106778, 2020.

[54] H. Lu and W. M. Huang, "On the origin of the vogel–fulcher–tammann law in the thermo-responsive shape memory effect of amorphous polymers," *Smart Materials and Structures*, vol. 22, p. 105021, sep 2013.

[55] H. Tobushi, H. Hara, E. Yamada, and S. Hayashi, "Thermomechanical properties in a thin film of shape memory polymer of polyurethane series," *Smart Materials and Structures*, vol. 5, pp. 483–491, aug 1996.

[56] C. Liang, C. Rogers, and E. Malafeew, "Investigation of shape memory polymers and their hybrid composites," *Journal of Intelligent Material Systems and Structures*, vol. 8, no. 4, pp. 380–386, 1997.

[57] S. Thakur and J. Hu, "Polyurethane: a shape memory polymer (smp)," *Aspects of Polyurethanes; Yilmaz, F., Ed.; InTechOpen: London, UK*, pp. 53–71, 2017.

[58] K. B. Kyu, S. Y. Jo, C. S. Mo, and J. H. Mo, “Shape-memory behavior of segmented polyurethanes with an amorphous reversible phase: The effect of block length and content,” *Journal of Polymer Science Part B: Polymer Physics*, vol. 38, no. 20, pp. 2652–2657, 2000.

[59] J. J. Song, I. Srivastava, J. Kowalski, and H. E. Naguib, “Fabrication and characterization of a foamed polylactic acid (PLA)/ thermoplastic polyurethane (TPU) shape memory polymer (SMP) blend for biomedical and clinical applications,” in *Behavior and Mechanics of Multifunctional Materials and Composites 2014* (N. C. Goulbourne and H. E. Naguib, eds.), vol. 9058, pp. 86 – 98, International Society for Optics and Photonics, SPIE, 2014.

[60] H. Karbasi and H. Reiser, “Smart mold: Real-time in-cavity data acquisition,” in *First Annual Technical Showcase & Third Annual Workshop, Canada*, Citeseer, 2006.

[61] G. Gordon, D. O. Kazmer, X. Tang, Z. Fan, and R. X. Gao, “Quality control using a multivariate injection molding sensor,” *The International Journal of Advanced Manufacturing Technology*, vol. 78, no. 9-12, pp. 1381–1391, 2015.

[62] P. Zhao, J. Zhang, Z. Dong, J. Huang, H. Zhou, J. Fu, and L.-S. Turng, “Intelligent injection molding on sensing, optimization, and control,” *Advances in Polymer Technology*, vol. 2020, 2020.

[63] S. Montgomery and V. Gallo, “Achieve process transparency with inmold cavity sensors,” *Plast. Technol.*, 2012.

[64] “Iso 294-1:2017 plastics — injection moulding of test specimens of thermoplastic materials — part 1: General principles, and moulding of multipurpose and bar test specimens.,” 2017.

[65] “Iso 3167:2014 plastics — multipurpose test specimens.,” 2014.

[66] “Iso 75-1:2013 plastics — determination of temperature of deflection under load — part 1: General test method.,” 2013.

[67] “Iso 178:2019 plastics — determination of flexural properties.,” 2019.

[68] “Iso 179-1:2010 plastics — determination of charpy impact properties — part 1: Non-instrumented impact test.,” 2010.

[69] E. M. et al., “Design of an innovative system for wave generation in direct tension–compression split hopkinson bar,” *J. Dyn. Behav. Mater.*, 2015.

[70] C. Fernandes, A. J. Pontes, J. C. Viana, and A. Gaspar-Cunha, “Modeling and optimization of the injection-molding process: A review,” *Advances in Polymer Technology*, vol. 37, no. 2, pp. 429–449, 2018.

[71] X. Shi, X. Ni, Y. Wang, C. Wu, R. Li, and M. Gu, "Injection mold analysis based on moldex3d car dashboard back cover casting system," *IOP Conference Series: Earth and Environmental Science*, vol. 252, p. 022103, jul 2019.

[72] J.-M. Kim and M.-Y. Lyu, "An application of cae in the optimization of runner size in injection molding," *Transactions of Materials Processing*, vol. 15, no. 5, pp. 347–353, 2006.

[73] A. Kumar and R. Arya, "Optimizing cooling efficiency through conformal cooling using moldex3d cae simulation," 2021.

[74] C.-T. Lu, C.-H. Chen, and S.-C. Tseng, "Application of conformal cooling to reduce cooling time and warpage of a u-shaped plate," in *AIP Conference Proceedings*, vol. 2065, p. 030007, AIP Publishing LLC, 2019.

[75] P. H. Foss, H.-C. Tseng, J. Snawerdt, Y.-J. Chang, W.-H. Yang, and C.-H. Hsu, "Prediction of fiber orientation distribution in injection molded parts using moldex3d simulation," *Polymer composites*, vol. 35, no. 4, pp. 671–680, 2014.

[76] A. Islam, X. Li, and M. Wirska, "Injection moulding simulation and validation of thin wall components for precision applications," in *International Scientific-Technical Conference MANUFACTURING*, pp. 96–107, Springer, 2019.

[77] T.-C. Chen, C.-T. Huang, Y.-C. Chiu, W.-D. Wang, C.-L. Hsu, C.-Y. Lin, and L.-W. Kao, "Material saving and product quality improvement with the visualization of hot runner design in injection molding," *International Journal of Precision Engineering and Manufacturing*, vol. 14, no. 6, pp. 1109–1112, 2013.

[78] N. T. Tran and M. Gehde, "Creating material data for thermoset injection molding simulation process," *Polymer Testing*, vol. 73, pp. 284–292, 2019.

[79] E. Farotti, E. Mancini, T. Bellezze, and M. Sasso, "Investigation of the effects of mold temperature, test temperature and strain rate on mechanical behaviour of polypropylene," *Journal of Dynamic Behavior of Materials*, vol. 5, no. 3, pp. 344–360, 2019.

[80] Y.-C. Chen, C.-C. Hsu, and C.-H. Hsu, "Numerical simulation for predicting sink marks on injection molding and injection compression molding process," in *AIP Conference Proceedings*, vol. 2205, p. 020014, AIP Publishing LLC, 2020.

[81] P. Thakre, A. S. Chauhan, A. Satyanarayana, E. R. Kumar, and R. Pradyumna, "Estimation of shrinkage & distortion in waxinjection using moldex3d simulation," *Materials Today: Proceedings*, vol. 5, no. 9, pp. 19410–19417, 2018.

[82] T. Chu, W. Ranson, and M. A. Sutton, "Applications of digital-image-correlation techniques to experimental mechanics," *Experimental mechanics*, vol. 25, no. 3, pp. 232–244, 1985.

[83] D. S. Zhang, M. Luo, and D. D. Arola, “Displacement/strain measurements using an optical microscope and digital image correlation,” *Optical Engineering*, vol. 45, no. 3, p. 033605, 2006.

[84] “Astm d3418 - standard test method for transition temperatures of polymers by differential scanning calorimetry,”

[85] W. Wagermaier, K. Kratz, M. Heuchel, and A. Lendlein, “Characterization methods for shape-memory polymers,” *Shape-memory polymers*, pp. 97–145, 2009.

[86] D. Kong and X. Xiao, “High cycle-life shape memory polymer at high temperature,” *Scientific reports*, vol. 6, no. 1, pp. 1–10, 2016.

[87] H. Fisher, P. Woolard, C. Ross, R. Kunkel, B. N. Bohnstedt, Y. Liu, and C.-H. Lee, “Thermomechanical data of polyurethane shape memory polymer: Considering varying compositions,” *Data in brief*, vol. 32, p. 106294, 2020.

[88] J. Hu, W. Chen, P. Fan, J. Gao, G. Fang, Z. Cao, and F. Peng, “Epoxy shape memory polymer (smp): Material preparation, uniaxial tensile tests and dynamic mechanical analysis,” *Polymer Testing*, vol. 62, pp. 335–341, 2017.

[89] G. Li and W. Xu, “Thermomechanical behavior of thermoset shape memory polymer programmed by cold-compression: Testing and constitutive modeling,” *Journal of the Mechanics and Physics of Solids*, vol. 59, no. 6, pp. 1231–1250, 2011.

[90] C. Liu, H. Qin, and P. T. Mather, “Review of progress in shape-memory polymers,” *J. Mater. Chem.*, vol. 17, pp. 1543–1558, 2007.

[91] M. Amber, T. Gyaneshwar, and B. Jeffery, “Strain rate and temperature-dependent tensile properties of an epoxy-based, thermosetting, shape memory polymer (veriflex-e),” *Mechanics of Time-Dependent Materials*, vol. 16, pp. 205–221, 05 2011.

[92] H. Tobushi, R. Matsui, K. Takeda, and S. Hayashi, “Mechanical testing of shape-memory polymers for biomedical applications,” in *Shape Memory Polymers for Biomedical Applications* (L. Yahia, ed.), Woodhead Publishing Series in Biomaterials, pp. 65–75, Woodhead Publishing, 2015.

[93] H. Tobushi, K. Okumura, M. Endo, and S. Hayashi, “Thermomechanical properties of polyurethane-shape memory polymer foam,” *Journal of intelligent material systems and structures*, vol. 12, no. 4, pp. 283–287, 2001.

[94] D. M. Feldkamp and I. A. Rousseau, “Effect of the deformation temperature on the shape-memory behavior of epoxy networks,” *Macromolecular Materials and Engineering*, vol. 295, no. 8, pp. 726–734, 2010.

[95] D. Ratna and J. Karger-Kocsis, “Recent advances in shape memory polymers and composites: a review,” *Journal of Materials Science*, vol. 43, no. 1, pp. 254–269, 2008.

[96] B. Atli, F. Gandhi, and G. Karst, “Thermomechanical characterization of shape memory polymers,” *Journal of Intelligent Material Systems and Structures*, vol. 20, no. 1, pp. 87–95, 2009.

[97] B. Yang, W. Huang, C. Li, and L. Li, “Effects of moisture on the thermomechanical properties of a polyurethane shape memory polymer,” *Polymer*, vol. 47, no. 4, pp. 1348–1356, 2006.

[98] F. Castro, K. K. Westbrook, J. Hermiller, D. U. Ahn, Y. Ding, and H. J. Qi, “Time and temperature dependent recovery of epoxy-based shape memory polymers,” *Journal of engineering materials and technology*, vol. 133, no. 2, 2011.

[99] A. Lendlein and S. Kelch, “Shape-memory polymers,” *Angewandte Chemie International Edition*, vol. 41, no. 12, pp. 2034–2057, 2002.

[100] C. Schmidt, K. Neuking, and G. Eggeler, “Functional fatigue of shape memory polymers,” *Advanced Engineering Materials*, vol. 10, no. 10, pp. 922–927, 2008.

[101] A. J. McClung, G. P. Tandon, and J. W. Baur, “Deformation rate-, hold time-, and cycle-dependent shape-memory performance of veriflex-e resin,” *Mechanics of Time-Dependent Materials*, vol. 17, no. 1, pp. 39–52, 2013.

[102] C. Liang, C. A. Rogers, and E. Malafeew, “Investigation of shape memory polymers and their hybrid composites,” *Journal of Intelligent Material Systems and Structures*, vol. 8, no. 4, pp. 380–386, 1997.

[103] Y. Lu, J. Fulcher, G. Tandon, D. Foster, and J. Baur, “Microscale thermomechanical characterization of environmentally conditioned shape memory polymers,” *Polymer Testing*, vol. 30, no. 5, pp. 563–570, 2011.

[104] P. Flory, *Principles of Polymer Chemistry.* Baker lectures 1948, Cornell University Press, 1953.

[105] M. Behl, M. Y. Razzaq, and A. Lendlein, “Multifunctional shape-memory polymers,” *Advanced Materials*, vol. 22, no. 31, pp. 3388–3410, 2010.

[106] G. Li and A. Wang, “Cold, warm, and hot programming of shape memory polymers,” *Journal of Polymer Science Part B: Polymer Physics*, vol. 54, no. 14, pp. 1319–1339, 2016.

[107] C. Poilâne, P. Delobelle, C. Lexcellent, S. Hayashi, and H. Tobushi, “Analysis of the mechanical behavior of shape memory polymer membranes by nanoindentation, bulging and point membrane deflection tests,” *Thin Solid Films*, vol. 379, no. 1-2, pp. 156–165, 2000.

[108] M. Sasso and D. Amodio, “Development of a biaxial stretching machine for rubbers by optical methods,” in *Society for Experimental Mechanics Annual Conference, St. Louis, MO, June*, pp. 4–7, 2006.

[109] U. D. Çakmak, I. Kallaí, and Z. Major, “Temperature dependent bulge test for elastomers,” *Mechanics Research Communications*, vol. 60, pp. 27–32, 2014.

[110] A. Kalkman, A. Verbruggen, and G. Janssen, “High-temperature bulge-test setup for mechanical testing of free-standing thin films,” *Review of scientific instruments*, vol. 74, no. 3, pp. 1383–1385, 2003.

[111] M. Rossi, L. Cortese, K. Genovese, A. Lattanzi, F. Nalli, and F. Pierron, “Evaluation of volume deformation from surface dic measurement,” *Experimental Mechanics*, vol. 58, no. 7, pp. 1181–1194, 2018.

[112] C. Popa, R. Fleischhauer, K. Schneider, and M. Kaliske, “Formulation and implementation of a constitutive model for semicrystalline polymers,” *International Journal of Plasticity*, vol. 61, pp. 128–156, 2014.

[113] J. Hu, Y. Zhu, H. Huang, and J. Lu, “Recent advances in shape–memory polymers: Structure, mechanism, functionality, modeling and applications,” *Progress in Polymer Science*, vol. 37, no. 12, pp. 1720–1763, 2012.

[114] T. D. Nguyen, H. J. Qi, F. Castro, and K. N. Long, “A thermoviscoelastic model for amorphous shape memory polymers: incorporating structural and stress relaxation,” *Journal of the Mechanics and Physics of Solids*, vol. 56, no. 9, pp. 2792–2814, 2008.

[115] B. Zhou, X. Lan, Y. Liu, and J. Leng, “Modeling thermo-mechanical behaviors of reinforced shape memory polymer under cyclic loads,” in *Second International Conference on Smart Materials and Nanotechnology in Engineering*, vol. 7493, p. 749336, International Society for Optics and Photonics, 2009.

[116] H. Lu and W. M. Huang, “On the origin of the vogel–fulcher–tammann law in the thermo-responsive shape memory effect of amorphous polymers,” vol. 22, p. 105021, sep 2013.

[117] J. Diani, Y. Liu, and K. Gall, “Finite strain 3d thermoviscoelastic constitutive model for shape memory polymers,” *Polymer Engineering & Science*, vol. 46, no. 4, pp. 486–492, 2006.

[118] M. Baghani, R. Naghdabadi, J. Arghavani, and S. Sohrabpour, “A thermodynamically-consistent 3d constitutive model for shape memory polymers,” *International Journal of Plasticity*, vol. 35, pp. 13–30, 2012.

[119] Y. Liu, K. Gall, M. L. Dunn, A. R. Greenberg, and J. Diani, “Thermomechanics of shape memory polymers: Uniaxial experiments and constitutive modeling,” *International Journal of Plasticity*, vol. 22, no. 2, pp. 279–313, 2006.

[120] Y.-C. Chen and D. C. Lagoudas, "A constitutive theory for shape memory polymers. part i: Large deformations," *Journal of the Mechanics and Physics of Solids*, vol. 56, no. 5, pp. 1752–1765, 2008.

[121] J. H. Kim, T. J. Kang, and W.-R. Yu, "Thermo-mechanical constitutive modeling of shape memory polyurethanes using a phenomenological approach," *International Journal of Plasticity*, vol. 26, no. 2, pp. 204–218, 2010.

Publications

The research activity during the three years of doctorate brought the following publications:

International Journals

- M. Utzeri, E. Farotti, M. Coccia, E. Mancini, M. Sasso "High strain rate compression behaviour of 3D printed Carbon-PA". In: *Journal of Materials Research* 36, 2083–2093 (2021). https://doi.org/10.1557/s43578-021-00248-9
- M. Coccia, E. Farotti, G. Chiappini, T. Bellezze, M. Sasso "Effects of temperature, strain and strain rate onshape memory thermoplastic polyurethane processed by injection molding" (under review)

International Conference Proceedings

- M. Coccia, A. Lattanzi, G. Chiappini, M. Sasso, M. Rossi "Analysis of the thermomechanical behaviour of SMP in equi-biaxial condition by means of hydraulic bulge test". In: *Proceedings of the SEM Annual Conference 2021*
- M. Coccia, E. Farotti, A. Lattanzi "Simulation of the thermomechanical SMP in equi-biaxial condition by HBT". In: *Proceedings of the AIAS Annual Conference 2021*
- G. Chiappini, M. Coccia, M. Rossi, F. Marchione, P. Munafò, C. Scoccia, C. Luca "Assessment of the deformation behavior of a tensegrity floor through photogrammetry". In: *Proceedings of the AIAS Annual Conference 2021*

National Conference Proceedings

- M. Utzeri, E. Farotti, M. Coccia "Identificazione di un modello di materiale equivalente per strutture cellulari gyroid realizzate mediante manifattura additiva" In: *Atti del 50 ° Convegno Nazionale AIAS 2021*